Depth-sensitive Raman spectroscopy of layered turbid media

By
Khan Mohammad Khan

PHYS03201304003

Raja Ramanna Centre for Advanced Technology, Indore

A thesis submitted to the

Board of Studies in Physical Sciences

In partial fulfillment of requirements

for the Degree of

DOCTOR OF PHILOSOPHY

of

HOMI BHABHA NATIONAL INSTITUTE

August, 2018

Homi Bhabha National Institute
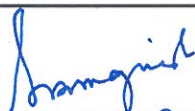
Recommendations of the Viva Voce Committee

As members of the Viva Voce Committee, we certify that we have read the dissertation prepared by Khan Mohammad Khan entitled "Depth-sensitive Raman spectroscopy of layered turbid media" and recommend that it may be accepted as fulfilling the thesis requirement for the award of Degree of Doctor of Philosophy.

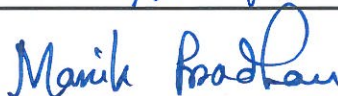Chairperson – Prof. K. S. Bindra   Date: 20-9-2019.

Guide / Convener – Prof. S. K. Majumder   Date: 20/9/19

Examiner- Prof. Manik Pradhan   Date: 20-9-2019

Member 1- Prof. S. R. Mishra   Date: 20-9-2019

Member 2- Prof. A. Moorti   Date: 20/9/2019.

Member 3- Prof. P. K. Mukhopadhyay   Date: 20/9/19

Member 4- Prof. C. Mukherjee   Date: 20/9/19

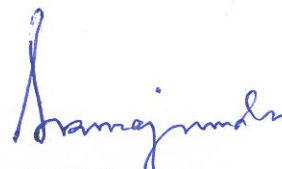External Member - Prof. K. Divakar Rao   Date: 20/9/19

Final approval and acceptance of this thesis is contingent upon the candidate's submission of the final copies of the thesis to HBNI.

    I hereby certify that I have read this thesis prepared under my direction and recommend that it may be accepted as fulfilling the thesis requirement.

Date: 27/9/2019

Place: Indore

S. K. Majumder

STATEMENT BY AUTHOR

This dissertation has been submitted in partial fulfillment of requirements for an advanced degree at Homi Bhabha National Institute (HBNI) and is deposited in the Library to be made available to borrowers under rules of the HBNI.

Brief quotations from this dissertation are allowable without special permission, provided that accurate acknowledgement of source is made. Requests for permission for extended quotation from or reproduction of this manuscript in whole or in part may be granted by the Competent Authority of HBNI when in his or her judgment the proposed use of the material is in the interests of scholarship. In all other instances, however, permission must be obtained from the author.

Khan Mohammad Khan

DECLARATION

I, hereby declare that the investigation presented in the thesis has been carried out by me. The work is original and has not been submitted earlier as a whole or in part for a degree / diploma at this or any other Institution / University.

Khan Mohammad Khan

List of Publications arising from the thesis

Journal

1. "Cone-shell Raman spectroscopy (CSRS) for depth-sensitive measurements in layered tissue", K. M. Khan, S. K. Majumder and P. K. Gupta, *Journal of Biophotonics*, **2015**, *8(11-12)*, 889-896.
2. "Inverse SORS for detecting a low Raman-active turbid sample placed inside a highly Raman-active diffusely scattering matrix – A feasibility study", K. M. Khan, S. B. Dutta, H. Krishna and S. K. Majumder, *Journal of Biophotonics*, **2016**, 9(9), 879-887.
3. "Off-confocal Raman spectroscopy (OCRS) for subsurface measurements in layered turbid samples", K. M. Khan, N. Ghosh and S. K. Majumder, *Journal of Optics*, **2016**, 18(9), 095301.
4. "Depth-sensitive Raman spectroscopy of intact formalin-fixed and paraffin-embedded tissue blocks for objective diagnosis of cancer - An exploratory study", K. M. Khan, H. Krishna, C. V. Kulkarni and S. K. Majumder, *Journal of Analytical Oncology*, **2016**, 5(4), 153-163.
5. "Inverse spatially-offset Raman spectroscopy using optical fibers – An axicon lens-free approach", K. M. Khan, S. B. Dutta, N. Kumar, A. Dalal, A. Srivastava, H. Krishna and S. K. Majumder, *Journal of Biophotonics*, **2019**, *e201900140*.

Manuscripts to be submitted:

1. "Reverse confocal polarized Raman spectroscopy (RCPRS) for layered tissue analysis", K. M. Khan, A. Srivastava, S. B. Dutta, N. Kumar and S. K. Majumder, To be submitted
2. "Depth-sensitive Raman spectroscopy of layered turbid samples", K. M. Khan and S. K. Majumder, To be submitted

Conferences

1. K. M. Khan, S. B. Dutta, S. K. Majumder and P. K. Gupta, Spatially-offset Raman spectroscopy (SORS) of paraffin-embedded tissue blocks, Proceedings of DAE-BRNS National Laser Symposium (NLS-23), p. 194, held at Sri Venkateswara University, Tirupati, Dec. 3-6, 2014.
2. S. K. Majumder and K. M. Khan, Photonics for depth-sectioning of layered biological tissue, Proceedings of DAE-BRNS 3rd National Workshop on Materials Chemistry (Optical Materials) NWMC-2015 (OPT-MAT), p. 16-22, held at BARC, Mumbai, Nov. 20-21, 2015.

3. A. Srivastava, N. Kumar, K. M. Khan, S. B. Dutta and S. K. Majumder, Polarized micrometer scale spatially-offset Raman spectroscopy (μ-SORS) for layered biological media, Proceedings of DAE-BRNS National Laser Symposium (NLS-26), p. 134, held at BARC, Mumbai, Dec. 20-23, 2017.
4. A. Srivastava, K. M. Khan, S. B. Dutta, A. Dalal, N. Kumar and S. K. Majumder, Reverse confocal Raman spectroscopy (RCRS) for analysis of layered biological tissue, Proceedings of DAE-BRNS National Laser Symposium (NLS-27), p. 140, held at RRCAT, Indore, Dec. 3-6, 2018.

Khan Mohammad Khan

I dedicate this work to my parents, my wife and beloved Alisha & Tanweer

ACKNOWLEDGEMENTS

CONTENTS

SUMMARY

In recent years, Raman spectroscopy has been suggested and validated as a potential tool for non-invasive and near real-time diagnosis of various tissue abnormalities. Despite its usefulness in certain situations, a major shortcoming of its conventional experimental configuration is that the measured Raman signal at a given point on the surface of an interrogated tissue is volume-integrated (over the sub-surface depths) and therefore, it does not contain the desired information of the sub-surface tissue layers having different Raman characteristics. Obtaining depth-wise Raman signal is important because it may allow a more detailed analysis of the biochemical (and morphological) state of a given tissue thereby leading to an improved feedback on tissue state.

There are two primary objectives of the present thesis. The first is to investigate the applicability of existing depth-sensitive Raman spectroscopic techniques for applications involving turbid media such as biological tissues and evaluate their relative performances in probing sub-surface depths within the media. In order to achieve this objective, two independent studies have been carried out. While in the first study applicability of a CRS based technique was assessed for obtaining diagnostic feedback about a tissue under interrogation by measuring confocal Raman spectra from intact FFPE tissue blocks without preparing any micro-thin tissue sections or any other processing, in the second study the applicability of inverse SORS was investigated in identifying the presence of a very low Raman-active turbid sample placed inside a highly Raman-active diffusely scattering matrix.

The second objective includes development of new depth-sensitive Raman spectroscopic techniques and evaluation of their capabilities in overcoming major limitations of the existing techniques with a view to translating them into field-deployable instruments.

The work towards achieving this objective resulted in the development of four novel approaches of depth-sensitive Raman measurements from tissues listed below.

1. RCPRS: In this approach, the depth-sensitive Raman measurements were performed by moving the focal plane of the illumination beam away from the tissue surface unlike in CRS where it was moved across the different depths of the target tissue. The approach was shown to overcome the drawback of lens-sample contact faced in a CRS setup and found to probe comparatively larger sub-surface depths.

2. OCRS: It uses the experimental configuration of a confocal Raman, but employs off-confocal Raman detection for sub-surface interrogation of layered tissues. The two important advantages of this approach are that it does not require any adjustment in the sample arm of the system and the illumination light remains fixed on the sample surface and thereby providing the effective illumination.

3. CSRS: It employs the configuration of cone-shell Raman excitation and cone detection. Using this approach, Raman signal from a depth of up to few mm (~2.5 mm) beneath the surface could be measured.

4. An axicon lens free approach for implementing an inverse SORS: This approach not only probes higher depths as compared to CSRS but also has the ability of developing a compact and pencil-sized SORS probe, an urgent and current need in routine clinical pathology setting.

LIST OF FIGURES

deviation.

mirror, OL-objective lens, NF-notch filter and CL-convex lens.

position. The error bars represent ±1 standard deviation. (b) The ratio of the intensities of the Raman bands corresponding to 950 cm^{-1} and 1450 cm^{-1} as a function of the confocal-offsets investigated in steps of 100 µm. Error bars represent ±1 standard deviation. (c) Raman spectra of the surface muscle layer retrieved through scale subtraction using off-confocal spectrum with positive (upper row) and that with negative confocal offset (bottom row) along-with the reference Raman spectrum of the native muscle tissue (middle row). (d) Raman spectrum of sub-surface bone retrieved through scale subtraction using off-confocal spectrum with positive confocal offset (upper row) and that with negative confocal offset (bottom row) along-with the reference Raman spectrum of native bone (middle row).

abbreviations and their corresponding expanded forms are as follows: DL-Diode laser, LCF-Laser clean-up filter, OL-Objective lens, AX-Axicon lens, DF-Dichroic filter, ADL-Achromat doublet lens, NF-Notch filter, FCL-Fiber collimating lens.

spectra corresponding to three different lateral positions separated by ~1 mm from each other. The integration time for each of these measurements was 10 s. (b) Reference Raman spectra of muscle (upper panel) and bone (lower panel). Both the spectra are peak normalized. (c) The ratio of the intensities of the Raman bands corresponding to 955 cm^{-1} and 1447 cm^{-1} (I_{955}/I_{1447}) at different axial distances of the chicken tibia. Error bars represent ±1 standard deviation corresponding to three different spectra. (d) Raman spectra of muscle (a1) and bone (b1) retrieved through the scale subtraction technique.

PST block corresponding to 2.0 mm thick tissue.

were the maximum. The integration time used for each of these measurements was 20 s.

LIST OF TABLES

CHAPTER 1

Depth-sensitive Raman spectroscopy of layered

turbid samples

1.1 Introduction

Raman spectroscopy has drawn considerable attention in recent years as a promising new tool

for disease diagnosis [1-8]. Its major attraction comes from its ability to discern biochemical

make up of a tissue in a minimally invasive or non-invasive manner [1, 5-7, 9-10]. It probes

the vibrational energy levels of a molecule and the specific peaks in the Raman spectrum

correspond to particular chemical bonds or bond groups of the various bio-molecules

constituting the tissue [2-3]. As tissue transforms from normal to diseased, its overall

biochemical make up changes, and these changes are manifested in the measured Raman

spectra [3, 6, 9-10]. Typically, for recording a Raman spectrum, the target tissue is

illuminated by a laser of appropriate wavelength and the Raman signal back-scattered from it,

is detected using a Raman spectrometer [2-3, 6, 11-13]. Though this kind of conventional

measurement has been shown to be useful in certain situations, its major shortcoming is that

it obtains information only from the surface of a tissue. However, the majority of biological

tissues are known to have sub-surface layers, with different layers having different

biochemical and morphological make-up. Further, the morphological and biochemical

changes, that these sub-surface layers undergo as tissue transforms from normal to diseased,

are also believed to be quite different from that of the surface [14-16]. Consequently, the

resulting changes in the optical properties that get manifested in the Raman signatures of the

surface and the sub-surface tissue layers are not expected to be the same. Since in the conventional approach, the measured Raman signal at a given point on the surface of an interrogated tissue is volume integrated (over the sub-surface depths), it does not contain the desired information of the sub-surface tissue layers having different Raman characteristics. Obtaining depth-wise Raman signal is crucial because it may allow a more detailed analysis of the biochemical state of a given tissue thereby leading to an improved feedback on tissue state. Therefore, recently, there is a significant surge of interest in excogitating ways for depth-sensitive measurements of the Raman signatures originating from different layers of a biological tissue [17-22].

1.2 Background

The knowledge of light propagation in a biological tissue is an important prerequisite not only for understanding the principles underlying various depth-sensitive Raman spectroscopic techniques, but also in selecting the one that is most appropriate for a given tissue-application.
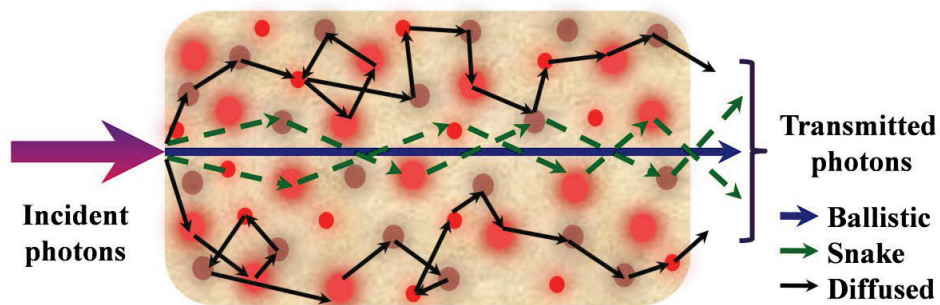
Figure 1.1: *Light propagation in a tissue like turbid medium*

A typical scheme of light propagation in a turbid medium, like biological tissue, is shown in Figure 1.1. Based on the trajectories followed by incident photons, the photons can

be grouped into three categories: ballistic, snake and diffused [23-24]. The ballistic photons are not influenced by the scattering centres of the medium and maintain their identity and directionality while leaving the medium. The snake photons are the ones which are scattered from few scattering centres (~1-5) and partially retain their directionality. However, the diffused photons are the ones which undergo multiple scattering (with number of scattering events >10) and completely lose their identity as well as the directionality while leaving the medium. On a time-scale, ballistic photons come out (of the tissue) first, snake the second, and, lastly, the diffused.

With the use of one or the other category of Raman photons available for detection, a variety of techniques of varying rigor [13, 19-22, 25-28] have been proposed for disentangling the Raman signals generated in the different tissue layers. Of these, the techniques based on confocal and spatially-offset Raman detection are the ones which have been widely researched for biomedical applications because of their suitability for use in biological samples [19-22]. While the former seeks to measure the un-scattered or the ballistic Raman photons in the vicinity of illumination, the later measures the diffused Raman photons generated (out of multiple scattering) away from the point of illumination. This fundamental difference in their underlying principles leads to two different limits of depth that these techniques are capable of probing. For example, while confocal detection is suitable only for depths ranging from several tens to a few hundreds of micrometers (i.e. shallow depths), the spatially-offset Raman detection allows probing the depths up to several mm (i.e. deeper layers). However, the signal-to-noise ratio (SNR) of the measured Raman signal gets quickly downgraded while probing such larger depths.

In confocal detection, the point of illumination (i.e. the focus of the incident light) on the (layered) sample is imaged onto the detector, through a pinhole placed in front of the detector [25-26, 29-30]. The underlying principle of such detection can be understood from

the figure shown in Figure 1.2. A laser beam is focused tightly on a plane, *F1*, at a point, *a*, by using a microscope objective lens (L1) of high numerical aperture (NA). This point is imaged (path shown in red colour) at point, *a'*, on plane, *P1*, through another objective lens, L2. In other words, the Raman signal originating from the point, *a*, will be available for the detection at the point, *a'*. Since a focused Gaussian beam has certain axial spread (or Rayleigh range) over which the intensity reduces to half of its maximum intensity, Raman signal can also originate from another point, *b*, lying on plane, *F2*. On tracing the ray diagram for this point (shown in violet colour), we can observe that this Raman signal will efficiently be detected at point, *b'* lying on plane, *P2*. If a pinhole of appropriate size ($\geq$ size of image point, *a'*, on plane, *P1* and < size of image point, *b'* on plane, *P1*) is placed on the plane, *P1* with its centre being at *a'*, a significant fraction of the Raman signal originated from the point, *b* can be rejected i.e. the Raman signal corresponding to the focal point of the incident light, is only collected by the detector.
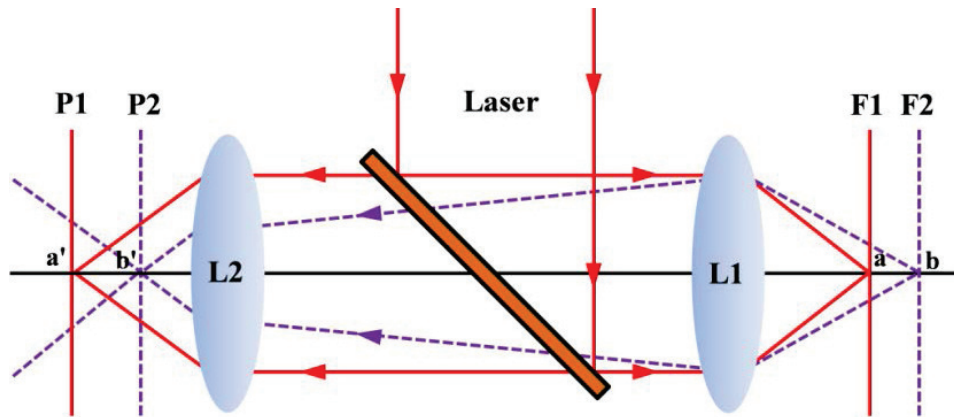
Figure 1.2: *Schematic showing the principle of confocal detection*

For depth-sensitive measurements, the pinhole is kept fixed in its original plane and the incident laser light is focused on different sample-planes (e.g. *F1*, *F2* etc.) of the target tissue by varying the separation between the lens, L1 and the tissue surface. For each sample-plane, the Raman signals generated from the out-of-focus planes are rejected by the pinhole.

The degree of rejection, which decides the depth resolution, is primarily determined by NA of the lens, L1, and the size of the pinhole used. In practice, the NA is kept as high as possible to create a focal point of least diameter. Further, a pinhole of smaller size efficiently rejects the signals corresponding to out-of-focus planes. However, it sharply decreases the SNR of the measured Raman signal and therefore, in practice, there is a trade-off between the size of the pinhole and SNR.

In the spatially-offset detection technique, also called source-detector separation (SDS), Raman spectra are collected from those points (lying on the surface of the tissue) which are spatially away from the point of illumination [17, 21-22]. A schematic to understand the SDS principle is shown in Figure 1.3. The schematic is a re-sketched form of the Figure 1.1, with the assumption that all the Raman scattered photons leave the sample from its surface only. This assumption holds good for a semi-infinite turbid medium.
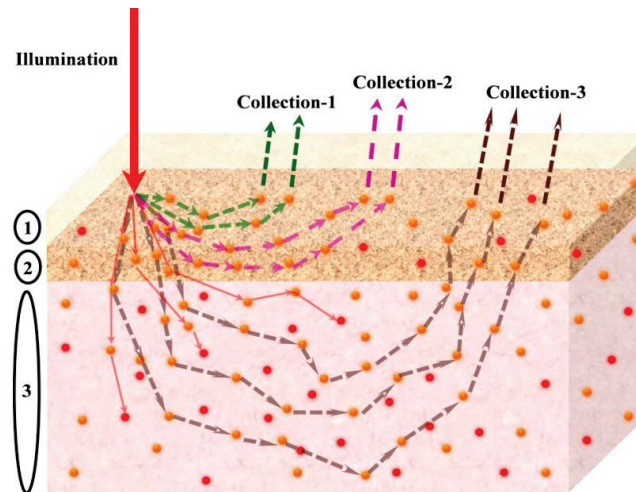
Figure 1.3: *Schematic showing the SDS principle*

In such case, deeper born Raman photons traverse larger distances and on their way they diffuse sideways to a greater extent than the Raman photons originating from shallower layers [17, 21-22]. This particular point is depicted in the figure by showing trajectories of the photons corresponding to three different collections. Among the three collections, the

Raman signal measured by 'collection-3' will predominately contain the Raman photons originated in the 3rd layer of the sample. It is therefore the set of Raman spectra obtained at varying spatial separation from the point of illumination contains different relative contributions of Raman signal from layers located at different depths within the sample. This has been shown using an experiment carried out with spatially-offset Raman spectroscopy (SORS) [17], one of the techniques based on the SDS principle.

In practice, the spatially-offset Raman detection is generally implemented with fiber-optic probes by arranging multiple fibers with a pre-fixed spatial separation between the fibers either in a linear array with the illumination fiber at either of the ends, or in concentric circular arrays with the central fiber providing illumination. The circular configuration (see Figure 1.4a) is usually preferred over the linear configuration because of its ability of providing increased signal strength or improved SNR. However, a major limitation of such configuration is that it monitors the Raman signal from sub-surface depths in a discrete manner. This difficulty can be overcome by using an inverse SORS scheme [31] which provides the same set of information as the SORS gives, but with interchanged positions of the illumination and collection points through the use of illumination rings of varying radii and collection of Raman signal from the centre of these rings (see Figure 1.4b).
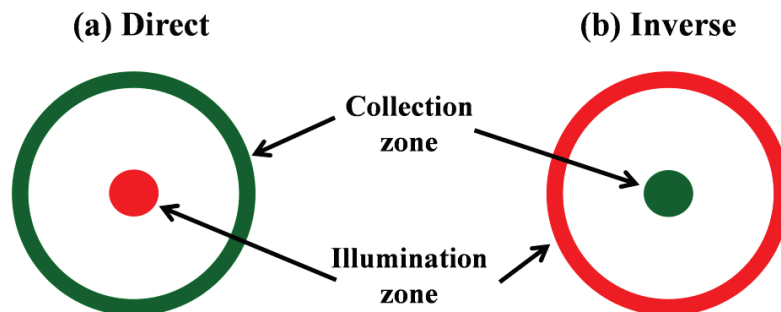
Figure 1.4: *Two basic schemes of spatially-offset detection (a) direct and (b) inverse*

In the inverse scheme, the probing depths can be varied in a continuous manner by simply varying the radii of the illumination rings formed using an axicon lens. The other

important advantage of this scheme is that the SNR is found to be fairly good even at larger offsets (i.e. larger depths) and with a reasonable integration time (1-5 s). This is possible because of the ring illumination which leads to a much larger number of Raman photons that can diffuse through before being detected as compared to the point-illumination where the corresponding number of photons is expected to be much less. Further, availability of a wider illumination zone on the sample surface allows for interrogation of samples at a lower power density thereby reducing any adverse effects due to sample heating [21-22, 31]. This is particularly beneficial when probing biological tissues *in-vivo* where safe illumination intensity levels are required to be adhered to.

1.3 Status report on depth-sensitive Raman spectroscopy for biomedical applications

Over the years, there has been a concerted effort in using depth-sensitive Raman spectroscopy for a variety of biomedical applications. A brief overview of some of the representative studies is presented in the following to indicate the present state-of-the-art of depth-sensitive Raman spectroscopy for tissue analysis.

In confocal Raman technique of depth-sensitive detection, depth resolution is the most important parameter for showing its usefulness in optically separating various sub-surface layers of a given tissue [30]. This parameter is primarily determined by NA of the focusing lens and the pinhole used for rejecting out-of-focus photons. Neil J. Everall at Wilton Research Centre, UK elaborated this parameter in detail and explained its actual interpretation [25-26, 32]. He suggested that for obtaining a resolution near its theoretically estimated value the objective lens should be overfilled and free from spherical aberration. In order to overcome the spherical aberration, use of an oil-immersion objective lens was

recommended [25-26]. However, in some cases, the oil used as an index-matching fluid caused swelling or dissolution by interacting with the sample [25]. Tomba *et al.* [33] overcame this issue by introducing a thin polymer film as a barrier between the oil and the sample. Further, it was also suggested that one must carefully specify the working conditions under which the resolution was calculated. Neil J. Everall explained it by saying that the working resolution was highly sample dependent and therefore, could not be really considered as a unique characteristic of a given instrument [25-26]. For example, for a thin substrate, the contribution from out-of-focus regions will be minimum leading to a good resolution even though a low NA metallurgical objective lens is used. In case of a sufficiently thick substrate, a large number of out-of-focus photons cause a decreased resolution. According to Tabaksblat *et al.* [29], the percentage of out-of-focus photons can be >50%.

Although confocal Raman detection was used in various areas, we limit our discussion only to some of the representative studies performed for biomedical applications. Puppels *et al.* [34] were the first who studied single living cells and chromosomes with a confocal Raman instrument. They also employed their instrument for measuring Raman spectra of nuclei and cytoplasmic regions of single living human granulocytes [35]. Caspers *et al.* [36] obtained depth resolved information about the molecular composition of human skin by measuring *in-vivo* confocal Raman spectra. Later, they showed that the same technique could be used in determining water concentration in stratum corneum as a function of distance to the skin surface [37]. In recent years, the confocal detection has also been used for diagnosing human tissues *in-vivo*. For example, Choi *et al.* [38] applied the technique in ten patients having one of the most common skin cancers i.e. basal cell carcinoma (BCC), and stated that the differences between normal and BCC tissues were found mainly in the Raman bands corresponding to amide-I. Chad A. Lieber and his co-workers at Vanderbilt University, Tennessee investigated the potential use of confocal Raman in differentiating

normal and malignant skin lesions obtained from 39 patients [39-40]. Raman spectra were measured from a depth of ~100 μm, at 20 μm intervals. The discrimination analysis between different tissue pathological states resulted in a sensitivity and specificity of 100%. The potential of confocal Raman detection as an alternate of histopathological examination was also explored. In histopathology, high-resolution images (obtained by a white light microscope) of cellular and sub-cellular structures of properly pre-processed and appropriately stained specimens of thin tissue sections obtained by microtomy from formalin-fixed and paraffin-embedded (FFPE) tissue blocks are analyzed [41-42]. In such analyses, the diagnosis depends on the expert interpretation that suffers from both human as well as sampling errors [7]. This is particularly a concern in the context of the tumors that are atypical or lack morphological features useful for differential diagnosis. In order to overcome such difficulties, the confocal Raman detection was used for cancer diagnosis using FFPE tissue sections of various organs like cervix [43-45], ovary [46], skin [47] etc. Confocal Raman spectroscopy was also integrated with confocal microscopy for obtaining molecular composition with high spatial resolution and optical sections without physically dissecting the tissue [48]. Such integrated systems provide both biochemical and morphological information of a given tissue state and therefore improves the diagnostic feedback. We at RRCAT, Indore also developed two such integrated systems. In these systems we combined optical coherence tomography (OCT) with confocal Raman [20], and confocal fluorescence spectroscopy [49] for characterizing layered tissues; morphologically as well as biochemically. Recently, the confocal Raman technique has also been used in the detection of nasopharyngeal cancer [50].

Despite the fact that the confocal Raman detection was used by various laboratories for non-invasive diagnosis or characterization of biological tissues of various pathologies, the number of reports available on the development of a clinically acceptable confocal Raman

system is only a few. Chad A. Lieber at Vanderbilt University, Tennessee was the first who developed a handheld Raman probe cum spectrometer for clinical dermatologic applications [51]. A microscope objective lens of NA = 0.35 with the feature of automatic positioning (resolution = <0.1 μm) was used for focusing the light onto skin surface. Such translation allowed the control of focal depth within the sample and thus enabled depth-sensitive measurements. In a recent publication, Agenant *et al.* [52] reported development of a clinical superficial Raman probe based on the confocal detection with a phantom model.

In contrast to the confocal detection, depth resolution is not a crucial parameter for the techniques based on the SDS principle and therefore, the performances of such techniques are not judged by their resolutions. However, maximum probing depth, ease of obtaining the SDS effect, SNR of the measured Raman signals etc. are some of the important factors which are carefully considered during the development of a depth-sensitive Raman technique developed based on the SDS principle. In Raman spectroscopy, first depth-sensitive Raman configuration based on the SDS principle was demonstrated by Pavel Matousek and named SORS [17]. In recent years, several sister variants of SORS such as inverse SORS [31], defocused SORS [53] etc. have been proposed. While basic scheme of the inverse SORS has been discussed in Figure 1.4, in defocused SORS the focal point of the illuminating laser beam is kept inside the target sample. However, such defocused arrangement could not show its potential in biological applications due to its inability of acquiring Raman signatures from the samples of low Raman cross-sections like biological tissue. Recently, efforts were also made for obtaining the SORS effect with offsets of few tens of micrometers unlike the conventional millimetre scaled offsets [54-55]. Such variant, known as μ-SORS, has drawn considerable attention for non-destructive analysis of comparatively thinner (few tens of micrometers) sub-surface layers in a highly turbid medium. In this variant, both the illumination and collection zones on the sample surface are defocused by moving either the

sample away from the microscope objective lens or the lens away from the sample [55]. Most recently, a latest version of it with complete separation between the illumination and collection zones on the sample surface (named full μ-SORS) has also appeared in the literature [56]. Using Monte Carlo (MC) simulations, a theoretical comparison between the two newer variants of SORS based on the consideration of various parameters like depth selectivity, relative enhancement of sub-layer Raman signal etc. was made and it was found that full μ-SORS outperforms the other [56].

Although the concept of SORS was discovered much later than the confocal Raman, it has been finding its applications faster than the confocal Raman. The two main biomedical applications of the SORS include, non-invasive probing of bones through overlaying soft tissue [19, 57-58] and the detection of tumors beneath the normal human breast tissues [59-60]. Matthew V. Schulmerich and his co-workers at University of Michigan, USA acquired the first transcutaneous Raman spectra of bones [57]. They successfully measured the Raman spectra of chicken tibia through a overlaying soft tissue (thickness = 4 mm) and estimated ratio of the intensities of Raman bands of phosphate (~958 cm^{-1}) and carbonate (~1070 cm^{-1}) with a good accuracy. The calculation of the ratio is particularly important as the ratio may be altered in osteoporosis, a terrible disease of bone fracturing [61]. In an independent study, Matousek *et al.* [19] demonstrated the feasibility of measuring SORS spectra of human bone *in-vivo* with a laser power of 2 mW, much below the threshold for the safe illumination of skin. Recently, a more detailed analytical study in 32 anesthetized mice has also been performed [58]. Non-invasive diagnosis of breast cancer is another important application area of SORS and was first explored by Matthew D. Keller and his co-workers at Vanderbilt University, Tennessee, USA [59]. The researchers developed a Monte Carlo code for evaluating SORS in soft tissues (e.g. breast) and compared the findings with the experimental results [60]. Different tissue geometries were adopted in order to predict the SORS signal

with varying sizes of normal and tumor layer. The results of their studies showed that using the same spatial offset it was possible to detect tumor through an overlaying normal tissue layer of much larger thickness if the thickness of the tumor was also proportionally increased. Besides the above mentioned applications, the measurement of glucose concentration in human tissues was also performed by using a novel concept of SE-SORS (Surface enhanced SORS). The concept was developed by combining the high sensitivity of surface enhanced Raman spectroscopy (SERS) in trace concentration detection with the high depth-sensitivity of SORS [62]. In this experiment, depth-sensitive Raman spectra were recorded from a SERS implant localized under skin. Following the successful demonstration of SE-SORS concept, in an independent study, glucose was detected with a root-mean-square error of calibration (RMSEC) and root-mean-square error of prediction (RMSEP) of 3.6 mg/dl and 13.7 mg/dl, respectively for low glucose concentrations (<80 mg/dl) [63]. More recently, the same concept was also employed in multiplexed imaging of tissue [64]. Multiplexed SERS signals from four different 'flavours' of nano-particles were recovered from a depth of ~20 mm in tissues. The recovered spectra were then reconstructed using the unique peak intensities of each of the nano-particles to produce false colour image.

In recent years, there is a considerable interest in developing clinically acceptable Raman spectroscopic probes using the SORS concept. For example, Schulmerich *et al.* [65] developed a fiber-optic Raman probe and used it in rat tibia. They used an axicon lens for distributing the laser power in an annulus region surrounding the field of view of a circular array of 50 collection fibers. They also slightly modified the developed Raman probe for recording the Raman spectra of Murine bone *in-vivo* [58]. More recently, Keller *et al.* [18] developed a fiber-optic SORS probe and used it in cancer tissues of breast pathology to assess its ability in evaluating surgical margin status. The developed probe has a single illumination fiber of core 400 μm and four different rings (not concentric) having a group of

identical collection fibers (core diameter = 300 µm). A probabilistic classification scheme was used to classify the measured spectra as "negative" or "positive" margins and the discrimination results were obtained with a sensitivity and specificity of 95% and 100% respectively.

In addition to the two important schemes described above in detail, there are also a few other schemes which may be configured for depth-sensitive Raman measurements from the tissue like turbid media. For example, an angled excitation-collection (AEC) [66-67] configuration may be considered. In AEC, the excitation (or illumination) is done via normal incidence and the collection is performed by an angled path with respect to the normal of the sample surface. As the obliquely incident light travels mostly in the superficial layers and the light with normal incidence penetrates comparatively deeper in the sub-surface regions, by varying the angle between the two channel paths, one can obtain the variations in the relative intensities of different peaks belonging to different sub-surface layers. The studies on the AEC configuration are found to be a few due to limited probing depth (~300 µm) and its inability of filtering the diffuse component of the light leading to poorer SNR of the measured signal [66-68]. Polarized Raman spectroscopy (PRS) has also been used for depth-sensitive measurements [28]. The underlying principle is that the light collected from the surface layer partially retains its initial polarization whereas the scattered or emitted light from the sub-surface regions is completely depolarized due to multiple scattering. The first demonstration of such measurements in fluorescence spectroscopy was presented by our group at RRCAT, Indore [69]. Smith *et al.* [28] revisited this scheme and applied in Raman spectroscopy. A notable advantage offered by this scheme is that it provides information of molecular orientation and symmetry of the vibrating bond. However, there is a rapid degradation in the SNR with the depth. The phenomena of total internal reflection (TIR) can also be used for depth-sensitive Raman [70] measurements. In this scheme, the depth-

sensitive Raman spectra can be obtained by varying the incident angle. Although, the scheme offers excellent depth resolution (~100 nm), it has been almost rejected, particularly in biomedical applications, due to complex instrumentation with bulky optics and the other stringent requirements like selection and optimization of an internal reflection element (IRE) etc. Further, the technique also fails to probe depths beyond 20 μm [70]. Kerr-gated or ultrafast temporal gating [27] may also be another technique; however, it is not suited for biomedical applications owing to the involvement of intense laser pulses. Recently, a scheme based on cone-shell illumination and cone collection has been proposed by Ong *et al.* [71-72] in order to probe depths beyond the reach of confocal detection. Though the instrumentation appealed novelty, there was no validation found in biological tissues and only the spectroscopy having higher signal strength (i.e. fluorescence spectroscopy) was configured.

1.4 Specific aims

There are two specific aims of the present dissertation:

1) To investigate the applicability of existing depth-sensitive Raman spectroscopic techniques for applications involving turbid media such as biological tissues and evaluate their relative performances in probing sub-surface depths within the media

2) To develop new depth-sensitive Raman spectroscopic techniques and evaluation of their capabilities in overcoming major limitations of the existing techniques with a view to translating them into field-deployable instruments

CHAPTER 2

Confocal Raman spectroscopy for tissue analysis

2.1 Introduction

In histopathology, the present gold standard for tissue characterization, high-resolution images of cellular and sub-cellular structures of appropriately pre-processed and stained specimens of thin tissue sections obtained by microtomy from the FFPE tissue blocks are analysed using light microscopy [41-42]. Despite its widespread use, a major limitation is that the diagnosis depends on the expert's interpretation and therefore suffers from both human as well as sampling errors [7]. In case of the tumors that are atypical or lack morphological features, the complexity level increases further. Such limitations can be overcome by the use of Raman spectroscopy as it produces molecular specific signatures ultimately suitable for the diagnosis. As discussed in the Chapter 1, many of recent research articles have shown potential of the technique in cancer diagnosis using FFPE tissue sections of various organs like cervix [43-45], ovary [46], skin [47] etc. However, a common major hurdle faced in all such studies was the orders of magnitude stronger paraffin Raman signal which swamped the rather weak tissue Raman signal. For faithful retrieval of the tissue Raman signatures from the measured Raman spectra of the FFPE tissue sections, mainly two approaches have been used, the chemical de-paraffinization [43, 46] and the mathematical de-paraffinization [44, 47, 73-75]. However, both the approaches consume a significant amount of time and require a large number of spectral measurements. Further, they are destructive due to the requirement of thin tissue sections (~5-10 μm) acquired from intact FFPE tissue blocks.

In this chapter, we present a study using confocal Raman spectroscopy (CRS) for depth-sensitive Raman spectral measurements from FFPE tissue blocks. The objective is to evaluate the feasibility of obtaining diagnostic feedback about a tissue under interrogation by measuring confocal Raman spectra from the intact FFPE block of the tissue without preparing any micro-thin tissue sections or any other processing. The confocal Raman spectra (measured using a developed CRS system) from pathologically certified, intact FFPE tissue blocks of normal and cancerous human breast tissues are recorded by moving the sample stage towards the objective lens (used for focusing the illumination beam) of the CRS system. The measured Raman spectra, highly contaminated with paraffin Raman signal, are de-paraffinized for retrieving the characteristic Raman signatures of the embedded tissues using scaled-subtraction, a non-statistical method of mathematical de-praffinization. The differences observed between the so obtained Raman spectra of normal and cancerous breast tissues are quantified using multivariate statistical analyses. The results clearly suggest that the combination of confocal Raman spectroscopy and a multivariate statistical diagnostic algorithm can be a promising tool in a clinical pathology setting for non-destructively determining the pathologic state of a tissue embedded in intact FFPE blocks.

2.2 Materials and methods

The pathologically certified FFPE blocks of breast tissue samples were obtained from the archival files of the Pathology Department of Mahatma Gandhi Memorial Medical College, Indore. Appropriate ethical permission was taken. The FFPE blocks consisted of 7 invasive ductal carcinoma and 7 normal breast tissue samples from a total of 14 different individuals. The paraffin blocks were 25 mm (L) x 22 mm (B) x 18 mm (H) in dimension. The surface dimensions of irregular shaped tissues ranged from 5 mm x 6 mm to 20 mm x 18 mm.

A schematic of the experimental setup of CRS for the depth-sensitive measurements of FFPE blocks is shown in Figure 2.1. The system utilizes a 785 nm single-mode diode laser (DL785-100-SO, CrystaLaser) as the illumination source. The laser beam is first collimated with an achromatic doublet lens (NA = 0.25, f = 36 mm). It is then spectrally purified using a laser clean-up filter (HQ782/20X, Chroma Tech. Corp.). A dichroic filter (λ_{trans}-800 nm, Semrock Inc.) kept at an angle of 45° with respect to the lens axis is used to steer the collimated beam towards a mirror kept at an angle of 45° with respect to the beam axis. The mirror reflects the collimated beam towards the sample arm where it is focused through a microscope objective lens (NA = 0.65, Comar Optics) onto the surface of the sample kept on a micrometer-controlled x-y-z stage.
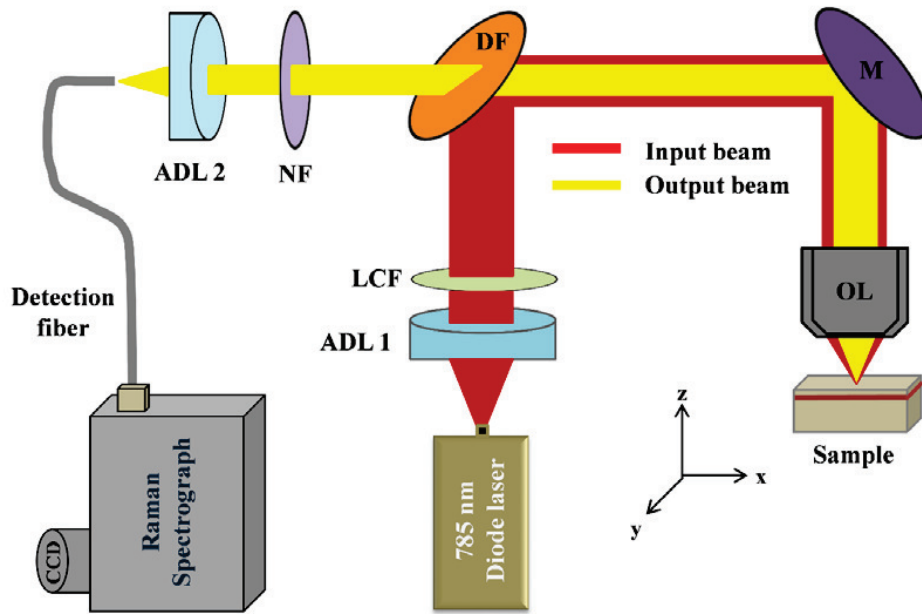
Figure 2.1: *Experimental setup of a CRS system for depth-sensitive Raman measurements from the FFPE tissue blocks. The abbreviations and their corresponding expanded forms are as follows: ADL-achromatic doublet lens, LCF-laser clean-up filter, DF-dichroic filter, M-mirror, OL-objective lens, NF-notch filter.*

The Raman signal backscattered from the sample is passed through the same objective lens, reflected by the mirror and then transmitted through the dichroic filter (passes the light

of wavelengths >800 nm) to get steered towards the detection arm of the confocal system by passing it through a notch filter (Narrow Notch-6, Tydex J. S. Co.) that filters the elastically scattered light (Rayleigh light). The filtered Raman output is focused by another achromatic doublet lens (NA = 0.25, f = 36 mm) onto an optical fiber of core size 100μm (QMMJ-55-IRVIS-100/140-0.3, OZ Optics Ltd.). The fiber finally couples the output to the entrance port of an imaging spectrograph (Acton SP2300, Princeton Instruments) equipped with a CCD camera (Pixis 100, Princeton Instruments).

The depth resolution of the developed confocal Raman system was estimated by measuring the Raman spectra of a 10 μm thick sheet of poly(methyl methacrylate) (PMMA) at different axial positions of the focused laser beam around the focus. For estimating the size of the focal point, the same PMMA sheet was used. The detailed procedure for measuring the depth resolution as well the lateral diameter of the focused beam can be found elsewhere [20]. The depth resolution and diameter were found to be ~50 μm and ~7 μm respectively. The SNR of the system, defined as the ratio of the maximum intensity of the signal to the baseline noise, was calculated as SNR = (signal maximum-signal minimum)/(baseline standard deviation in non-Raman region) and found out to be ~600 for the 1382 cm^{-1} naphthalene Raman peak for an integration time of 1s.

For the measurement of Raman spectra from the various depths of a FFPE tissue block, the focal plane of the Raman excitation beam was shifted axially (in z-direction) by moving the tissue block kept on the micrometer-controlled stage along the axial direction. For generating good quality Raman spectra, the integration time used was 10 s. The optical power at the target sample was measured to be ~50 mW.

2.3 Data pre-processing and scaled subtraction

For each measured Raman spectrum, the wavenumber axis was calibrated with the illumination laser line, acetaminophen and naphthalene standards, and the spectrum was truncated over the spectral region 800-1800 cm^{-1}. A blank spectrum (considered as the dark signal) acquired in absence of any light source prior to spectral measurements in actual samples was subtracted from the sample spectra. The subtracted spectra were then corrected for the spectral response of the system by using an NIST (National Institute of Standards and Technology) traceable calibration lamp (LS-1, Ocean Optics) [76]. The corrected spectra were then fed to a range independent background subtraction algorithm (RIA) [77] in order to eliminate the fluorescence background. For isolating the tissue specific Raman signatures buried in the Raman signal of paraffin, a method of scaled subtraction was developed. This method requires at its input at least two spectra which have one or more non-overlapping spectral regions. For instance, if S_1 and S_2 are the two Raman spectra and at least one of them has the Raman peaks corresponding to two different components with the assumption that the peaks (at least one, if not all) have different spectral positions, then the pure Raman spectrum (PRS) of one component can be extracted using the following formula –

$$PRS = \alpha S_1 - \beta S_2 \qquad \qquad ......\ 2.1$$

where α is the ratio of Raman peak intensity (corresponding to one component) and the integrated intensity over the entire spectrum. The other factor β for the second spectrum is also defined in the same way, however, the Raman peak intensity is taken for the other component. Moreover, the factor, α is estimated for S_2 and the β is calculated for the other spectrum i.e. S_1. In the present case, the mean Raman spectrum of paraffin, obtained from backside (containing only paraffin) of an FFPE tissue block, was subtracted from each of the measured depth-sensitive Raman spectrum of that particular tissue block after scaling the

peak intensity of the 1135 cm^{-1} Raman band (unique to paraffin) of this spectrum to the same height as that of the paraffin Raman spectrum.

2.4 Data analysis

The use of depth-sensitive Raman spectra for discrimination of cancerous and normal tissues in the FFPE blocks requires a diagnostic algorithm which seeks to extract the diagnostic features from the measured set of spectra and classify them into appropriate pathologic categories. A probability based multivariate diagnostic algorithm was developed for analyzing the diagnostic content of the depth-sensitive Raman spectra measured from the different FFPE tissue blocks. The algorithm development consisted of two steps: i) feature extraction (or dimensionality reduction) through PCA and ii) probabilistic classification via SMLR. These techniques have been described in detail elsewhere [78-80]. In brief, PCA [78] is a linear feature extraction procedure aimed to find a set of linear transformations on the input data that contains the maximum information about the data in a reduced dimensionality space. SMLR [79] computes the posterior probabilities using a multinomial logistic regression model and constructs a decision boundary that separates the data into its constituent classes based on the computed posterior probabilities following the Bayes' rule. All the discrimination analyses were performed using leave-one-block-out cross validation. To do so, the Raman spectra corresponding to any one block were excluded and regression vectors were estimated for the spectra of the rest blocks and then using the estimated regression parameters the spectra of the left out block were reconstructed. The predictive accuracies of the diagnostic algorithm used for different classification tasks were calculated with respect to histopathology report as the reference gold standard.

2.5 Results and discussions

The Raman spectra were measured from the different depths of the FFPE tissue blocks by axially varying the focal spot of the illumination beam in steps of 10 μm for 0-200 μm depth, 20 μm for 200-300 μm depth and 50 μm for higher depths of up to ~500 μm. Figure 2.2a shows the typical depth-sensitive Raman spectra measured from a cancerous FFPE tissue block chosen at randomly from among the seven different blocks belonging to the same pathology. Similarly, Figure 2.2b shows the typical Raman spectra measured from a normal FFPE tissue block randomly selected from among the remaining seven blocks of normal breast tissues. The spectra in each of the tissue blocks were measured at two different lateral positions separated by ~0.5 mm from each other.
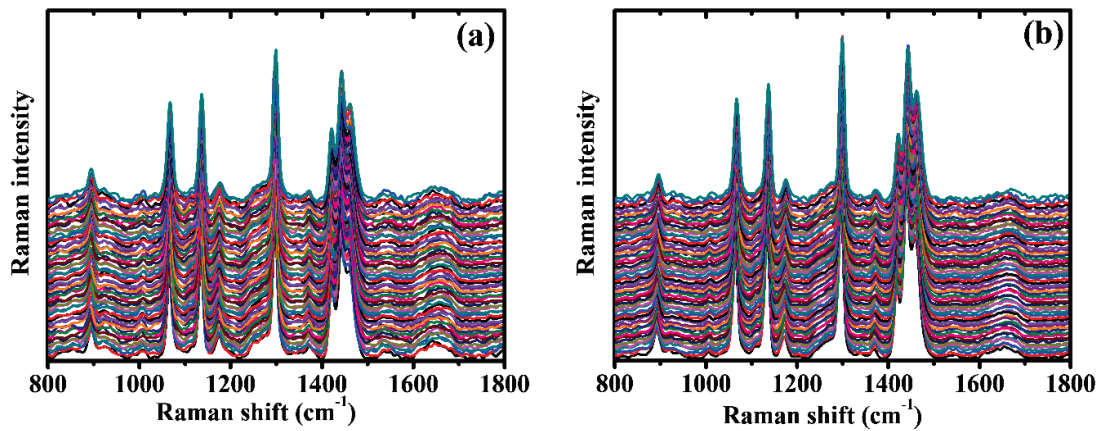
Figure 2.2: *Raman spectra corresponding to different depths (in steps of 10 μm for 0-200 μm depth, 20 μm for 200-300 μm depth and 50 μm for higher depths of up to ~500 μm) of (a) a cancerous and (b) a normal FFPE tissue block measured at two different lateral sites. The spectra are shown with offset for clarity.*

Figure 2.3a shows the conventional Raman spectrum of native paraffin (comprising the tissue blocks) measured with the same experimental set-up. The spectrum is the average of the spectra measured from the non-tissue containing portion of a total of 14 FFPE blocks. For each block three spectra were recorded from three different lateral positions containing

only paraffin but no tissue. It is evident from the Figures. 2.2a and 2.2b that the Raman spectra of the FFPE tissue blocks at all the depths irrespective of the tissue type are dominated by the Raman signatures of paraffin except at ~1650 cm^{-1} where the tissue Raman band is present and believed to be due to proteins (amide-I) [7, 43, 81]. However, the band does not seem to reveal any inter-category differences apparently being masked by the presence of the strong paraffin Raman bands.
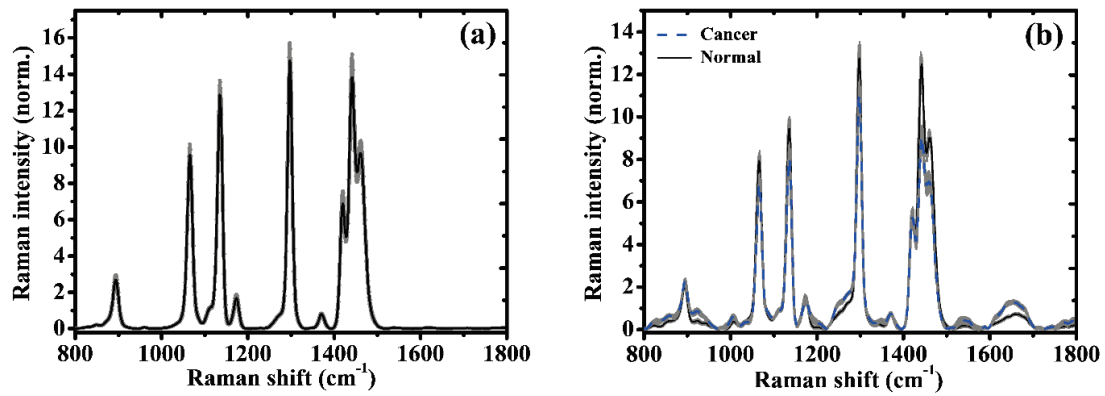
Figure 2.3: *(a) Raman spectrum of paraffin (comprising the tissue blocks). The spectrum is the average of the spectra measured from the non-tissue containing portion of a total of fourteen FFPE blocks with each block containing three lateral measurement sites. (b) Mean Raman spectra of cancerous (dashed line) and normal (solid line) FFPE tissue blocks obtained by averaging the respective set of spectra shown in Figures 2.2a and 2.2b. The error bars shown in grey represent ±1 standard deviation.*

Figure 2.3b shows the mean Raman spectra of cancerous and normal breast tissue types obtained by averaging the respective set of spectra of each of the Figures 2.2a and 2.2b corresponding to cancerous and normal FFPE tissue block. It is certainly apparent from the figure that the intensity of the 1650 cm^{-1} band is enhanced and this is consistent with that reported in literature [7, 81], in the cancerous as compared to that in the normal FFPE tissue block. Similarly, the intensity of the Raman peak ~1265 cm^{-1}, believed to be due to amide-III [7, 43, 81], is also seen to be higher in cancerous relative to the normal breast tissue block.

As the depth at which the tissue was embedded in a FFPE tissue block was not known and visibly seen to vary across the blocks investigated, it was imperative to locate by some means the axial position of the tissue in each FFPE block. In order to do that we devised a scheme which sought to find out, in each tissue block, the subset of spectra (from among the whole set of measured depth-sensitive Raman spectra) that contained the most of the tissue specific Raman signatures. Since the Raman bands around 1650 cm^{-1} and 1135 cm^{-1} are known primarily to be characteristics of tissue and paraffin respectively, the ratio of the peak intensities at these two wavenumbers (i.e. I_{1650}/I_{1135}), indicative of the content of tissue Raman signatures in the spectra, was plotted against the axial positions for the whole set of depth-sensitive spectra measured in each block.
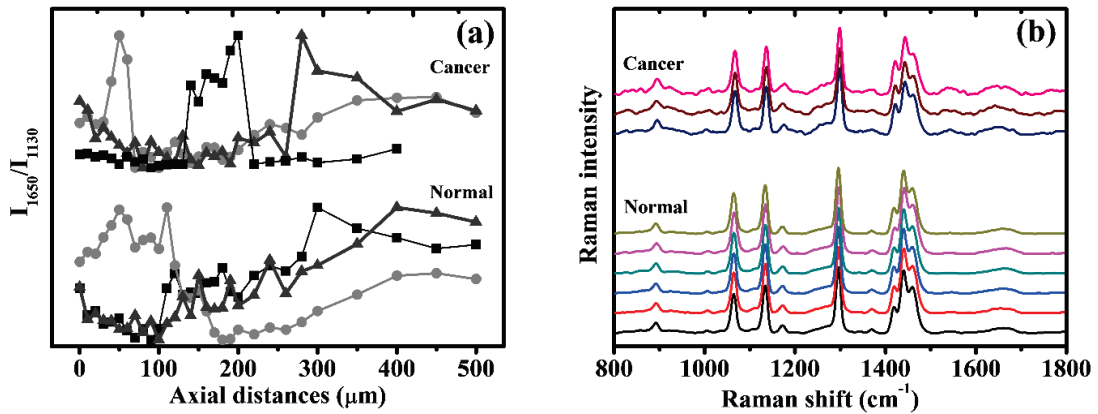
Figure 2.4: *(a) Plot of the ratio (I_{1650}/I_{1130}) versus the axial position for the set of spectra of three cancerous (upper panel) and three normal (lower panel) tissue blocks chosen at random from among the fourteen tissue blocks. (b) Shortlisted spectra (most representative of tissue) corresponding to the Raman spectra shown in Figures 2.2a and 2.2b. The spectra are shown with an offset for clarity.*

Figure 2.4a shows the plot of the ratio verses the axial position for the set of spectra of three cancerous and three normal tissue blocks chosen at random from among the fourteen tissue blocks. One can observe that irrespective of the blocks investigated, the ratio increases first, reaches a maximum and then decrease implying that the spectra corresponding to the

maximum ratio contain the best tissue-specific signatures. Further one can also see that the maximum ratio occurs at different axial positions for the different FFPE tissue blocks signifying the variation in the subsurface positions of tissue in the different blocks. In order to find out the set of spectra that is most representative of tissue, only those spectra in each block were retained for which the ratio was ≥90% of their respective maxima. Figure 2.4b shows the shortlisted spectra (most representative of tissue) corresponding to the tissue blocks whose depth-sensitive Raman spectra are shown in Figures 2.2a and 2.2b.

In order to de-paraffinize the measured Raman spectra, the full set of depth-sensitive Raman spectra of the FFPE tissue blocks was subjected to the method of scale-subtraction as described earlier in this chapter. Figure 2.5a shows the Raman spectra retrieved through scale-subtraction from the spectra shown in Figure 2.4b. It is apparent from the figures that the retrieved spectra resemble the typical Raman spectra of breast tissues reported in literature [81] except for the few sharp spikes with intensities extending even in the negative. These spikes are the unavoidable artefacts that result during scale-subtraction from those parts of the characteristic paraffin Raman bands which slightly differ in line shape than that of the corresponding paraffin Raman bands contained in the Raman spectra of the FFPE tissue blocks and as a result do not have complete overlap with their contours. Though appropriate spectral smoothening can reduce the height of these spikes or even eliminate them in some situations but the process almost flattens many of the tissue specific spectral signatures resulting in further distortions in the scale-subtracted spectra. Figure 2.5b shows the average scale-subtracted spectra corresponding to those shown in Figure 2.5a. One may note that significant spectral differences which otherwise were completely masked before scale-subtraction are now explicit in all the Raman bands of the tissue types. For example, significant spectral variations are seen around 1100 to 1300, 1440 and 1650 cm^{-1} and these

correspond to biochemical differences inherent in the different breast tissues, notably connective tissue proteins, and fatty acids [7, 81].
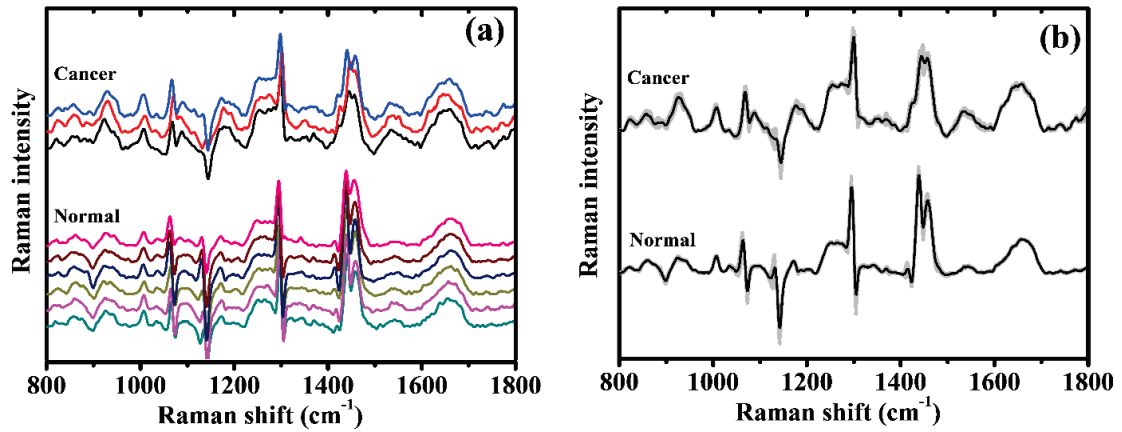
Figure 2.5: *(a) Raman spectra of cancer (upper panel) and normal (lower panel) breast tissues retrieved through scale-subtraction from the shortlisted spectra shown in Figure 2.4b. The spectra are shown with an offset for clarity. (b) Mean scale-subtracted Raman spectra of cancerous (upper panel) and normal (lower panel) breast tissues obtained by averaging the respective set of spectra of the tissue types shown in Figure 2.5a. The error bars shown in grey represent ±1 standard deviation.*

The ratios of peak intensities at 1650 cm^{-1} and 1450 cm^{-1} (i.e. I_{1650}/I_{1450}), estimated from the whole set of scale-subtracted spectra of the tissue types and reflecting the relationship between relative protein and lipid content, were found to be significantly (p<0.05) different in normal as compared to the cancerous tissue spectra. It is pertinent to mention here that this observation is in accordance with that reported in literature [7, 81] where it has also been proposed as an index for discriminating cancerous from normal breast tissues. For assessing the ability of I_{1650}/I_{1450} for possible discrimination between tissue types in the present case, its values were used as input to a nearest-mean classifier (NMC). Table 2.1 shows the discrimination results obtained with the values of I_{1650}/I_{1450} as input to a NMC employed in a leave-one-block-out cross validation mode. The results are shown with different parameters like sensitivity, specificity, positive predictive value (PPV), negative

predictive value (NPV) and overall accuracy. It can be seen that the values of sensitivity and specificity towards cancer are ~77% and 56%, respectively.

Table 2.1: *The discrimination results obtained using the NMC with the values of the ratio I_{1650}/I_{1450} as its input. The results are based on leave-one-block-out cross validation.*

Classification algorithm	Sensitivity (N=22)	Specificity (N=18)	PPV (N=25)	NPV (N=15)	Overall accuracy (N=40)
Ratio (I_{1650}/I_{1450}) - NMC	77%	56%	68%	67%	68%

In order to evaluate the diagnostic content of the whole range of normalized intensities contained in the Raman spectra measured from the FFPE tissue blocks, the full set of shortlisted (most representative of tissue) scale-subtracted spectra of the tissue blocks was subjected to the input of the PCA-SMLR based probabilistic multivariate diagnostic algorithm developed for this purpose. The task of the algorithm was to classify the tissue spectra into two pathologic categories: cancerous and normal. PCA of the set of shortlisted scaled-subtracted spectra resulted in 40 principal components that collectively accounted for 99.9% of the total variance of the spectral data. Of these forty principal components, only six (having largest eigen-values and accounting for ~90% of the total variance) were retained since they were found to yield optimum classification between the tissue types using the SMLR based classification. Table 2.2 shows the classification results obtained based on leave-one-block-out cross validation of the PCA-SMLR algorithm on the entire data set. The results show an excellent ability for the depth-sensitive Raman spectra to evaluate pathology status in FFPE tissue blocks, with 96% sensitivity and 100% specificity, and an overall classification accuracy of 98%. Alternatively, the discrimination was performed with 95% NPV and 100% PPV. For the sake of comparison, the discriminations results obtained using the values of I_{1650}/I_{1450} as input to the SMLR classifier are also listed in Table 2.2. One can

see that the sensitivity and specificity values (59% and 72% respectively) yielded by the single-variate algorithm are significantly poorer as compared to the PCA-SMLR based multivariate algorithm.

Table 2.2: *The discrimination results obtained (i) using PCA-SMLR applied on the shortlisted set of scale-subtracted, depth-sensitive Raman spectra of the FFPE tissue blocks of pathologically certified cancerous and normal breast tissues and (ii) using SMLR with the ratio I_{1650}/I_{1450} as its input.*

Classification algorithm	Sensitivity (N=22)	Specificity (N=18)	PPV (N=25)	NPV (N=15)	Overall accuracy (N=40)
PCA-SMLR	96%	100%	100%	95%	98%
Ratio (I_{1650}/I_{1450}) - SMLR	59%	72%	72%	59%	65%

In addition to assigning class labels, the PCA-SMLR based diagnostic algorithm also yielded posterior probabilities of the measured tissue sites belonging to each class of breast tissues. Figure 2.6 illustrates the posterior probabilities computed by the algorithm for the measured tissue spectra of each tissue class of belonging to cancer. While the open symbols in the figure represent probabilities of correct class-membership, the closed symbols denote the probabilities for the misclassified tissue sites. The figure indicates that 96% of the cancerous breast tissue sites have a posterior probability >0.5 and 100% of the normal breast tissue sites have a posterior probability <0.5. A further examination of the figure reveals an interesting observation. While all the normal tissue sites are seen to have a posterior probability <0.2 of being cancer, only 20 out of 22 of the cancerous sites are found having a posterior probability >0.8. Of the remaining two cancerous sites, while one is seen to have a probability of ~0.65 of being cancer, the corresponding probability for the other is seen to be exceedingly low (<0.1). This is not quite unusual because while the presence of any amount

cancerous cells is not expected in a normal breast tissue, the reverse is not true. A piece of cancerous tissue, due to its very heterogeneous nature, might contain variable amount of normal cells at some isolated locations across the investigational volume which otherwise is cancerous. A further proof towards this is the fact that the sensitivity was seen to rise to 100% (with the posterior probability >0.8 for all) when the discrimination analysis was carried out on the basis of "averaged-spectrum-per-block" by applying the algorithm on the spectral data obtained by averaging over the shortlisted set of spectra in each of the cancerous and normal tissue blocks thereby generating a single spectrum per block.

Figure 2.6: *Posterior probabilities of belonging to cancer for the scaled-subtracted spectra of each tissue category as computed by the PCA-SMLR algorithm. The open symbols represent probabilities of correct class-membership (true positives and true negatives) and the closed symbols denote the probabilities for misclassification (false positives and false negatives).*

At present, there exists no method for determining the pathologic state of a paraffin embedded tissue without preparing micro-thin slices from an intact FFPE tissue block and subjecting it to further processing. The present study is a step towards investigating the feasibility of such a task using the technique of Raman spectroscopy. The goal of the present

study is to explore the capability of CRS for discriminating the cancerous from normal human breast tissues based on depth-sensitive measurement of Raman spectra from the intact FFPE tissue blocks. Such an approach is all the more desired because it is completely non-destructive as it eliminates the need to prepare micro-thin tissue slices thereby enabling preservation of the tissue blocks intact for further use in future in case any re-assessment is required.

The depth-sensitive Raman spectra measured from the FFPE blocks of pathologically certified cancerous and normal breast tissues were found to be severely contaminated (see Figures 2.2a and 2.2b) by the Raman signatures of paraffin whose Raman cross-section is known to be significantly higher than that of the biological tissues. In order to eliminate the paraffin Raman background and isolate the weak tissue Raman signatures buried in it, the Raman spectrum of paraffin measured from the non-tissue containing region of the block was scaled-subtracted from the measured depth-sensitive Raman spectra of the FFPE tissue blocks. The method was found to satisfactorily recover the Raman spectra characteristic of breast tissues by cancelling out the spectral contributions of paraffin contained in it. It is important to mention here that mathematical de-praffinization was earlier attempted by the Michel Manfait group [47, 73-74]. They employed independent component analysis (ICA) to first generate model sources of paraffin from the set of measured micro-Raman spectra of the micro-thin tissue sections and then used these model paraffin spectra along with the set of micro-Raman spectra, from which they were derived, as input to a non-negatively constrained least-squares method [47, 73-74] for obtaining de-praffinized Raman spectra of tissues. However, the major disadvantage of this approach is that ICA being based on the theory of statistical pattern recognition requires an array of Raman spectra at its input for generating the model source spectra of paraffin. Further, the scale of accuracy of the source spectra is dependent on the size of the input Raman spectral data which needs to be larger than the data

dimension (i.e. number of wavenumbers) to satisfy the validity criteria of ICA. In contrast, the present method of mathematical de-praffinization employed by us is non-statistical and requires only two spectra, a paraffin Raman spectrum which can be easily obtained from the non-tissue containing part of the FFPE tissue block and a depth-sensitive Raman spectrum measured across the tissue containing portion of the block.

It is also important to mention here that instead of using the mean paraffin Raman spectrum obtained by averaging all the paraffin Raman spectra of the different FFPE blocks investigated, the mean paraffin Raman spectrum of an individual FFPE block was used for generating the scale-subtracted spectra from the measured set of depth-sensitive spectra from that block. This is to minimize the effect of the observed inter-block variability (~9-20%) of the line-shapes of the paraffin Raman bands on the outcome of scaled-subtraction. However, the scaled-subtracted spectra still showed a few sharp spikes with intensities extending even in the negative (Figure 2.5a). These are unavoidable because during scaled-subtraction even a very subtle mismatch between the line shape of the characteristic paraffin Raman bands appearing in the spectra measured from non-tissue and tissue containing part of the FFPE block is bound to lead to this kind of artefacts. Though a direct comparison is not possible, it is pertinent to mention here that the de-paraffinized spectra obtained by the Michel Manfait group [47, 73-74] using non-negatively constrained least square method also had similar sharp spikes across the spectral range. However, these artefacts were observed to have no bearing on the results of discrimination.

In order to discriminate the FFPE tissue blocks two different approaches were taken. Under the first approach, there were two sub-approaches. The first sub-approach was empirical wherein a geometric classifier (nearest mean classifier) was used and the values of the ratio of intensities at 1650 cm^{-1} and 1450 cm^{-1} (i.e. I_{1650}/I_{1450}) computed from the measured set of spectra were used as input to the classifier. The second sub-approach was a

mix of empirical and statistical wherein an SMLR based classifier was applied on the same set of ratio values as its input. In the second approach, which was purely statistical, the normalized Raman intensities over all the wavenumbers were used as an input to a multivariate statistical diagnostic algorithm developed based on PCA and SMLR. The objective of the first approach was to evaluate the discrimination efficacy of the intensity ratio that was observed to be significantly different for the cancerous FFPE tissue block than the normal. The advantage of using such a diagnostic feature based only on the intensity ratio is that it could considerably simplify the experimental arrangement since no spectral resolution is required. The second approach exploits the total spectral information content of the full range of spectral data. The results (Table 2.2) clearly indicate that multivariate algorithms based on PCA-SMLR provides significantly improved discrimination accuracy. This is quite expected because in contrast to the case where the classifier (either geometric or statistical) uses only a single spectral variable (e.g. the ratio of intensity), PCA-SMLR uses multiple Raman bands over the full range of wave-numbers thereby exploiting significantly more information useful for discrimination.

Classification error is the ultimate measure of performance of a diagnostic algorithm and it strongly depends on the mathematical formulation of the algorithm. In practice, the classification error is estimated from all the available data that include both the training and validation sets [80]. An algorithm is considered robust when it can provide a reliable estimate of classification error independent of the sizes of both the training as well as the validation set data. This depends on the ability of the algorithm to eliminate the high degree of multi-collinearity that is usually present in the measured spectral data whose dimension is higher compared to its size (i.e. the number of measurements). The major advantage of using the SMLR based classification is that it can mitigate this collinearity problem [79-80] and therefore, can perform classification from a set of test data of any size and dimension with

sufficient accuracy. The additional advantage of the algorithm is that it also predicts the posterior probability of tissues belonging to a specific diagnostic category thus allowing one to quantitatively assess the certainty of classification [79-80]. This is apparent from Figure 2.6 where the posterior probabilities (of being cancer) as predicted by the PCA-SMLR algorithm are plotted for the scaled-subtracted, depth-sensitive spectra of FFPE tissue blocks. Knowledge of the posterior probability of class-membership is useful in a clinical pathological setting because it would allow to reassess those sites that are classified with higher relative uncertainty, provide the opportunity to improve performance by rejecting more ambiguous data points, cause an optimal compensation for asymmetric misclassification costs and varying class proportions and allow for the fusion of outputs with other probabilistic sources of information before applying the decision criteria.

An important task while using a diagnostic algorithm is to evaluate the generalized classification ability of the algorithm. It was thus required to make sure that the validation set data was fully independent of the training set data i.e. it should not contain any of the pieces of the training set data with which the algorithm was trained and optimized. The independence was ensured by following the leave-one-block-out cross validation method. In this method, for each of the N (= 14) blocks of Raman spectra, spectra of N-1 (= 13) of them were used to train the algorithm and the set of spectra of the remaining block was left excluded (and therefore not used by the algorithm during calibration) as the validation set. This was repeated N times (until the spectra of all the withheld blocks were predicted) each time excluding a different block for the purpose of validation and retraining the algorithm using spectra of the rest of the blocks. Since the training set data remained completely independent of the test data in each of the N loops (as the set of spectra from a block was never a part of both the training and the validation sets simultaneously), the validation was

statistically unbiased. Thus, classification results obtained in the present study can be considered reliable in predicting future classification performance.

2.6 Summary

To summarize, we have presented details of a study carried out for evaluating the applicability of CRS to discriminate cancerous and normal breast tissues using the depth-sensitive Raman spectra measured from the FFPE tissue blocks. The important attraction of the approach is that it enables tissue analysis using intact tissue blocks without requiring preparation of any thin tissue sections or any other processing, and is also capable of providing a quantitative diagnostic feedback. Use of a diagnostic algorithm developed using the framework of PCA and SMLR provided a sensitivity of 96% and a specificity of 100% towards cancer based on leave-one-block-out cross validation. The results of the present work indicate that the combination of CRS and a multivariate statistical diagnostic algorithm could be a promising tool in a clinical pathology setting for non-destructively determining the pathologic state of a tissue embedded in intact FFPE blocks. Despite the encouraging results, one practical problem encountered with the CRS based approach was that the objective lens would often touch the surface of the target sample while probing its sub-surface depths. The limited probing depth (~200-300 μm) was found to be as an additional drawback. In the next chapter, a depth-sensitive Raman technique for overcoming such limitations is described.

CHAPTER 3

Reverse confocal polarized Raman spectroscopy for

tissue analysis

3.1 Introduction

In the previous chapter, we showed how a CRS system can be used for depth-sensitive Raman measurements from intact FFPE tissue blocks without requiring preparation of any micro-thin tissue sections or any other processing. For implementing such a non-destructive way of determining the pathologic state of a tissue embedded in the intact FFPE blocks, the Raman spectra from the various depths of a given block were measured by moving the sample stage towards the objective lens (used for focusing the illumination beam) of the CRS system. Notwithstanding the encouraging results, one practical problem faced in such measurements is that the objective lens often touches the surface of the target sample while probing its sub-surface depths. Such lens-sample contact must be avoided because this not only results in deviation of lens's optical behaviour, but also may damage the lens permanently if the sample is of reactive nature. In practice, a cover slip is generally used in between the sample and the lens in order to protect the lens. However, most of the cover slips show significant background fluorescence generated due to their material (e.g. glass) which overwhelms the comparatively weaker Raman signal of the target sample [25-26]. For biological tissues, the situation worsens further as they itself have strong fluorescence and very low Raman cross-section [1-8, 77, 82]. Although selection of a suitable material for the cover slip may overcome the issue to an extent, an ideal material providing a perfect solution

is not found yet [25-26, 33, 83]. An additional problem with CRS is that one cannot measure Raman signal beyond a certain depth of the target sample. For a given sample, the overall probing depth primarily depends on the two factors, first, NA of the objective lens and second, the available distance between the lens's exiting surface and the sample surface i.e. the working distance. A high NA objective lens is generally used for obtaining Raman spectra with improved spatial resolution, however, its ability of probing deep inside the sample degrades sharply. On sacrificing the resolution through the use of a low NA objective lens, though the probing depth can be improved a bit, yet interrogating a depth beyond ~200-300 μm in a typical biological tissue seems impossible [34-37].

In this chapter, we present the results of a study carried out using an alternate depth-sensitive Raman spectroscopic technique which overcomes the above mentioned drawbacks of the CRS based approach. In this technique, we perform Raman measurements by moving the focal plane of the illumination beam away from the tissue surface, unlike in CRS where it is moved across the different depths of the target tissue. Since this scheme requires the sample stage to be moved in a direction opposite to that in CRS, the technique is christened reverse confocal Raman spectroscopy (RCRS). The technique is further combined with a scheme of plane polarized illumination and orthogonal polarized detection to develop a new technique called reverse confocal polarized Raman spectroscopy (RCPRS). The evaluation of the performance of the RCPRS technique using a two-layered non-biological phantom with varying thicknesses of its surface layer and a two-layered biological tissue is detailed in the chapter.

3.2 Principles of RCRS and RCPRS

The basic principle of RCRS detection can be understood from Figure 3.1. In the figure, a lens focuses laser beam onto a point, say F, (path is shown by red coloured lines) lying above the surface of a two-layered sample and at a distance Δz from the surface. Such focusing makes a defocused circular illumination with its centre being at C. The radius of the illumination zone is assumed to be $\Delta z'$.
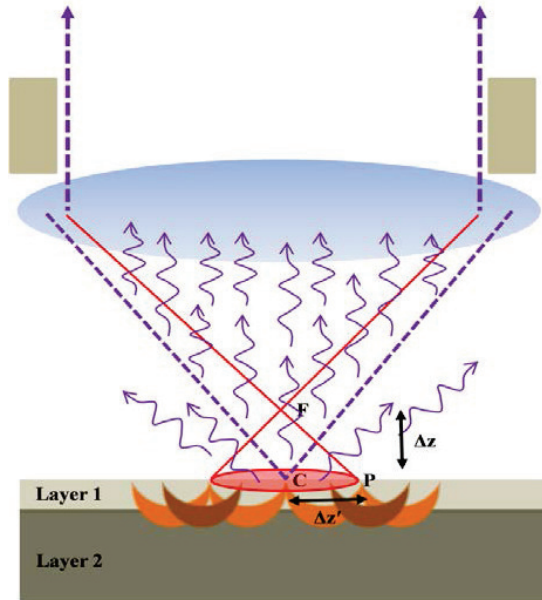
Figure 3.1: *Geometrical sketch to understand the principle of RCRS*

The light-photons emanating from each point of the illumination zone traverse inside the sample and follow their trajectories governed by absorption and scattering properties of the two layers of the sample. While absorption causes loss of a photon, scattering randomizes direction of the photon [24, 84]. In the visible and near infrared region of the electromagnetic spectrum, biological tissues predominately show forward scattering of light-photons [85-95]. Taking into account of such scattering, it has been shown that the overall trajectory of the photons emanating from any point of the illumination zone (onto the sample surface) is

generally of banana shaped [17-18, 89-94]. For few points, such banana shaped trajectories are shown in the figure. Considering one such point, say P, one can see that the photons incident at this point, traverse from layer 1 to layer 2 and return back to the sample surface at the centre of the illumination zone i.e. at the point C. during the travel they are influenced more from the layer 2 and thus they are expected to have a larger contribution of the Raman signal originated from the layer 2, while returning back to the surface. Though the photons may also exit from the points lying outside illumination zone, such exiting points can be ignored as the photons coming out from these points will not be collected by the lens. The lens will collect only those photons which would fall in its collection cone. The most effective collection cone for the lens will be the one for which the vertex lies at point C. In the figure, this effective collection cone is traced by violet coloured dashed lines. Now, on envisaging all the possible trajectories of the photons incident on different points of the illuminating circular region, it can be easily understood that the photons which are incident immediately close to the centre of the circle (whose number is obviously less) would generate Raman photons primarily in the layer 1, and the photons incident away from the centre (whose number is significantly more) would generate Raman photons primarily in the layer 2. As a result, the net Raman signal collected through the lens, following incidence of a circular illuminating beam on the sample surface, will always contain more Raman photons from the layer 2 as compared to from the layer 1. Because of this fact, the detection of sub-surface Raman signal is possible in RCRS, even though the illumination beam is focused above the sample surface. Further, if the point of focus, F, moves away more from the sample surface, the peripheral region of the circular zone increases, leading to an increase in the contribution of the Raman signal corresponding to the layer 2 and thereby enabling depth-sensitive Raman measurement.

RCPRS is a combined scheme of RCRS and orthogonal polarized Raman detection. As we have mentioned in Chapter 1 that on shining a beam of polarized light on a layered turbid sample, the light coming from its top layers partially retains its polarization state due to undergoing a few or no scattering events, whereas the light emanating from the bottom layers gets completely depolarized due to undergoing multiple scattering events. This principle, therefore, can be used to probe sub-surface depths by measuring the spectra with polarization which is either parallel or perpendicular to the inherent polarization of the illuminating light. This is illustrated in Figure 3.2. A polarizer, P1, introduced in the illumination path of a given Raman system selects a particular polarization based on the orientation of its axis with respect to the illumination beam. Another polarizer, P2, is placed in the detection arm of the system and is called analyzer. If the polarizing axis of the P2 is co-aligned with the axis of P1 then the Raman signal originating from surface layer, for which the polarization is retained, will be detected. In contrast, if the two axes become mutually orthogonal, the Raman signal belonging to the sub-surface layer for which the polarization memory is completely lost (due to the effect of multiple scattering) will be passed through the analyzer, P2. For developing a RCPRS scheme of depth-sensitive Raman detection, a polarizer can be put in the source arm of the RCRS setup and an analyzer can be kept in the detection arm of the setup.
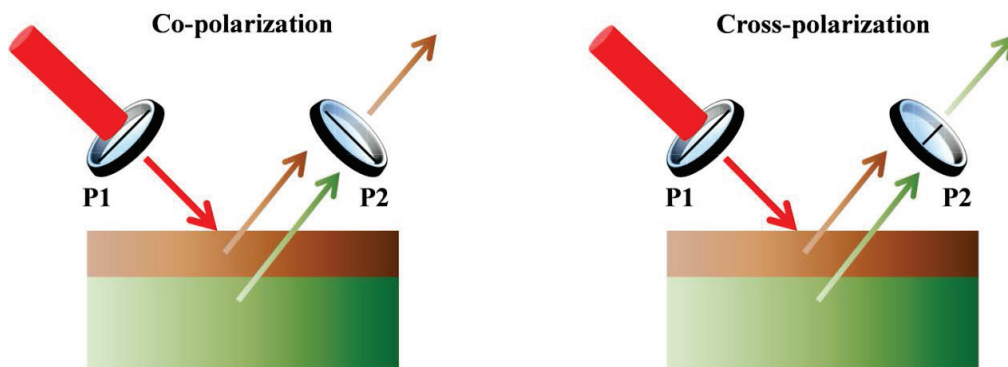
Figure 3.2: *The scheme of co- and cross-polarized Raman detection*

3.3 Materials and methods

Figure 3.3 shows the experimental arrangement of the RCPRS system developed for depth-sensitive Raman measurements. The output of a single mode diode laser (CL-2000, CrystaLaser) with central wavelength 785 nm is first collimated by an achromatic doublet lens, ADL (AC254-050-B-ML, Thorlabs Inc.) and then is passed through a laser clean-up filter, LCF (HQ782/20X, Chroma Technology Corp.) to get a spectrally purified beam.
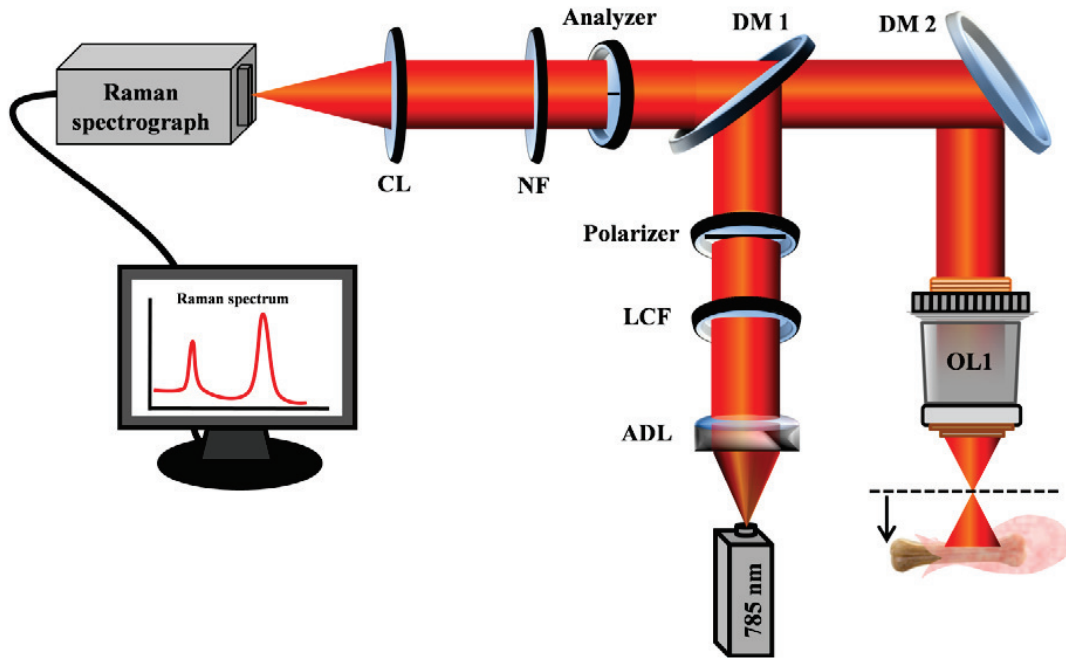
Figure 3.3: *Experimental arrangement of the RCPRS system used for depth-sensitive Raman measurements.* *The abbreviations as follows: ADL-Achromatic doublet lens, LCF-laser clean-up filter, DM–dichroic mirror, OL-objective lens, NF-notch filter and CL-convex lens.*

The purified collimated beam is linearly polarized using a polarizer (Osaka CPL 77 mm, Japan) and guided towards the sample arm of the system using two dichroic mirrors, DM1 (LPD02-785RU-25, Semrock, Inc.) and DM2 (DMLP1180, Thorlabs Inc.). Both the dichroic mirrors are kept at an angle of 45º with respect to the axis of the incoming laser beam. In the sample arm, by the use of a microscope objective lens, OL1 (10OM25, Comar

Optics Ltd.) the beam is focused on the sample kept on an x-y-z translation stage. The Raman signal backscattered from the sample is transmitted through the same objective lens and is guided towards the detection arm of the system with help of the two dichoric mirrors (DM1 and DM2) mentioned above. In the detection arm, another polarizer known as analyzer (03 FPG 003, Melles Griot) is used for changing the polarization of the backscattered signal. A notch filter, NF (Narrow Notch–6, Tydex J. S. Co.) eliminates the Rayleigh scattered component and allows to pass only in-elastically scattered light. Through the use of a convex lens, CL of focal length 50 mm, the Raman signal is finally fed to an imaging spectrograph (SR-303iA, Andor Shamrock) equipped with a thermoelectrically cooled, back-illuminated, deep-depletion CCD camera (DU416A-LDC-DD, Andor) for acquiring the Raman signals.

For carrying out the depth-sensitive Raman measurements, initially, no polarizer and analyzer were used and the z-position of the sample was fixed in such a way so that the focus of the illumination beam rested on the sample surface. This particular position of the illumination beam was called zero axial offset. The z-position of the sample was then varied in both directions around the focus. For CRS measurements, the focus of the beam was brought below the sample surface, and for the RCRS measurements, the focus was shifted above and away from the sample surface. The z-displacements of the sample from the zero axial offset were noted as non-zero axial offsets with their numerical values being equal to those displacements. For implementing the RCPRS measurements, above described procedure for RCRS is repeated in presence of the polarizer-analyzer assembly.

For the depth-sensitive Raman measurements using the three schemes mentioned above, a two-layered non-biological phantom was prepared. The non-biological phantom was designed by placing a polystyrene layer of thickness 240 μm on a 30 mm thick Teflon substrate. The measurements were also made for the two additional thicknesses (80 μm and 400 μm) of the top layer. For validating the RCPRS scheme of Raman detection, a two-

layered biological tissue was also considered. The tissue was a chicken tibia and had a bone embedded in a relatively thin muscle layer (thickness ~500 μm).

The details of the Raman spectral measurements and the data pre-processing steps like dark noise removal, background subtraction, normalization etc. have been described in the Chapter 2. The optical power measured at the focus of the objective lens was found to be 50 mW and was kept constant while comparing the RCPRS and RCRS schemes of Raman detection. The acquisition times were 5 s and 10 s for non-biological phantom and biological tissue respectively.

3.4 Results and discussions

Figure 3.4a shows the RCRS spectra of the non-biological phantom prepared with the 240 μm thick polystyrene. The spectra are measured from three different axial offsets; 0, 5.8 and 17.8 mm respectively. The reference Raman spectra of individual layers of the phantom measured from authentic samples of polystyrene and Teflon, are plotted in Figure 3.4b. In the figure, two prominent Raman peaks of Teflon, found at 725 and 1375 cm^{-1}, are marked by a star symbol. The prominent Raman peak of the polystyrene is seen at 995 cm^{-1}. It is amply evident from the Figure 3.4a that when the focus of the illumination beam is shifted up above the phantom surface (i.e. from zero offset to non-zero axial offset), the intensities of the Raman peaks ~725 and 1375 cm^{-1} (highlighted by two vertical bars of grey colour in the figure), characteristics of the sub-surface Teflon, increase and the peak at ~995 cm^{-1}, characteristic of polystyrene, decreases in intensity. The presence of the Raman peaks corresponding to the sub-surface layer of the phantom, in a RCRS spectrum measured with non-zero axial offset, and their increasing intensities with the offset shows that depth-

sensitive Raman measurements can be performed even though the illumination light is being focused above the sample surface.
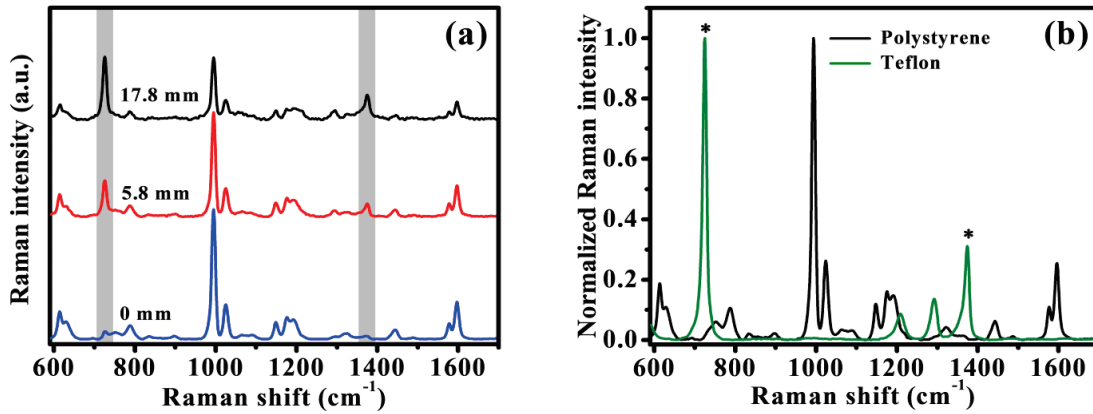
Figure 3.4: *(a) RCRS spectra of the non-biological phantom prepared with a 240 μm thick polystyrene layer. The spectra are measured at three different axial offsets. (b) Reference Raman spectra of individual layers of the phantom measured by focusing the illumination beam on their surfaces. The spectra are peak normalized.*

For a more detailed picture, the intensities of the Raman peaks at 725 and 1375 cm^{-1} corresponding to the sub-surface layer of the phantom were plotted for a set of Raman spectra measured with systematically varying the axial offset with respect to the phantom surface. Figure 3.5a shows the plots of the intensities of the Raman peaks at 725 and 1375 cm^{-1} (i.e. I_{725} and I_{1375}) as a function of the axial offset. In the figure, the zero value of the axial offset denotes the surface of the phantom. Error bars represent ±1 standard deviation over the two different measurements for a given axial offset. One can see in the figure that the peak intensities increase rapidly (almost linearly) with the axial offset. However, beyond an offset (~10 mm) the rate of increase becomes slower and approaches to nearly zero. It clearly reveals that though the probing depth in a given layered turbid sample can be increased by increasing the axial offset, it is not possible to probe deeper beyond a certain point when further increase in axial offset cannot affect any increase in the probing depth.
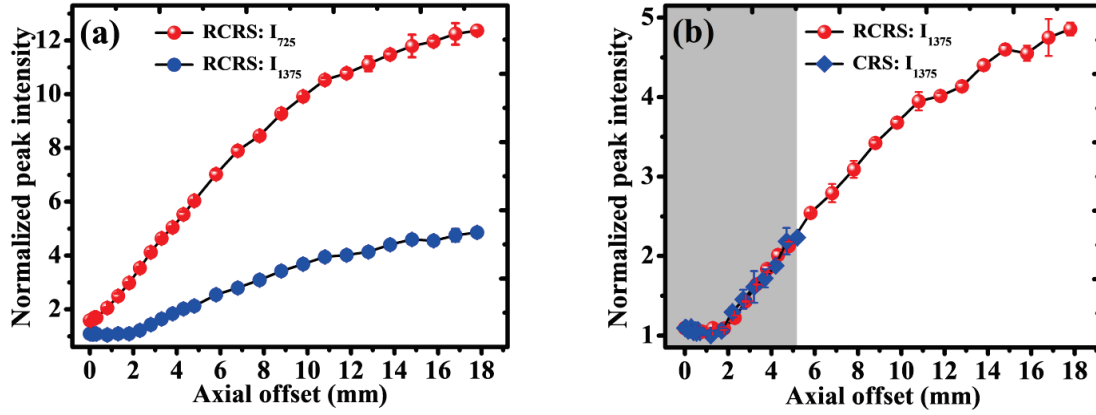
Figure 3.5: *(a) Plots of intensities of the Raman peaks at 725 and 1375 cm^{-1} in a set of RCRS spectra. (b) Plots of intensity of the 1375 cm^{-1} Raman peak in the two sets of Raman spectra acquired using the RCRS and CRS schemes of Raman detection. In both the sub-figures, error bars represent ±1 standard deviation over the two different measurements for a given axial offset.*

In order to compare the performance of the RCRS technique relative to CRS scheme of Raman detection, CRS measurements from the same phantom, by gradually focusing the illumination beam at different depths beneath the phantom surface, were also made. Figure 3.5b plots the intensities of the 1375 cm^{-1} Raman peak in the two sets of Raman spectra acquired using the RCRS and CRS schemes of Raman detection, respectively for the same set of axial offsets. It is seen in the figure that the increase in I_{1375} follows similar pattern with the intensity values almost overlapping for RCRS and CRS for all the axial offsets starting from zero to a certain limit (~5.2 mm) beyond which I_{1375} values for only RCRS exist with no I_{1375} values seen for CRS. This observation clearly reveals that both RCRS and CRS are equally adept in probing sub-surface layers of a layered turbid medium up to certain depth and beyond this depth CRS becomes ineffective (because the objective lens starts touching the sample surface), whereas RCRS, not having any such limitation, can be used to probe deeper. However, its ability of probing deeper is limited beyond a particular axial offset as noted in Figure 3.5a.

In order to improve the performance of the RCRS technique, particularly at higher offsets, we combined RCRS with the scheme of orthogonal polarized Raman detection. In the combined version, called RCPRS, the Raman spectra were measured in a similar fashion to that used earlier in RCRS, however, for each axial offset the analyzer (lying in the detection arm of the system shown in Figure 3.3) was kept in a cross-position with respect to the position of the polarizer lying in the illumination arm of the system. The RCPRS spectra measured from the same non-biological phantom (mentioned above) are displayed in Figure 3.6. In the figure, the spectrum corresponding to zero axial offset is plotted nearest to the horizontal axis and the Raman spectrum measured with the highest offset (~18 mm) is displayed farthest from the axis. It can be seen that the intensities of the two prominent Raman peaks of the sub-surface Teflon (highlighted by grey coloured vertical bars) increase with the axial offset.
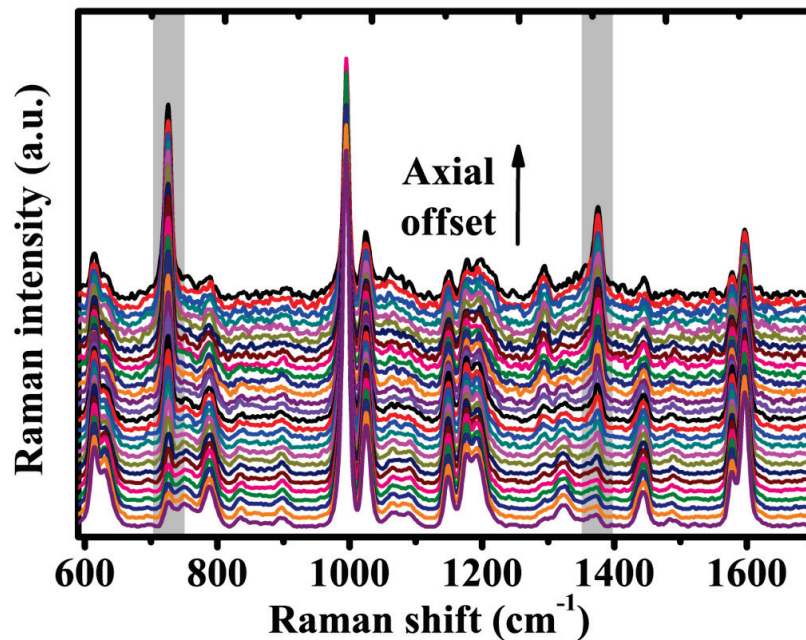
Figure 3.6: *Raman spectra of the non-biological phantom (with a 240 μm thick polystyrene) measured with RCPRS scheme. The spectra are shown at offset for clarity. The grey coloured vertical bars locate the spectral positions of the two prominent Raman peaks of the sub-surface Teflon.*

For comparing the performance of RCPRS with that of RCRS, we used the intensity of 1375 cm^{-1} Raman peak corresponding to Teflon which forms the sub-surface layer of the phantom and the ratio of the intensity of the 1375 cm^{-1} Raman peak characteristic of Teflon to the intensity of the 995 cm^{-1} Raman peak characteristic of polystyrene (I_{1375}/I_{995}). Figure 3.7a and b show the plot of the intensities of the 1375 cm^{-1} Raman peak and the values of the ratio I_{1375}/I_{995} for the same set of axial offsets used to acquire Raman spectra using RCRS and RCPRS, respectively. In both the figures, error bars represent ±1 standard deviation over the two different measurements for a given offset.
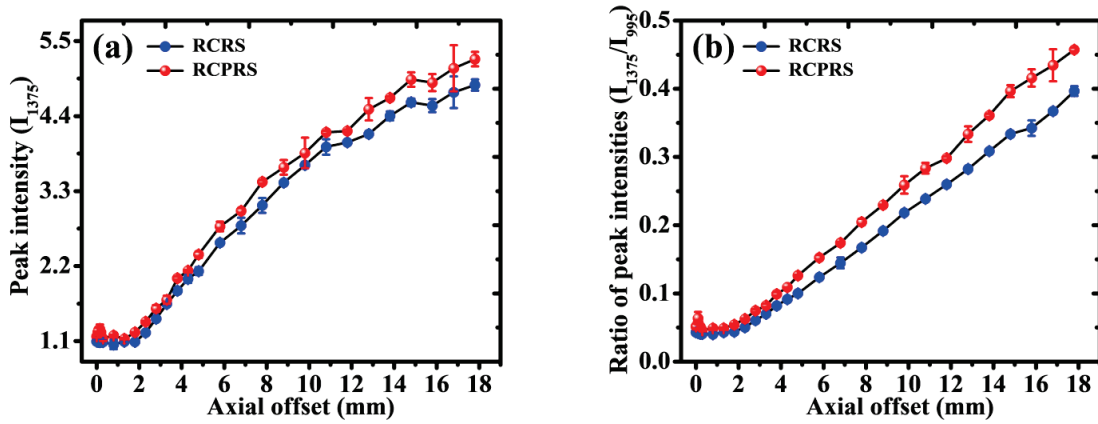
Figure 3.7: *(a) Plots of the intensity of the 1375 cm^{-1} Raman peak found in the two sets of Raman spectra acquired using the RCRS and RCPRS schemes of Raman detection respectively. (b) Plots of the ratio of the intensities of the Raman peaks at 1375 cm^{-1} and 995 cm^{-1}, I_{1375}/I_{995}, computed in the two sets of Raman spectra respectively acquired with RCRS and RCPRS. In both the sub-figures, error bars represent ±1 standard deviation over the two different measurements for a given offset.*

It is clearly seen in the figures that for each axial offset, values for both the intensity of the Raman peak at 1375 cm^{-1} (I_{1375}) and the ratio of intensities of the two peaks (I_{1375}/I_{995}) increase faster in RCPRS as compared to RCRS. The reason for such increase can be understood from the underlying principle of the RCPRS scheme, mentioned earlier in this chapter. With an increase in depth, the effect of scattering increases which changes the polarization state of the Raman signal originating from these depths. In the case of the cross-

polarized detection, the relative contribution of the sub-surface layer increases due to the substantial decrease in the Raman signal originating from the surface layer of the phantom, which is why the peak intensity (or the ratio of the peaks) increases in case of the RCPRS detection.
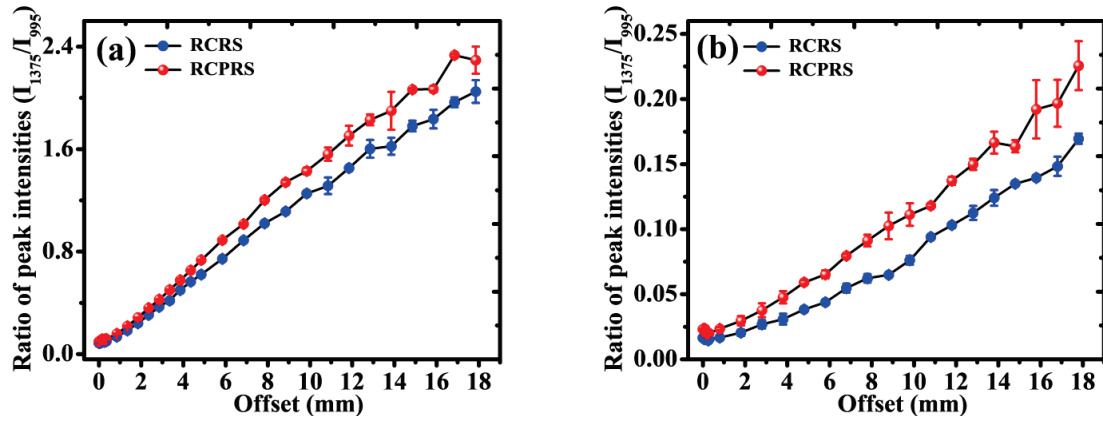
Figure 3.8: *Plots of the ratio of the intensities, I_{1375}/I_{995}, computed in the two sets of Raman spectra acquired with RCRS and RCPRS schemes of Raman detection, for surface thicknesses of (a) 80 μm and (b) 400 μm. Error bars represent ±1 standard deviation over the two different measurements for a given offset.*

In order to investigate the effect of the surface layer thickness on the ability of the RCPRS technique with respect to the RCRS, measurements were also carried out with the phantom of two different surface thicknesses, 80 μm and 400 μm respectively. Figure 3.8a and b respectively shows the plots of the ratio of the intensities, I_{1375}/I_{995}, computed in the two sets of Raman spectra acquired with RCRS and RCPRS schemes of Raman detection, for surface thicknesses of 80 μm and 400 μm. Error bars represent ±1 standard deviation over the two different measurements for a given offset. Similar to the observation noted in Figure 3.7b, here also the rate of increase is found to be higher for the RCPRS detection. A further interesting point is that the rate of the increase in the ratio of the peak intensities seems to be improving with the thickness of the surface layer of the phantom. To confirm this fact, the percentage increase (with respect to the RCRS) in the ratio corresponding to the maximum axial offset was computed for all the three thicknesses. The values of the percentage increase

are found to be ~14, 15 and 33% for the thicknesses of 80, 240 and 400 µm, respectively thereby confirming the fact that RCPRS outperforms RCRS.
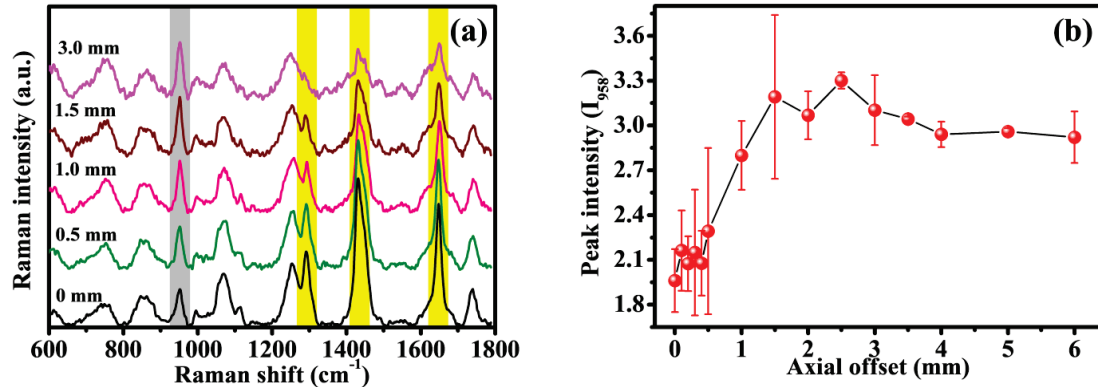
Figure 3.9: *(a) RCPRS spectra of a chicken tibia having a bone embedded in a muscle of thickness ~500 µm. The spectra are at offset for clarity. The grey coloured vertical bar highlights the Raman peak corresponding to the bone and the yellow coloured vertical bars locate the spectral positions of the Raman peaks appeared due to muscle. (b) Plot of intensity of the Raman peak at 958 cm^{-1} as a function of the axial offset. Error bars represent ±1 standard deviation over the two different measurements for a given offset.*

Following validation of the RCPRS scheme of depth-sensitive Raman detection in the non-biological phantom of varying thicknesses of its surface layer and motivated by the improved results as compared to the RCRS, the developed RCPRS system was then used for measuring the depth-sensitive Raman signatures from a two-layered biological tissue. The tissue was a chicken tibia with a bone embedded in a muscle of thickness ~500 µm. The RCPRS spectra of the chicken tibia, at five different axial offsets are displayed in Figure 3.9a. It is known that muscle being the top layer of the tissue has plenty of proteins and lipids, and shows Raman peaks at 1267, 1304 cm^{-1} (amide-III), 1443 cm^{-1} (CH$_2$ bending, lipid characteristic) and at 1660 cm^{-1} (amide-I) [2, 6-7]. On the other hand, bone, the bottom layer of the two-layered tissue is known to have Raman peaks at 958 and 1073 cm^{-1} believed to be due to phosphate (PO$_4^{3-}$) and carbonate (CO$_3^{2-}$) respectively [19, 57-58]. The presence of these Raman peaks corresponding to the two layers of the tissue can be clearly noted in the

figure. While the intensity of the Raman peak at 958 cm^{-1} (highlighted by grey coloured vertical bar in the figure), corresponding to bone, the sub-surface layer of the tissue increases with the axial offset, the intensities of the Raman peaks at ~1304, 1443 and 1660 cm^{-1} (highlighted by yellow coloured vertical bars) corresponding to the top layer of the tissue are found to decrease. In order to have a detailed picture, we plotted variation in the intensity of the peak at 958 cm^{-1} i.e. I_{958}, characteristic of the sub-surface bone, as a function of the axial offset. The plot is shown in Figure 3.9b. One may note that with the increase in the axial offset, the peak intensity increases rapidly confirming the ability of the RCPRS scheme in probing sub-surface depths. However, beyond a particular offset almost a constant value for the peak intensity is seen. This is because of the high scattering nature of the sub-surface bone. Since bone is one of the highly scattering biological samples, the light will not penetrate further inside it and thus beyond a particular offset, a constant Raman signal may be expected.

One of the important findings of the studies performed in this chapter is that the two issues (lens-sample contact and the limited probing depth) faced by a CRS based approach can be overcome by using a RCRS scheme of Raman detection. The comparison of RCRS with CRS, presented in Figure 3.5b, reveals that RCRS provides the same set of depth information which CRS achieves. However the RCRS does depth probing by focusing the illumination beam above the sample surface unlike the CRS in which depth-sensitive measurements are performed by focusing the illumination beam below the sample surface. Further, though both CRS and RCRS does equal depth-probing, the comparison could be made till a particular axial offset (~5.2 mm) due to inaccessibility of the CRS scheme. Therefore for probing higher depths (as compared to the CRS based approach) of a layered turbid medium, RCRS is explored as an effective way of gathering depth-sensitive information because of its ability of measuring Raman signals at higher axial offsets. Further,

though both CRS and RCRS fare equally in probing depth up to a particular axial offset (~5.2 mm), CRS becomes ineffective beyond this axial offset. Therefore, for probing higher depths (as compared to the CRS based approach) of a layered turbid medium, RCRS is explored as an effective way of gathering depth-sensitive information because of its ability of measuring Raman signals at higher axial offsets.

In the RCRS technique, the ability of probing deeper layers go down with the offset beyond a particular axial offset (~10 mm), as seen in the Figure 3.5a. In order to improve the performance of the RCRS technique at higher offsets (or higher depths), we recommend use of the RCPRS scheme of Raman detection. The RCPRS is a combination of RCRS and orthogonal polarized Raman detection and acquires Raman signals in a similar fashion to that used in the RCRS, however, for each axial offset the analyzer is being kept in a cross-position with respect to the position of the polarizer lying in the source arm of the system. The RCPRS measurements performed in a non-biological phantom of varying thicknesses of its surface layer show a significant increase in the sensitivity of probing sub-surface layer (beneath a turbid surface layer), as compared to the RCRS technique of depth-sensitive detection. Further, the rate of increase in the sensitivity is seen to be proportional to the axial offset thereby confirming the improvement in the RCRS measurements at higher axial offsets. Furthermore, with the thickness of the surface layer of the phantom, the rate of the improvement increases too. This was confirmed by computing the percentage increase (with respect to the RCRS) in the ratio of the intensities of the peaks corresponding to sub-surface and surface layers of the phantom, estimated at maximum axial offset. Such increase may also be seen by plotting the intensity of 1375 cm^{-1} Raman peak (corresponding to the sub-surface layer of the phantom) found with different thicknesses of the surface layer (plots are not shown), instead of the ratio of the peak intensities. However, with the surface layer thickness, the intensity profile tend to become more straight as compared to its initial profile

(of exponentially increasing nature) found with the lowest thickness of the surface layer. This is due to the fact that for low thicknesses, the light beam retains its Gaussian shape due to a limited number of scattering. With the increase in the thickness, the scattering causes light photons to be diffused. From the MC solution and the analytical solution of the well known diffusion equation for biological media [86, 90-95], it has been shown that near the boundary (or surface) emitted photon flux varies exponentially with the distance. However, away from the surface the flux varies almost linearly.
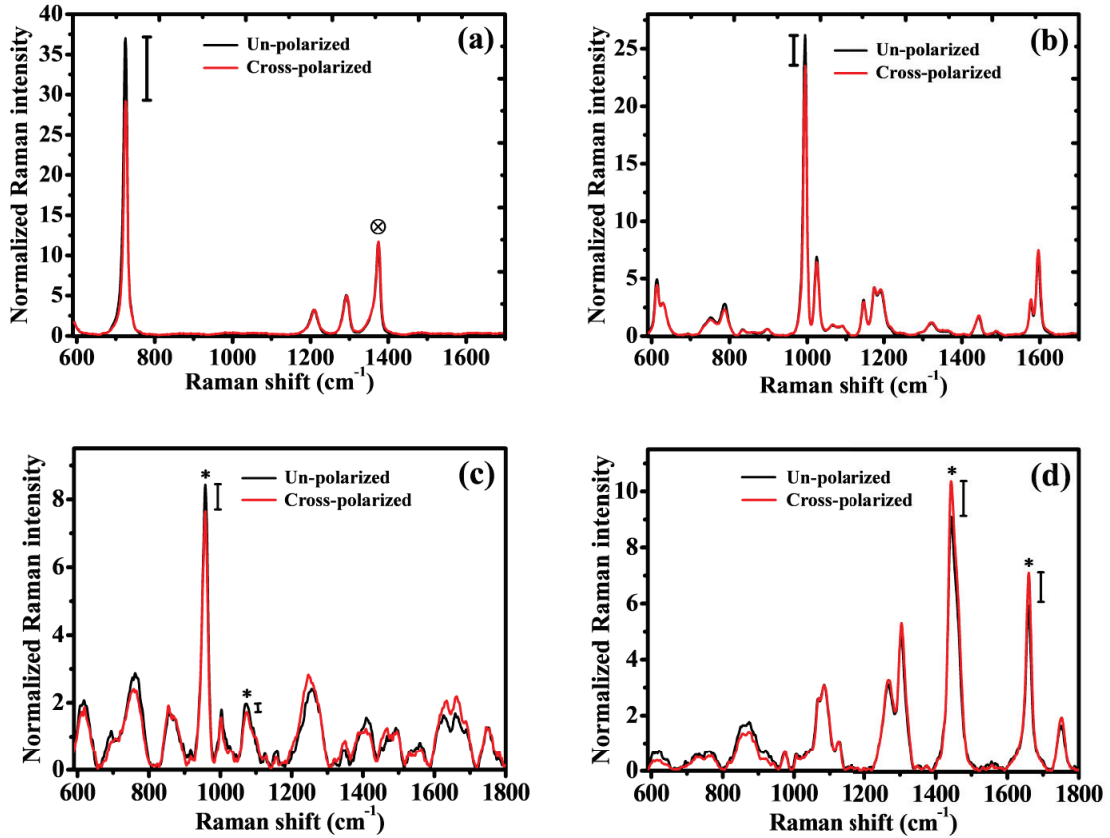
Figure 3.10: *Raman spectra of (a) Teflon, (b) polystyrene (c) bone and (d) muscle measured using an un-polarized detection and the cross-polarized detection.*

Notwithstanding the encouraging results obtained using the RCPRS technique, one drawback noted with the RCPRS scheme is that one or a few of the Raman peaks in a measured Raman spectrum may be sensitive to polarization which puts a small question mark

on the ability of the technique. In order to check this fact, we measured Raman spectra from the individual layers of the phantom and the tissue, with cross-polarized detection and without any polarizer-analyzer assembly (i.e. un-polarized detection), keeping the optical power delivered to their surfaces be same. Figures 3.10a and b show the Raman spectra of Teflon (sub-figure 3.10a) and polystyrene (subfigure 3.10b) measured with un-polarized and cross-polarized detection. For the Teflon, while the intensity of 725 cm^{-1} peak reduces by ~21% in cross-polarized detection, only 1.5% variation in the intensity of the 1375 cm^{-1} Raman peak is seen. For the peak at 995 cm^{-1}, corresponding to polystyrene (surface layer of the phantom), the decrease is noted to be ~10%. Due to the minimum variation found in the intensity of 1375 cm^{-1} Raman peak, the peak was chosen for comparing the RCPRS and RCRS schemes of detection, despite not being the most intense Raman peak of the sub-surface Teflon. Figures 3.10c and d show Raman spectra of bone (sub-figure 3.10c) and muscle (sub-figure 3.10d) measured with un-polarized and cross-polarized detection. One may note that while the intensities of the Raman peaks at 1304, 1443 and 1660 cm^{-1}, corresponding to muscle are found to increase in the cross-polarized detection, the intensity of 958 cm^{-1}, belonging to the bone, decreases with the introduction of the polarization. Despite such counter effect, an increase in the intensity of the 958 cm^{-1} peak (see Figure 3.9b) with the offset clearly reveals the potential of the RCPRS scheme of Raman detection. An additional point to be mentioned here is that although an approach closely similar to the RCRS scheme of Raman detection has been used in a few non-biomedical applications [54-56, 96-99] in the recent past, none of the studies have shown the technique's potential in biological tissues. Further, no RCPRS concept has been proposed till date for obtaining sub-surface Raman signals in an efficient way as compared to the RCRS, particularly in probing higher depths of a layered turbid medium.

3.5 Summary

To summarize, we have presented a scheme of depth-sensitive Raman measurement which overcomes the major difficulties faced by a CRS based approach. The scheme, named RCRS, uses an experimental arrangement in which depth-sensitive Raman measurements are performed by moving the focal plane of the illumination beam away from the tissue surface unlike in CRS where it is moved across the different depths of the target tissue. To enable the RCRS scheme in probing higher depths, a combination of RCRS and a scheme of plane polarized illumination and orthogonal polarized detection, abbreviated RCPRS, has also been proposed as a novel technique of depth-sensitive Raman detection. The efficacy of the proposed RCPRS technique was tested with a non-biological phantom and a biological tissue. However, in both RCRS and RCPRS schemes of Raman detection, the sample could not be illuminated effectively as it was moved continuously away from the focused illumination. Such ineffective illumination is expected to result in a poor SNR. In the next chapter, we will present development of a method which can provide a solution to this problem.

CHAPTER 4

Off-confocal Raman spectroscopy for tissue analysis

4.1 Introduction

In the previous chapter we have seen that the RCRS based approach can solve the practical problem (as was faced in CRS) of touching of the objective lens with the sample surface. By employing a combination of the RCRS and a scheme of plane polarized illumination and orthogonal polarized detection, abbreviated RCPRS, a significant enhancement in probing depth as compared to CRS was also noted. Notwithstanding the success of RCPRS, one major limitation, found with this scheme, is that the depth-sensitive Raman measurements from a tissue are performed by successively moving the focal plane of the illumination beam away from the tissue surface. Such illumination is ineffective in obtaining good quality Raman spectra, particularly, of biological tissues. For example, we found ~30% reduction in signal strength of a 20 μm thick polystyrene sheet when it was displaced by 200 μm from the focal point. It is therefore expected that an illumination fixed on the sample surface may provide a good quality Raman signal and can acquire more reliable measurement from layered biological media.

In this chapter, we report development of a depth-sensitive Raman spectroscopic system for investigating sub-surface depths in a layered turbid sample using the concept of varying Raman collection zones while keeping the point of illumination fixed on the surface of the target sample. The system makes use of a conventional confocal Raman configuration and realizes the variation in Raman collection zones employing off-confocal detection. The

technique is thus named off-confocal Raman spectroscopy (OCRS). The OCRS detection is effected by moving the tip of the Raman detection fiber (acting as the pinhole aperture) from the focus of the Raman collection objective either by taking the point of detection away from the objective (along its axis) or bringing it closer to the objective (along the same axis), thereby essentially offering two ways of enabling sub-surface interrogation at a given time. Another important attraction of the approach is that it can be used for analyzing layered turbid samples at depths beyond the reach of the conventional confocal Raman, though not at the cost of any further modifications in its instrumentation. Further, the illumination point remains fixed on the sample surface and no adjustment is required in the sample arm which indeed are significant advantages for depth-sensitive measurements *in-situ* from layered turbid samples particularly those having irregular surfaces (like biological tissues). The ability of the system to recover Raman spectra of the subsurface layer was demonstrated using a layered non-biological phantom and a biological tissue sample.

4.2 Principle of OCRS detection

The basic principle of OCRS detection can be understood from the ray diagram shown in Figure 4.1. A laser beam is focused tightly on a plane, *F1*, at a point, *a*, by using a lens (L1) of focal length f_1. This point is imaged (path shown in red colour) at point, *a'*, on plane, *P1*, through another lens, L2 of focal length f_2. In other words, the Raman signal originating from the point, *a*, will be available for the detection at the point, *a'*. The point, *a'*, is known conjugate point of the point, *a*. Since a focused Gaussian beam has certain axial spread (or Rayleigh range) over which the intensity reduces to half its maximum intensity found at the focal point (i.e. *a*), one can also expect generation of Raman signal from another point, *b*, lying on plane, *F2*. On tracing the ray diagram for this point (shown in violet colour), one

observes that the point or its corresponding Raman signal will efficiently be detected on plane, *P2* and at point, *b'*. The distance between the planes, *F1* and *F2* is taken to be *z*. Further, an axial point of a plane lying at a distance $f_1 - z$ from the lens, L1 (path is not shown in the figure), will be imaged on a plane behind the plane, *P1* at a distance, $z^* > f_2$ with z^* being the variable distance of the image planes (i.e. *P1*, *P2* etc).
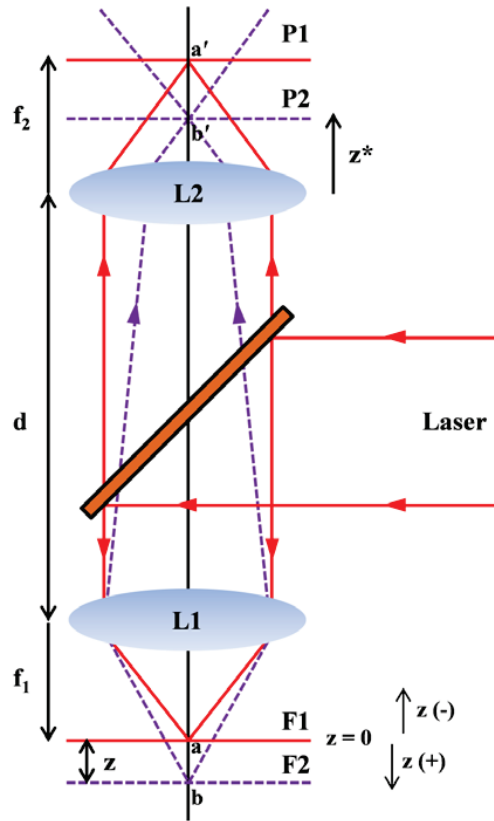
Figure 4.1: *Ray diagram to understand the principle of OCRS detection*

If the illumination point is kept fixed at the point '*a*' on the plane *F1* and the distance between the lens, L2 and the plane, *P1* (or detection fiber) is varied, Raman signal generated from different sample planes (e.g. *F1*, *F2* etc.) can be detected i.e. depth-sensitive measurements will be allowed.

In order to relate the different distances traversed in detection planes and the distances in sample planes, we developed a mathematical model based on ray transfer matrix method.

Assuming the distance between the two lenses be d, for a ray originated at a distance $f_1 \pm z$ from the lens, L1, lying on the axis of the two-lens system and crossing the axis again at a distance, the ray transfer matrices would satisfy the following equation:

$$\begin{pmatrix} 0 \\ \theta_2 \end{pmatrix} = \begin{pmatrix} 1 & z^* \\ 0 & 1 \end{pmatrix} \begin{pmatrix} 1 & 0 \\ -1/f_2 & 1 \end{pmatrix} \begin{pmatrix} 1 & d \\ 0 & 1 \end{pmatrix} \begin{pmatrix} 1 & 0 \\ -1/f_1 & 1 \end{pmatrix} \begin{pmatrix} 1 & f_1 \pm z \\ 0 & 1 \end{pmatrix} \begin{pmatrix} 0 \\ \theta_1 \end{pmatrix} \qquad \text{...... 4.1}$$

where θ_1 and θ_2 are the angles of the light ray (with respect to the optic axis of the lenses) at its starting and end point respectively. The simplification of the equation 4.1 results into following two equations:

$$(f_1 \pm z) \mp \frac{zd}{f_1} - z^* \left(\frac{(f_1 \pm z)}{f_2} \mp \frac{z(d - f_2)}{f_1 f_2} \right) = 0 \qquad \text{...... 4.2}$$

$$\frac{(f_1 \pm z)}{f_2} \mp \frac{z(d - f_2)}{f_1 f_2} = -\frac{\theta_2}{\theta_1} \qquad \text{...... 4.3}$$

Further simplification of the equation 4.2 gives -

$$z^* = \frac{f_2 \left[f_1 (f_1 \pm z) \mp zd \right]}{\left[f_1 (f_1 \pm z) \mp z(d - f_2) \right]} \qquad \text{...... 4.4}$$

The equation 4.4 provides the relation between z^* and the z. However, for employing OCRS concept one needs to know the z in terms of z^* and for that above equation can be rearranged in the following form:

$$z = \pm \frac{f_1^2 (z^* - f_2)}{d(z^* - f_2) + f_1 f_2 - z^* (f_1 + f_2)} \qquad \text{...... 4.5}$$

Since all the parameters in the right hand side of the above equation are known, the virtual distances traversed below and above the sample surface can be determined. It should be however, noted that the equation is suitable only for transparent and semi-transparent media. For highly turbid samples, the effect of scattering should also be considered.

4.3 Materials and methods

Figure 4.2 shows the experimental arrangement of the OCRS system developed for the depth-sensitive Raman measurements. The output of a diode laser (DL785-100-SO, CrystaLaser) with a central wavelength of 785 nm is first collimated by a collimating lens, CL (AC254-050-B-ML, Thorlabs Inc.) of focal length 50 mm and then spectrally purified using a laser clean-up filter, LCF (HQ782/20X, Chroma Tech. Corp.).
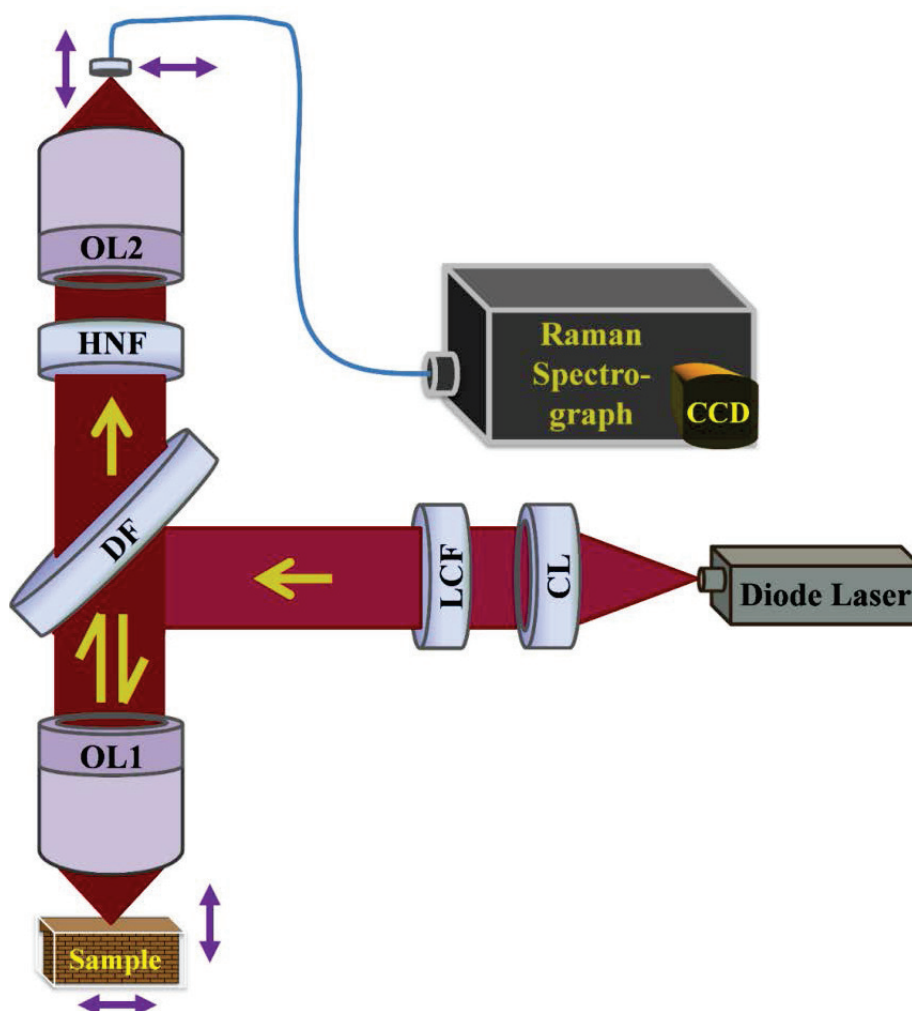
Figure 4.2: *Experimental arrangement of the OCRS technique for depth-sensitive measurements. The abbreviations and their corresponding expanded forms are as follows: CL-collimating lens, LCF-laser clean-up filter, DF-dichroic filter, OL-Objective lens, HNF-holographic notch filter.*

The spectrally purified, collimated laser beam is steered towards the sample by using a dichroic filter, DF (LPD01-785RU-25, Semrock Inc.) kept at an angle of 45° with respect to the axis of the laser beam. The dichroic filter reflects light of wavelengths <800 nm and transmits light of wavelengths >800 nm. A microscope objective lens, OL1 (20OM40, Comar Optics) focuses the incoming collimated beam onto the surface of the sample kept on a micrometer controlled x-y-z stage. The Raman signal backscattered from the sample is transmitted through the same dichroic filter, DF (that transmits light above 800 nm) and then passed through a holographic notch filter, HNF (Narrow Notch-6, Tydex J. S. Co.) before it is coupled with the help of another microscope objective lens, OL2 (10OM25, Comar Optics) into an optical fiber (of core 100 μm) mounted on a x-y-z coupler. The Raman light coming out of the distal end of the fiber is fed to an imaging spectrograph (SR-303i, Andor Shamrock) equipped with a thermoelectrically cooled, back-illuminated, deep-depletion CCD camera (DU420A-BR-DD, Andor) for depth-sensitive Raman spectral measurements.

The performance of the OCRS system was evaluated first by measuring the depth-sensitive Raman spectra from a layered non-biological phantom made of paraffin and acetaminophen and then from a biological system having a layered structure. The non-biological phantom was made by depositing a thin layer of paraffin (thickness ~300 μm) over a ~3.5 mm thick acetaminophen substrate. The tissue sample was a chicken tibia with a thin layer of muscle tissue (thickness ~400 μm) on its top. The thicknesses of the top layers of the samples were estimated using a real-time time-domain OCT system [100] developed earlier at RRCAT, Indore. The Raman spectra so measured were processed using the methodology described in the Chapter 2 and normalized with respect to their mean intensities over a spectral range of 750-1800 cm^{-1}. The optical power onto the sample surface was measured to be 60 mW.

4.4 Results and discussions

The Raman spectra were measured from the non-biological phantom, first, with the tip of the detection fiber located at the conventional confocal position (i.e. at the focus of the microscope objective OL2 in Figure 4.2) and then by moving the fiber tip away from the confocal position sequentially in two directions, one towards the microscope objective (along its axis) and the other away from the objective (along the same axis). Figure 4.3a shows the conventional Raman spectrum as well as two representative Raman spectra corresponding to two equidistant off-confocal positions (closer to and far from the objective). Each spectrum is the average of two spectra measured from two different lateral positions separated by ~1.5 mm from each other. The error bars represent ±1 standard deviation.
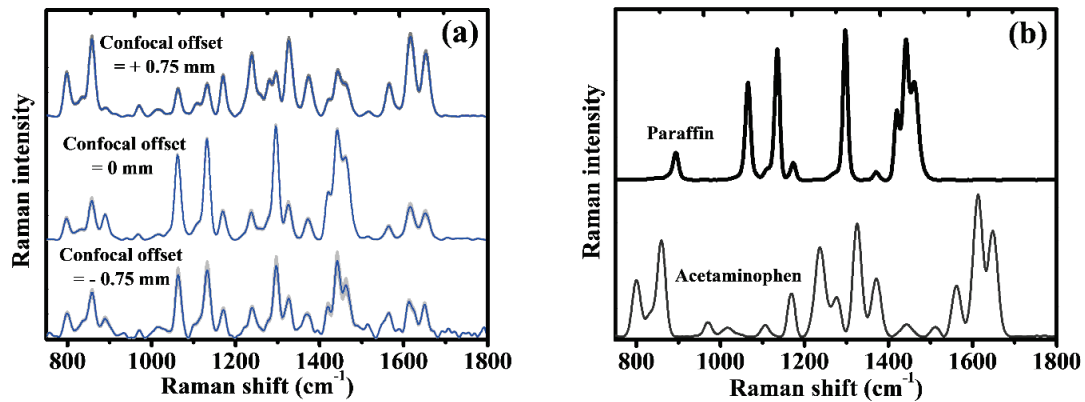
Figure 4.3: *(a) Mean normalized Raman spectra (integration time = 5s) of the non-biological phantom corresponding to two equidistant off-confocal (upper and lower row) as well as to the confocal detection positions (middle row). Each spectrum is the average of two spectra corresponding to two different lateral positions separated by ~1.5 mm from each other. The error bars in grey background represent ±1 standard deviation. (b) Normalized Raman spectra of paraffin (upper row) and acetaminophen (lower row) for reference.*

Figure 4.3b shows the Raman spectra of the authentic samples of paraffin and acetaminophen measured with the same experimental set-up with the fiber tip located at the confocal position. One can see from the Figure 4.3a that the Raman spectrum corresponding

to the confocal position of the fiber tip is dominated by the Raman bands associated with the top paraffin layer. This is quite expected because the excitation as well as the collection in this case is done through the same cone whose apex is the focal spot that lies on the surface of the sample. However, for both the off-confocal spectra (measured by displacing the fiber tip equidistant from the confocal position in two opposite directions along the axis of the microscope objective), the intensities of the Raman bands (e.g. ~855, 1328 cm^{-1} and the triplet peaks between ~1550 to 1650 cm^{-1}) of the bottom acetaminophen layer is seen to increase relative to the intensities of the Raman bands (e.g. ~1295 and 1440 cm^{-1}) of the top paraffin layer. Further, the Raman spectrum measured with the detection fiber away from the microscope objective is seen to contain considerably higher contribution of Raman characteristics of acetaminophen as compared to the spectrum measured with the detection fiber at the position closer to the objective. This becomes further evident from the computed ratio of the intensity of the characteristic Raman peak of acetaminophen (at 855 cm^{-1}) to that of the characteristic peak of paraffin (1440 cm^{-1}). The ratio (I_{855}/I_{1440}), a quantitative measure of the relative contribution of acetaminophen vs. paraffin, was found to be significantly higher ($I_{855}/I_{1440} = 1.66$) for the Raman spectrum measured away from the objective as compared to the corresponding ratio value ($I_{855}/I_{1440} = 0.6$) calculated for the spectrum measured closer to the objective.

In order to have a more detailed picture, the ratios of the intensities of the Raman peaks at 855 cm^{-1} and 1440 cm^{-1} (i.e. I_{855}/I_{1440}) were computed in a set of Raman spectra measured with systematically varying the displacement of the tip of the detection fiber with respect to its confocal detection position in steps of 100 μm both away from and nearer to the microscope objective. Figure 4.4a shows plot of the ratio of the intensities I_{855}/I_{1440} as a function of the confocal-offsets investigated. Figure 4.4b shows the variation in intensities of the individual Raman peaks (i.e. I_{855} and I_{1440}) corresponding to subsurface layer of

acetaminophen and the surface layer of paraffin. Error bars represent ±1 standard deviation over spectra measured from two different lateral positions.
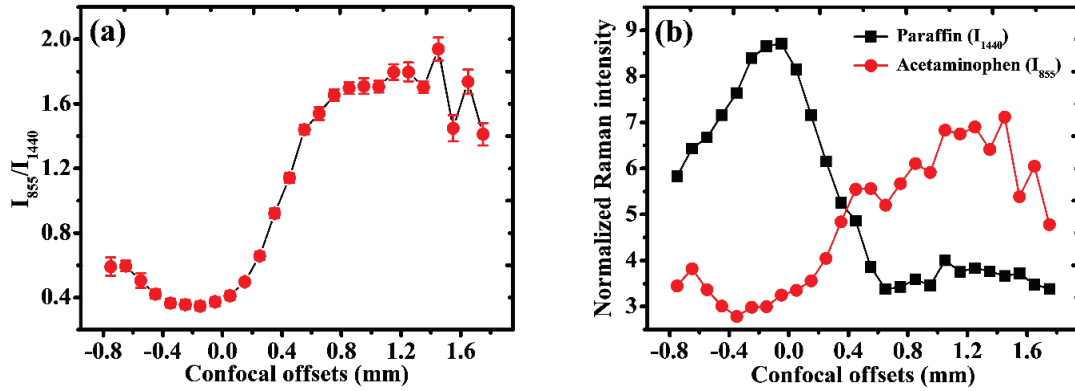
Figure 4.4: *(a) The ratio of intensities of Raman bands corresponding to 855 cm^{-1} and 1440 cm^{-1} as a function of the confocal-offsets investigated in steps of 100 µm. Error bars represent ±1 standard deviation. (b) The variation in intensities of the individual Raman peaks (i.e. I_{855} and I_{1440}) as a function of the confocal-offsets.*

A perusal of the figure reveals a few interesting points worth noting. For example, while the values of I_{855} as well as of I_{855}/I_{1440} are the lowest around the confocal position indicating dominant paraffin Raman signatures from the surface of the sample, these values increase when one is displaced away from the zero offset position in either direction signifying increase in the Raman signatures from the subsurface acetaminophen. However, it is interesting to see that the rate of increase is significantly more when the point of detection is moved away from the objective (i.e. when the confocal-offsets are positive) as compared to when it is moved in the opposite direction nearer to the objective (confocal-offsets negative). Further, it is seen that beyond a point (confocal-offset ~0.7 mm) the ratio values do not change with further increase in the values of the confocal-offset. However, the maximum ratio value corresponding to the positive confocal-offset is found to be considerably larger (almost three times) than that corresponding to the negative confocal-offset implying that the Raman spectra measured with positive confocal-offset contain significantly more subsurface Raman signatures as compared to the spectra measured with negative offset.

The above observations pose two immediate questions. First, how a confocal-offset effected by moving the detection point away from the confocal position in either direction (away from the objective or nearer to it) allows one to detect the subsurface Raman signal, and second, why the spectra corresponding to the positive confocal-offsets contain significantly enhanced Raman signatures of the subsurface layer compared to the spectra corresponding to the negative offsets of equal magnitude.
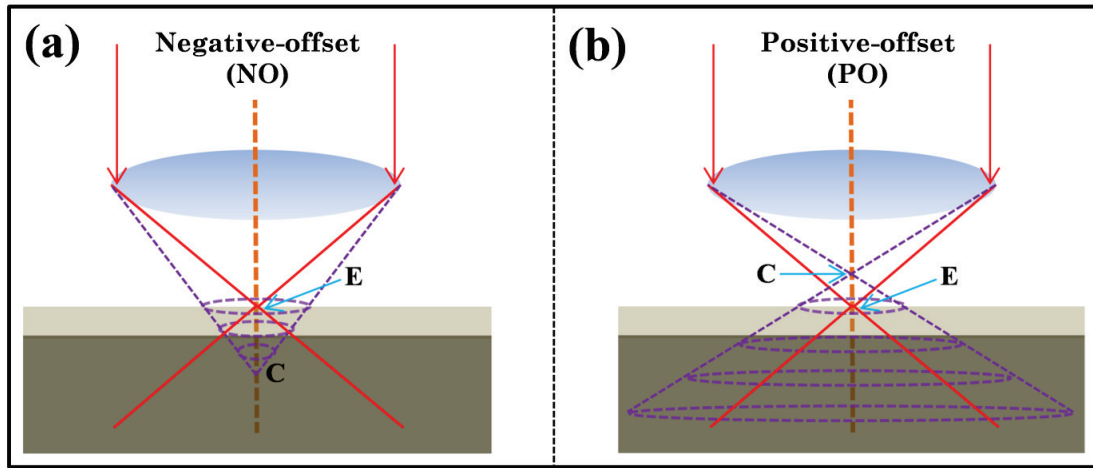
Figure 4.5: *Pictorial demonstration of the principle of OCRS for sub-surface interrogation. (a) Ray diagrams showing illumination-collection configurations at the surface of the sample for negative confocal offset, (b) ray diagrams showing illumination-collection configurations on the sample surface for positive confocal offset.*

The ray-diagrams, illustrated in Figures 4.5a and b, may help understand the underlying reasons. Let us assume that the rays of illumination are focused at a point E on the surface of a two layered sample. Let C be the point of collection which is conjugate to the point of detection (lying near the objective OL2 of Figure 4.2 and not shown in the present figures). Let us consider the situation wherein one gets the maximum possible Raman signatures from the subsurface layer. It is evident that for the negative confocal-offset i.e. when the point of detection is nearer to the objective, the collection point C will lie inside the sample below the sample surface (as shown in Figure 4.5a). Similarly, for the positive offset i.e. when the point of detection is away from the objective, the collection point C will lie

above the sample surface (as shown in Figure 4.5b). One can see that in the both the cases, the illumination-collection configuration at the surface of the sample is identical to that of a conventional SORS [17]. For example, in the present case, it is seen that the point of illumination is fixed on the sample surface at E and the Raman photons exiting the surrounding circular region through all the points lying symmetrically around this illumination point with distances of separation varying between zero (zero spatial offset) and the radius of the circle are collected for detection. Thus the off-confocal separation of the detection point leads to the classical SORS spatial offset [17, 54-56] at the sample surface which is why it has been possible to probe subsurface depths with off-confocal detection.

Though the exact reason behind the enhanced sub-surface Raman signal with a positive confocal-offset is not clearly understood at this moment, for a plausible explanation one may envisage the illumination and collection scenario below the sample surface in Figures 4.5a and b. It is pertinent to mention here that a ray diagram is not strictly valid for describing the excitation light and the collection of scattered Raman signal below the sample surface in the present case because unlike transparent /semi-transparent medium, both the excitation light and the emitted Raman signal will propagate in curved zigzag path inside this turbid and multiply scattering sample. Though multiple scattering eventually will lead to scrambling of the directional information on photon propagation, it is expected to take several transport path lengths for complete randomization of the propagation direction of the incident directional light beam [101]. In fact, within this path length (where all the photons haven't completely lost its directional memory), one may still use average photon trajectories to describe light propagation. Unlike transparent /semi-transparent medium (where photon trajectories are described by straight line), such average photon trajectories would be curved and determination of its exact nature would involve modeling of light propagation using MC simulations [91] or radiative transport theory (or its simpler variant using diffusion

approximation) [101]. Thus, though a ray diagram is not valid for describing photon trajectories beneath the sample surface in the present case, nonetheless, an analogous diagram with curved photon path (describing the average photon trajectories) may still be adopted to describe excitation/collection of Raman signal inside the sample. With this picture of average curved photon trajectories (beneath the sample surface) in mind, one can now envisage the differences in the changes in the effective volume of the Raman collection zone (inside the sample) with increasing subsurface depths corresponding to the positive and the negative confocal-offsets, even though, for both the offsets the illumination volume below the sample surface is expected to remain unchanged across the depths (since the point of illumination is fixed on the sample surface at the point E). By comparing the envisaged volume of the Raman collection zones at a particular sub-surface depth for the two offsets, one can understand that the collection volume will be significantly enlarged for the positive offset as compared to that for the negative offset indicating considerably larger number of diffused Raman photons (and hence larger Raman response) corresponding to the positive offset.

In order to retrieve the characteristic Raman spectra of the two layers, all the spectra were subjected to the method of scaled subtraction described in the Chapter 2. This was done by taking, at a time, two Raman spectra, one measured with the tip of the detection fiber located at the conventional confocal position, being at the focus of the Raman collection objective (so as to get a sharp image of the sample surface), and the second measured with the fiber tip displaced away from the focus of the objective in either direction (leading to a defocusing of the Raman collection zone on the sample surface). The first spectrum, dominated by the characteristic Raman signatures of the top layer, is then scaled subtracted from the second spectrum (obtained at off-confocal position) to recover the Raman spectrum characteristic of the subsurface bottom layer by cancelling out the spectral contributions of the surface layer contained in it. The recovery of the Raman spectrum characteristic of the top

layer is obtained in analogy by a reverse process in which the Raman spectrum recorded at the off-confocal position is scaled subtracted from the spectrum measured with the fiber tip at the confocal position.
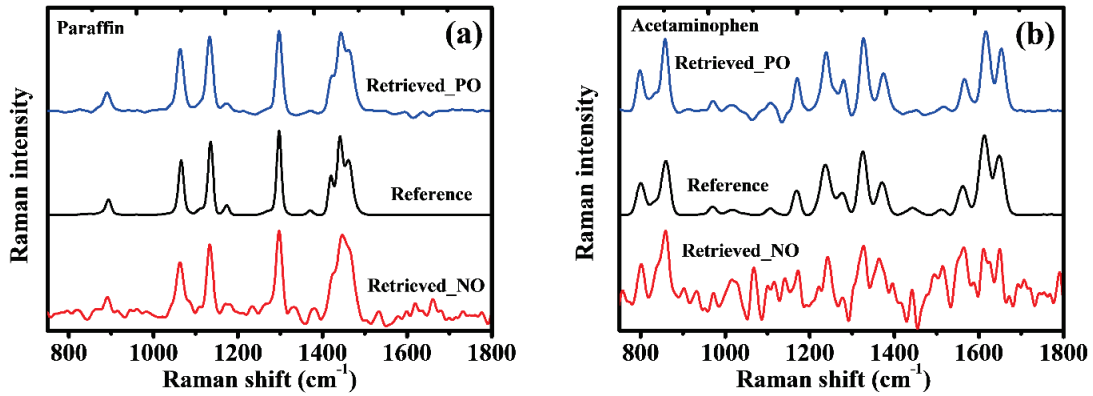
Figure 4.6: *(a) Raman spectra of the surface paraffin layer retrieved through scale subtraction using off-confocal spectrum with positive (upper row) and that with negative confocal offset (bottom row) along-with the reference Raman spectrum of authentic paraffin (middle row). (b) Raman spectrum of sub-surface acetaminophen layer retrieved through scale subtraction using off-confocal spectrum with positive confocal offset (upper row) and that with negative confocal offset (bottom row) along-with the reference Raman spectrum of authentic acetaminophen (middle row).*

Figure 4.6a shows the Raman spectra of the surface paraffin layer retrieved through scale subtraction using the off-confocal spectra with positive and negative confocal offsets. Similarly, Figure 4.6b displays the Raman spectra of the sub-surface acetaminophen layer retrieved through scale subtraction using the off-confocal spectra with positive and negative confocal offsets. For the purpose of comparison, the spectra of the authentic paraffin and acetaminophen are also shown as reference in the respective figures. One can see from the figures that all the relevant Raman bands observed in the scaled-subtracted spectra have a very good match ($R^2 = \sim 0.9$) with those found in the reference Raman spectra of the authentic paraffin and acetaminophen constituting the layers. For further confirmation, the ratios of intensities of the characteristic Raman peaks of paraffin at 1295 cm^{-1} and 1440 cm^{-1} (i.e.

I_{1295}/I_{1440}) and of acetaminophen at 855 cm^{-1} and 1612 cm^{-1} (i.e. I_{855}/I_{1612}) were calculated for the set of scaled subtracted Raman spectra corresponding to the positive and negative confocal offsets. The ratio values turned out to be 1.04 and 0.89 for the spectra of the surface (zero confocal offset) and subsurface (positive confocal offset) layers retrieved through scaled-subtraction using off-confocal spectrum corresponding to positive confocal offset and were found to be reasonably close the corresponding ratio of intensities (1.06 and 0.70 respectively) calculated for the reference Raman spectra of authentic paraffin and acetaminophen, respectively. However, using the off-confocal spectrum with negative confocal offset for scaled-subtraction while the value of the ratio I_{1295}/I_{1440} was found to be 1.03 for the retrieved spectrum of the surface layer of paraffin as against the value of 1.06 for the authentic paraffin, the value of the ratio I_{855}/I_{1612} turned out to be 1.3 for the retrieved spectrum (negative confocal offset) of the subsurface layer of acetaminophen as against 0.70 for the authentic acetaminophen corroborating that the off-confocal Raman spectrum with negative confocal offset contain less sub-surface specific Raman signatures as compared to the corresponding spectrum measured with positive confocal offset.

Following validation in the non-biological phantom, the system was used to measure Raman spectra from the biological tissue in a similar manner as before, first, with the point of detection located at the conventional confocal position, and then by moving it in steps of 100 μm away from the confocal position sequentially in two directions, one towards the collection objective and the other away from it. Figure 4.7a shows the measured Raman spectra of the tissue sample corresponding to three different confocal-offsets, zero (detection point at the focus of the objective), positive (detection point far from the objective) and negative (detection point closer to the objective) with error bars representing ±1 standard deviation. Similar to the earlier case, here also, each spectrum is the average of two spectra corresponding to two different lateral positions separated by ~1 mm.
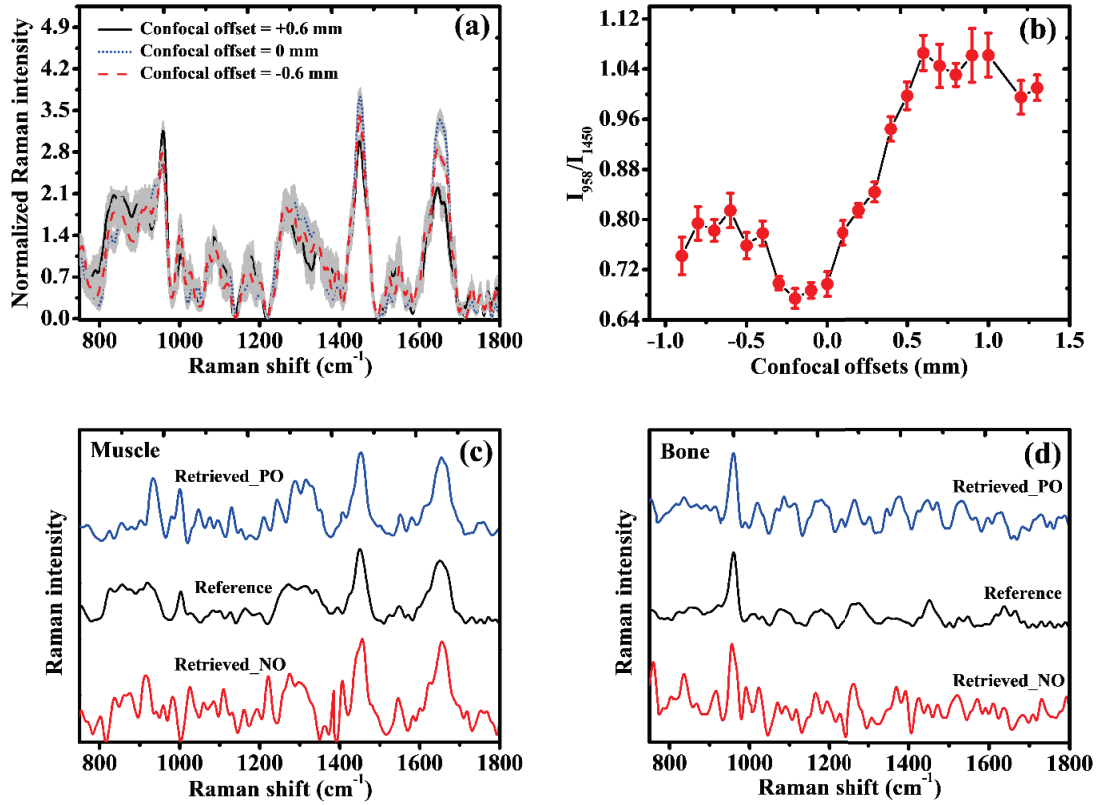
Figure 4.7: *(a) Mean normalized Raman spectra corresponding to two equidistant off-confocal detection positions as well as to the confocal detection position. The error bars represent ±1 standard deviation. (b) The ratio of the intensities of the Raman bands corresponding to 950 cm^{-1} and 1450 cm^{-1} as a function of the confocal-offsets investigated in steps of 100 μm. Error bars represent ±1 standard deviation. (c) Raman spectra of the surface muscle layer retrieved through scale subtraction using off-confocal spectrum with positive (upper row) and that with negative confocal offset (bottom row) along-with the reference Raman spectrum of the native muscle tissue (middle row). (d) Raman spectrum of sub-surface bone retrieved through scale subtraction using off-confocal spectrum with positive confocal offset (upper row) and that with negative confocal offset (bottom row) along-with the reference Raman spectrum of native bone (middle row).*

As expected in both the Raman spectra measured at off-confocal positions the Raman signatures of subsurface bone dominates over that of the surface layer of muscle tissue. For example, the intensities of the characteristic muscle tissue Raman bands at ~1650 cm^{-1} (amide-I) and 1450 cm^{-1} (CH$_2$ bending) are found to decrease and the intensity of the characteristic bone Raman band at ~958 cm^{-1} (believed to be due to Phosphate in bone) is

seen to increase. Figure 4.7b shows the plot of the ratios of the normalized intensities of the Raman peaks at 958 cm^{-1} and 1450 cm^{-1} (i.e. I_{958}/I_{1450}) as a function of the different confocal-offsets. Error bars represent ±1 standard deviation over spectra measured at two lateral positions. One can clearly see that like in the case of non-biological phantom as one moves from the confocal position (i.e. zero confocal-offset) in either direction, the values start increasing indicating lesser contribution of the Raman signal from the surface layer which indeed is the case. Figures 4.7c-d show the scaled-subtracted tissue Raman spectra corresponding to the spectra shown in Figure 4.7a. On comparing the retrieved spectra with the reference spectra (shown in the same figures), measured separately from the corresponding native tissues constituting the layers, it is evident that there is reasonably good match between the Raman bands of the retrieved spectra with those found in the reference spectra of the native tissues. However, one can clearly see that the pair of spectra (corresponding to off-confocal and confocal detection) recovered through scaled-subtraction using the off-confocal spectrum measured with positive confocal-offset have a better match ($R^2 = \sim0.65$) with the reference Raman spectra as compared to the corresponding pair of tissue Raman spectra retrieved using the off-confocal spectrum measured with negative confocal-offset ($R^2 = \sim0.4$). The spectrum measured with zero-confocal offset was the common second spectrum used during scaled-subtraction along with either of the off-confocal spectra (corresponding to positive and negative confocal offsets). Further, the ratios of the intensities of the Raman peak at 1078 and 958 cm^{-1} in the retrieved off-confocal spectra (i.e. of the subsurface bone tissue layer) corresponding to positive and negative confocal offsets were 0.35 and 1.2 as against the value of 0.25 found for the reference Raman spectrum of native bone confirming once again that the Raman spectra measured with positive confocal-offsets have the ability to probe subsurface layers more efficiently as compared to the spectra measured with negative offsets.
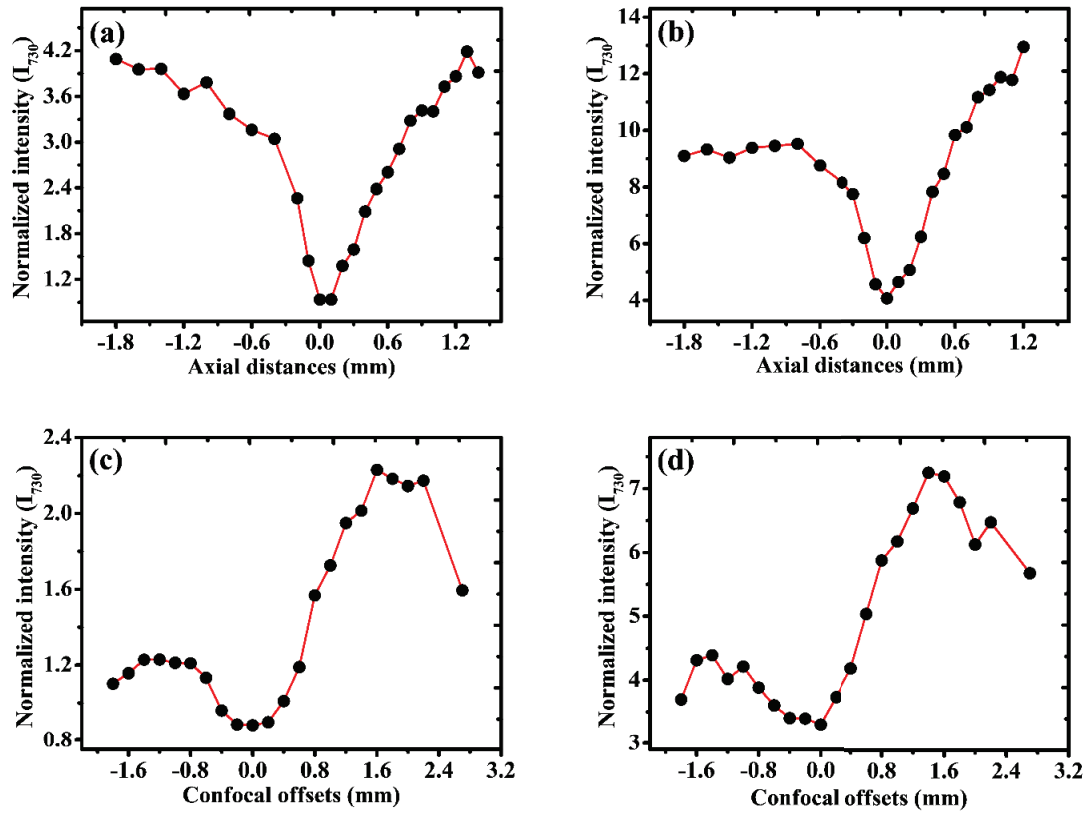
Figure 4.8: *The plots of variation in the normalized Raman intensity at 730 cm^{-1} (characteristic of subsurface Teflon) as a function of positive / negative displacements with respect to the confocal position in μ-SORS: (a) for the sample with 800 μm thick paraffin layer overlaying a 15 mm thick Teflon, and (b) for the sample with ~250 μm thick tissue layer overlaying a 15 mm thick Teflon. The plots of variation in the normalized Raman intensity at 730 cm^{-1} as a function of positive / negative confocal offsets in OCRS: (c) for the sample with ~800 μm thick paraffin layer overlaying a 15 mm thick Teflon, and (d) for the sample with ~250 μm thick tissue layer overlaying a 15 mm thick Teflon.*

In order to compare this interesting property of OCRS of using two sided-sided SORS effect in probing sub-surface depths with that of the conventional μ-SORS [54-56, 102] (a technique similar to the RCRS demonstrated in Chapter 3), two mock-up samples were prepared. In one, a layer of paraffin of ~800 μm thicknesses was deposited on a 15 mm thick Teflon substrate and in the second, a section of chicken muscle tissue of thickness ~250 μm was overlaid on a similar Teflon substrate of 15 mm thickness. Figures 4.8a and b plot the

variation in intensities of the characteristic (prominent) Raman peak of the subsurface layer (i.e. Teflon) as a function of positive / negative displacements (with respect to the confocal position) introduced using the μ-SORS. Figures 4.8c and d show the corresponding variation in the intensities of the Raman peak of the sub-surface layer as a function of the positive / negative confocal offsets introduced using OCRS. One can see that in the case of μ-SORS while the peak intensities vary almost symmetrically around the confocal position for the sample with paraffin as the top layer (Figure 4.8a) indicating almost equal contribution of subsurface Raman signal (from Teflon) for both the positive and negative displacements, the corresponding intensity variation becomes asymmetric with significantly diminished contribution of the sub-surface Raman (from Teflon) for negative displacements (i.e. when the imaged zone is above the sample surface) for the sample with tissue as the top layer (Figure 4.8b).

In contrast, in the case of OCRS, the variation of the peak intensity around the confocal detection is seen to be asymmetric for both the samples (Figures 4.8c and d) with considerably more contribution of subsurface Raman for the positive offsets in comparison with the negative offsets of equal magnitude. In order to first understand the difference in the nature of variation of the subsurface Raman response (i.e. symmetric versus asymmetric) for the two samples investigated using μ-SORS, the transport path lengths of photons in the top layer materials used in the respective samples were estimated. It was found that while for paraffin (used to prepare the sample) the estimated transport path length was ~280 μm, for the chicken muscle tissue it was ~1.8 mm. Now, since the thickness of paraffin used as the top layer in the first sample was ~800 μm, it was definitely turbid on the scale of its thickness (since thickness of paraffin layer > the transport path length of paraffin). On the other hand, the second sample with the 250 μm thick section of tissue at the top turned out to be semi-transparent (since tissue thickness < the transport path length of tissue) on the scale of the

thickness of tissue. Since a sample with a turbid surface layer is known to produce symmetric variation in Raman response of the subsurface layer whereas that with a semi-transparent or transparent surface layer produces asymmetric variation with the μ-SORS [102], the reason for the contrasting observations for the two samples used in the present experiment became apparent. The observed dissimilarity in the outcome of the experiments carried out using μ-SORS and OCRS can be understood considering the mechanisms underlying the two techniques. For example, in the case of μ-SORS, both the illumination and collection zones remain (almost) completely overlapped whether one goes above or below the sample surface. As a result, both the positive and negative displacements (around the confocal) lead to similar degree of laser illumination and Raman collection zone enlargement on and beneath the sample surface thereby producing very similar Raman response from the sub-surface layer of a sample with a turbid surface layer. In contrast, in OCRS, the illumination being fixed on the sample surface, the confocal offsets introduce enlarging collection zones to generate the SORS photons. Since the positive and negative confocal offsets lead to different degrees of Raman collection zone enlargement beneath the sample surface (as already explained earlier), the distribution of the sub-surface Raman response around the confocal is always asymmetric irrespective of whether the sample is turbid or semi-transparent (or transparent).

The results of the studies described above demonstrate the potential of OCRS as a viable technique for carrying out depth-sensitive Raman spectroscopy in a layered turbid sample. An important attraction of the system is that it allows probing subsurface depths in two ways, either by moving the fiber tip closer to the Raman collection objective (in the detection arm) but away from the confocal position, or by moving the fiber tip away from the objective but also away from the confocal position, thereby providing two sided SORS effect. Another point of attraction of OCRS is the simplicity with which the system can be used for analyzing turbid layered samples at depths beyond the reach of the conventional confocal

Raman without requiring any further modifications in the conventional confocal Raman instrumentation. Further, unlike the earlier reported systems, no adjustment is required in the sample arm as the illumination area is fixed on the sample surface, which is a significant advantage for non-contact, depth-sensitive measurement from a layered sample (like biological tissue) which most of the time has an irregular surface. In OCRS, on the other hand, subsurface depths can be probed by simply varying the separation between the fiber tip and the microscope objective at the detection end (see Figure 4.2). Since these are independent of the sample arm, it amounts to having a remote handle in varying the probing depths inside a sample without requiring any manipulation inside the sample arm.

4.5 Summary

In this chapter, we have shown development of a novel depth-sensitive Raman spectroscopic system using the principle of defocusing the Raman collection zone while keeping the point of illumination fixed on the surface of a target sample. The system adopts the configuration of a confocal Raman and employs off-confocal detection for non-destructive sub-surface interrogation of layered turbid samples at depths beyond the reach of the conventional confocal Raman owing to a high level of diffuse scattering. The concept was demonstrated using two examples, one in which the system was used on a non-biological phantom to recover subsurface acetaminophen Raman through a thin layer of paraffin deposit on its top, and second, in which it was used to extract Raman signal characteristic of bone through a thin layer of muscle tissue lying atop it. Apart from the ability of the approach in probing sub-surface depths in a highly scattering sample, its other important attraction is that it does not require any adjustment in the sample arm of the system and the illumination light remains fixed onto the surface of the sample under investigation. It is a significant advantage for

depth-sensitive measurement from a layered sample having an irregular surface (like biological tissues). Although the proposed technique is novel and can be converted into a portable system for acquiring depth-sensitive Raman signal *in-situ* from a variety of layered turbid samples including the biological tissues at depths outside the scope of confocal like detections, development of a technique capable of measuring Raman signatures beyond a thickness ~800 μm is often required in many biological applications like non-invasive probing of bone (through a 2-3 mm thick muscle) etc. In the next chapter, a depth-sensitive spectroscopic technique capable of probing higher depths will be presented.

CHAPTER 5

Cone-shell Raman spectroscopy for tissue analysis

5.1 Introduction

In the previous chapters, we described the use of existing depth-sensitive technique like CRS in tissue diagnosis and development of two novel depth-sensitive Raman techniques (RCPRS and OCRS) for analysis of layered biological tissues. It has been found that RCPRS overcomes the practical limitations of CRS and can probe deeper. Although the OCRS approach was found to solve the practical limitations of both CRS and RCPRS in probing sub-surface layers, yet the depths beyond ~800 μm could not be probed using it. Development of a technique capable of measuring Raman signatures beyond a thickness ~800 μm is often required in many biological applications like non-invasive probing of bone through a thick (~2-3 mm) muscle.

In this chapter, we report development of a novel scheme of depth-sensitive Raman spectroscopic measurement for probing depths beyond 800 μm. The scheme uses three identical axicons for Raman excitation of the target sample in form of a hollow conic section. The Raman scattered light from the sample, passed through the same (but solid) conic section, is collected for detection. Because of using the configuration of cone-shell excitation and cone detection, the scheme is named cone-shell Raman spectroscopy (CSRS). Evaluation of the performance of the developed scheme on non-biological phantom and biological tissue sample demonstrated its ability to recover Raman spectra of layers located at depths of ~2-3 mm beneath the surface. Apart from its ability of probing larger depths, an important

attraction of the system is that the probing depths can be varied by simply varying the separation between axicons in the excitation arm. Further, no adjustment is required in the sample arm, which is a significant advantage for non-contact, depth-sensitive measurement.

5.2 Principle of CSRS detection

Figure 5.1 shows the principle of CSRS detection. In this scheme of Raman detection, three axicon lenses A, B and C are used. The lens, A, converts a collimated beam into a ring shaped (or hollow) beam which is first focused and then gets to diverge. The lens, B, collimates the hollow diverging beam. Finally, the lens, C focuses the collimated beam on layer 1 of the sample.
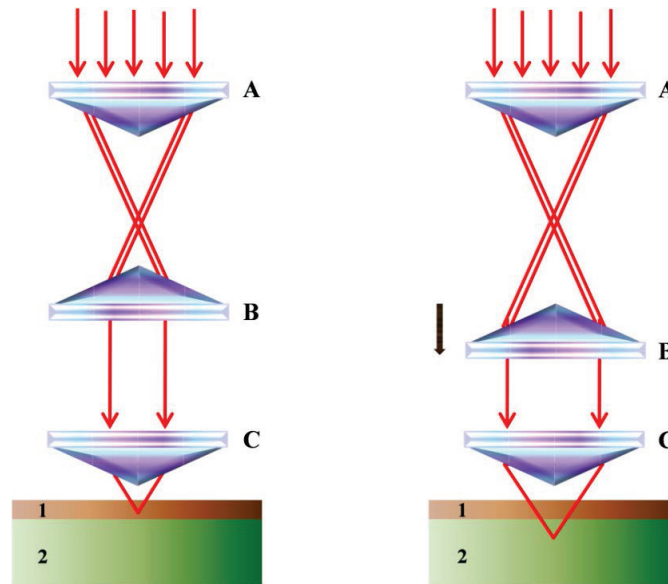
Figure 5.1: *Geometrical sketch showing the CSRS principle*

On displacing the lens, B away from the lens, A, along their common axis, the output through B will be again a collimated beam, however, of increased diameter. Due to the increased diameter, the points of incidence on the surface of the lens, C, are shifted away as

compared to those seen in the former case. Unlike a simple lens, the other surface (i.e. exiting) of the axicon, C, has no curvature, instead has a slanted surface. As a result, the beam is focused at a larger depth inside the sample. Since the beam is focused at two different depths by changing the position of the lens, B, the Raman scattered light from these two focal points will have different proportion of the Raman signatures corresponding the two layers.

5.3 Materials and methods

Figure 5.2 shows the experimental arrangement of the developed CSRS setup. It uses a 785 nm multimode diode laser (CL-2000, CrystaLaser) for Raman excitation. The laser beam is spectrally purified using a laser clean-up filter (HQ782/20X, Chroma Tech. Corp.) and then collimated using an objective lens (10OM25, Comar Optics). The collimated laser beam is then passed through an axicon lens, AX1 (1-APX-2-C254, Altechna Co. Ltd.) which converts it into a ring shaped beam with increasing diameter along its axis. Another identical axicon, AX2 placed coaxial with AX1 is used to collimate the diverging ring shaped beam. The diameter of the ring can be varied by varying the spatial separation between the two axicons. A dichroic filter (LPD01-785RU-25, Semrock Inc.) kept at an angle of 45° with respect to the axis of the axicons is used to steer the ring-shaped collimated beam towards the sample onto which it is focused using a achromat lens (AC254-050-B-ML, Thorlabs Inc.) and axicon lens (identical to AX1 and AX2) combination. The Raman signal backscattered from the sample is transmitted through the same dichroic filter (that transmits light above 800 nm) and then passed through a notch filter (Narrow Notch-6, Tydex J. S. Co.) before it is coupled to an optical fiber of core 100 μm with the help of a fiber collimating lens (F810SMA-780, Thorlabs Inc.) of numerical aperture (NA) 0.25. The light coming out of the distal end of the fiber is fed to an imaging spectrograph (SR-303i, Andor Shamrock) equipped with a

thermoelectrically cooled, back-illuminated, deep-depletion CCD camera (DU420A-BR-DD, Andor) for depth-sensitive Raman spectral measurements.
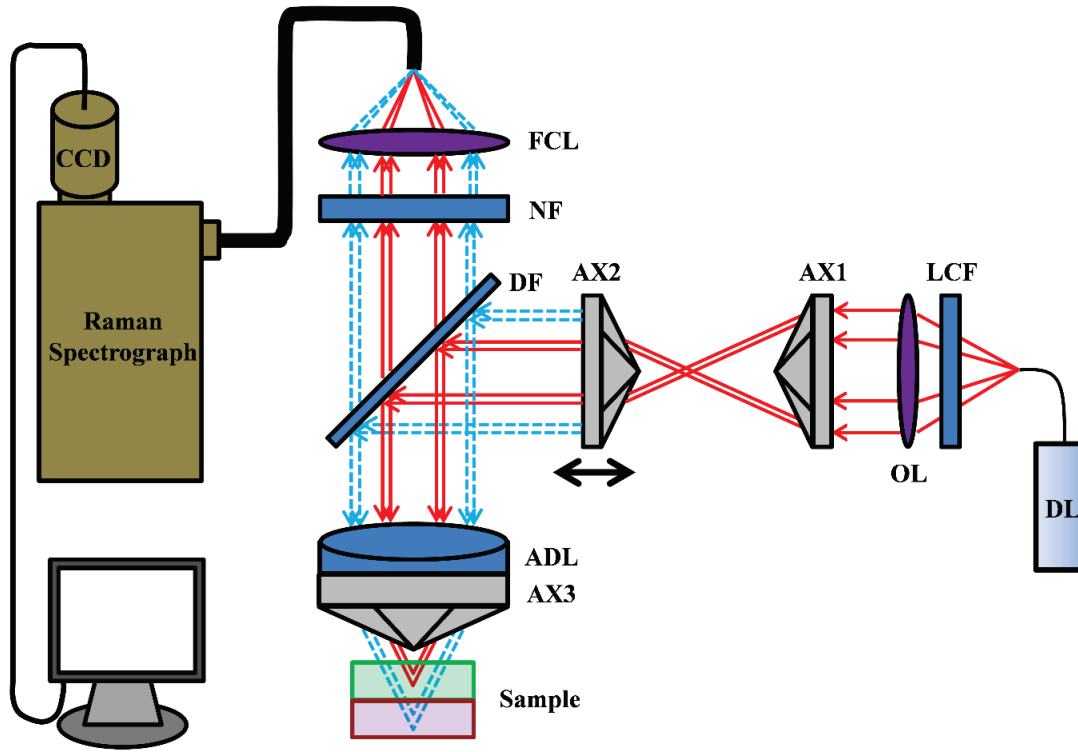
Figure 5.2: *Experimental setup for the depth-sensitive CSRS system. The abbreviations and their corresponding expanded forms are as follows: DL-Diode laser, LCF-Laser clean-up filter, OL-Objective lens, AX-Axicon lens, DF-Dichroic filter, ADL-Achromat doublet lens, NF-Notch filter, FCL-Fiber collimating lens.*

Our primary goal was to evaluate the ability of the CSRS system in measuring the Raman spectra from different depths of a sample. Thus an important task was to determine the depth of focus of the developed system. This was done by following the method detailed in our earlier report [20]. In brief, the Raman spectra were measured by axially moving a 20 μm thick sheet of PMMA across the focus of the Raman excitation beam and then fitting a Gaussian to the plot (shown in Figure 5.3a) of the intensities of the characteristic Raman peak of PMMA (at 1450 cm^{-1}) versus the axial distance. It is seen from Figure 5.3a that though the measured profile of the data points does not follow a true Gaussian at the top where it is a bit

flattened owing to the mixing of two Gaussian components resulting from the convergence of the illumination rings [103], it follows a Gaussian behavior elsewhere. Therefore, the full width at half maximum (FWHM) of the fitted Gaussian, measured to be ~0.9 mm, was taken as a practical estimate of depth resolution of the CSRS system.
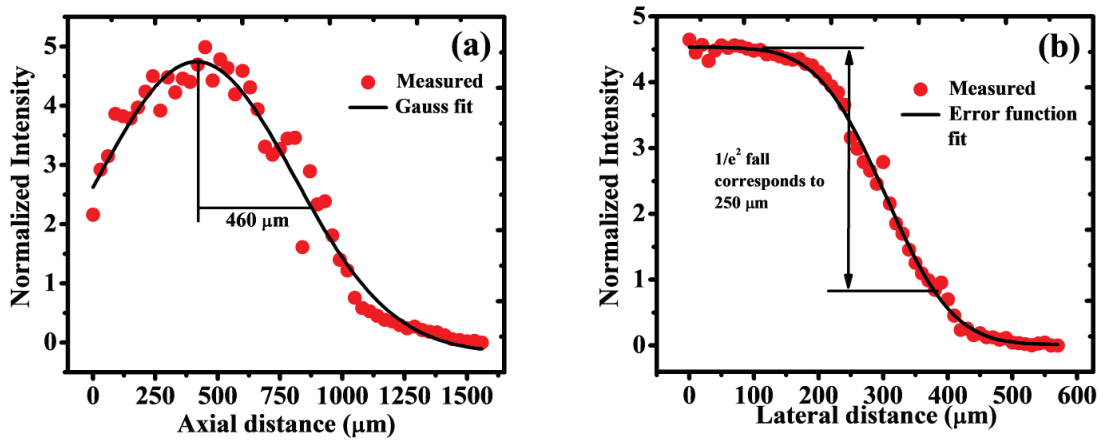
Figure 5.3: *(a) Plot of the intensities (red dotted points) of the characteristic Raman peak of PMMA (at 1450 cm^{-1}) versus the axial distance. The solid black line represents the Gaussian fit. (b) Plot of the intensities (red dotted points) of the characteristic Raman peak of PMMA (at 1450 cm^{-1}) versus the lateral distance. The solid black line represents the error function fit.*

The spot size at the focal plane was estimated by following the edge response method described elsewhere [20, 104]. In this method, the focus of the Raman excitation beam was laterally scanned over a clean edge of a PMMA layer of thickness 20 µm and the fall in the intensity of the 1450 cm^{-1} Raman peak was noted (Figure 5.3b). An error function was fitted to the measured Raman intensities. The lateral movement of sample stage corresponding to the point where the intensity dropped to $1/e^2$ was taken as a measure of the spot size which was found to be 250 µm (Figure 5.3b).

The performance of the CSRS system was evaluated first by measuring the depth-sensitive Raman spectra from a layered non-biological phantom made of paraffin and acetaminophen and then from a biological system having a layered structure. The phantom

was made by depositing a paraffin layer (thickness ~1.9 mm) over a ~3.5 mm thick acetaminophen substrate. The tissue sample was a chicken tibia with muscle tissue (thickness ~2.3 mm) on its top. The Raman spectra so measured were processed using a routine methodology as described in the Chapter 2 and normalized with respect to its mean intensity over a spectral range of 750-1750 cm^{-1}. The optical power onto the sample surface was measured to be 60 mW.

For the measurement of the Raman spectra from various depths of the samples investigated, the focal plane of the Raman excitation beam was moved axially by varying the separation between the two axicons (AX1 and AX2 in Figure 5.2). The calibration between the separation of the axicons (AX1 and AX2) and the axial shift in focal plane was done with the help of a thin (~10 μm) layer of PMMA. First, for a fixed position of the two axicons, the sample stage was axially adjusted to measure the Raman spectra of the PMMA layer and the position of the stage corresponding to the maximum signal intensity was noted. The separation between the axicons was then increased to cause an axial shift of the focal plane downwards. The sample stage was again adjusted (by moving it downwards this time) for measuring the Raman spectra of the PMMA layer and the position of sample stage corresponding to the maximum signal intensity was noted as before. The difference between the two axial positions of the sample stage (corresponding to the maximum Raman intensities) provided the axial shift in focal plane for the corresponding separation between AX1 and AX2. These axial shifts (in free space) corrected with the respective refractive indices of the samples using the method suggested by Everall et al. [25] provided the required calibration of axial shifts of the focal plane within the samples. For each 500 μm separation between the axicons (AX1 and AX2), the axial shifts of the focal spot into the phantom and tissue were found to be ~0.18 and 0.19 mm respectively. Though these values increased with depth due to the progressive increase in the normalized radius of the focusing lens (defined as

the ratio of the radius of the illumination beam and the true radius of the lens), this increase was found to be very small (only at the third decimal place) over the probing depth in the samples investigated by us. In order to effect the axial movement of the focal plane for probing different depths inside a sample, it was necessary to first determine the absolute position of the focal plane with respect to the sample surface that would serve as the reference. This was done by placing a 10 μm thick PMMA layer over the sample surface, adjusting the axial position of the sample stage corresponding to the maximum intensity of the PMMA Raman signal for a fixed position of the axicons, removing the PMMA layer from the sample surface and then axially moving the sample stage upwards by 10 μm.

5.4 Results and discussions

The Raman spectra were measured from the different depths of the non-biological phantom by varying the focal point of the excitation beam in steps of 0.18 mm. Figure 5.4a shows the Raman spectra measured from four different depths of the phantom, two from top and bottom extremities and two from the intermediate depths. Each spectrum is the average of three spectra corresponding to three different lateral positions separated by ~1 mm from each other. Figure 5.4b shows the Raman spectra of the authentic samples of paraffin and acetaminophen measured with the same experimental set-up. It is amply evident from the Figure 5.4a that when the focus of the excitation beam changes from top paraffin to bottom acetaminophen layer, the intensities of the Raman bands ~1295 and 1440 cm^{-1}, characteristics of paraffin Raman spectrum, decrease and that for the bands ~855, 1328 cm^{-1} and the triplet peaks between ~1550 to 1650 cm^{-1}, characteristics of acetaminophen spectrum, increase. In Figure 5.4c, the ratio of the intensities of the Raman peaks at 1610 cm^{-1} and 1440 cm^{-1} (i.e. I_{1610}/I_{1440}) is plotted as a function of the axial positions of the focus of the Raman excitation

beam inside the phantom. Error bars represent ±1 standard deviation corresponding to three different spectra measured from three different lateral positions.
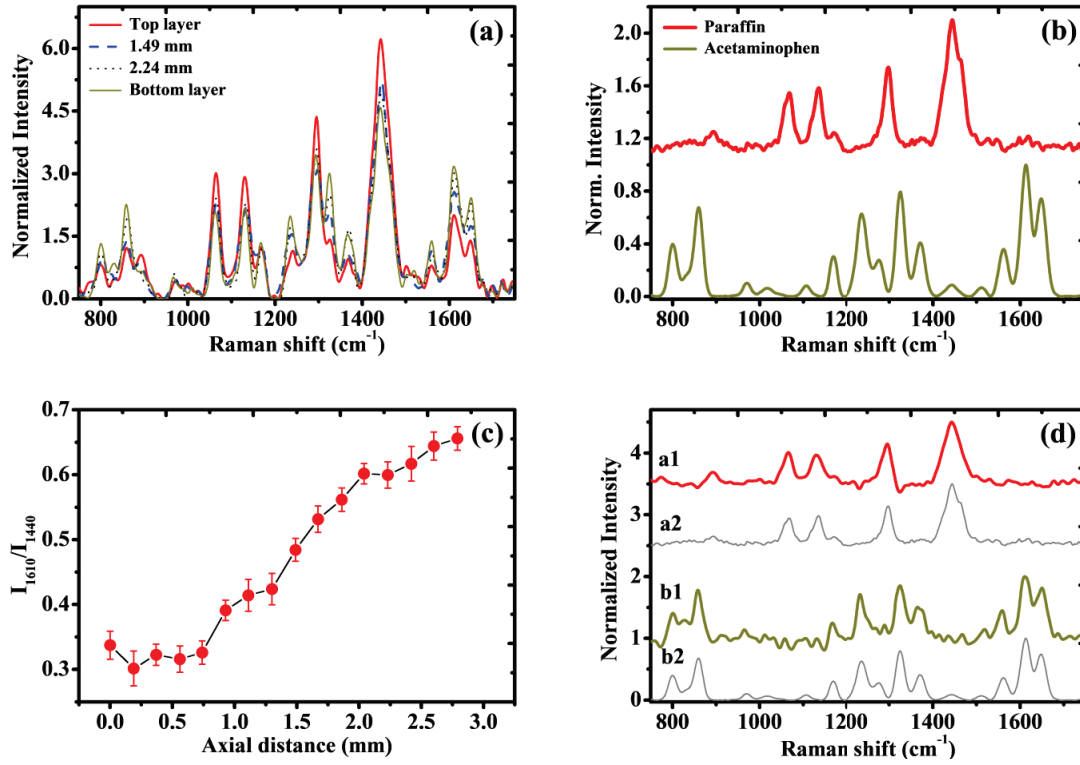
Figure 5.4: *(a) Mean normalized Raman spectra corresponding to four different depths of the phantom. Each spectrum is the average of three spectra corresponding to three different lateral positions separated by ~1 mm from each other. The integration time for each of these measurements was 5 s. (b) Reference Raman spectra of paraffin (upper panel) and acetaminophen (lower panel). Both the spectra are peak normalized. (c) The ratio of the intensities of the Raman bands corresponding to 1610 cm^{-1} and 1440 cm^{-1} (I_{1610}/I_{1440}) at different axial distances of the phantom. Error bars represent ±1 standard deviation corresponding to three different spectra. (d) Raman spectra of paraffin (a1) and acetaminophen (b1) retrieved through the scale subtraction technique, along-with the reference Raman spectra of paraffin (a2) and acetaminophen (b2).*

One may note that when the Raman excitation beam is focused onto the top layer, the 1440 cm^{-1} Raman peak characteristic of paraffin dominates, giving the lowest value (~0.32) of the peak ratio (I_{1610}/I_{1440}). Similarly, when the focus lies at the bottom acetaminophen layer, the ratio value is the largest (~0.66). It is also apparent from Figures 5.4a and 5.4b that

despite significant differences in the Raman spectra at different depths, there is considerable mixing of spectral signatures even for the top and bottom layers although the layers have distinctly different chemical make-ups. It is important to mention here that this mixing of signals could be lowered only marginally (by improving the depth resolution of the system), but it was not possible to fully eliminate it. The reason behind this unavoidable mixing of signals is the contamination of the Raman spectrum of the probed layer inside the sampling volume by the Raman scattered light coming from the out of focus planes. In fact, the sampling volume is determined by the axial point spread function which has quite broad wings (as seen in Figure 5.3a). Thus, weak signals emanating even from regions quite distant from the point of the tightest focus contribute to the detected signal.

In order to retrieve the characteristic Raman spectra of the two layers, the Raman spectra measured at the two depths (i.e. top and bottom) were subjected to the method of scale-subtraction as described in the Chapter 2. In this technique the spectrum from one layer was subtracted from that of the other after scaling them in ratios estimated using intensities of Raman peaks unique to each layer (i.e. I_{1610}/I_{1440}). Figure 5.4d shows the Raman spectra extracted from the spectra measured with the excitation beam focused onto the top and bottom layers of the phantom respectively. For the sake of comparison, the spectra of the authentic samples of paraffin and acetaminophen are also shown in the same figure. It can be seen from the figure that all the Raman peaks observed in the extracted spectra of the top (a1) and bottom (b1) layers have a very good match with those found in the Raman spectra of the authentic chemicals (a2 and b2) constituting the layers. In order to quantify the extent of overlap, the correlation coefficient (R^2) was calculated between the extracted and the authentic spectra. The R^2 values for the top and the bottom layers were found to be 0.85 and 0.88 respectively indicating a very good correlation. For further confirmation, the ratios of intensities of the characteristic Raman peaks of paraffin at 1440 cm^{-1} and 1295 cm^{-1} and of

acetaminophen at 1610 cm^{-1} and 1326 cm^{-1} were calculated for the retrieved Raman spectra of the top and bottom layers. The ratio values turned out to be 1.55 and 1.19, respectively and were found close to the corresponding ratio of intensities (1.59 and 1.27 respectively) calculated for the respective authentic Raman spectra.
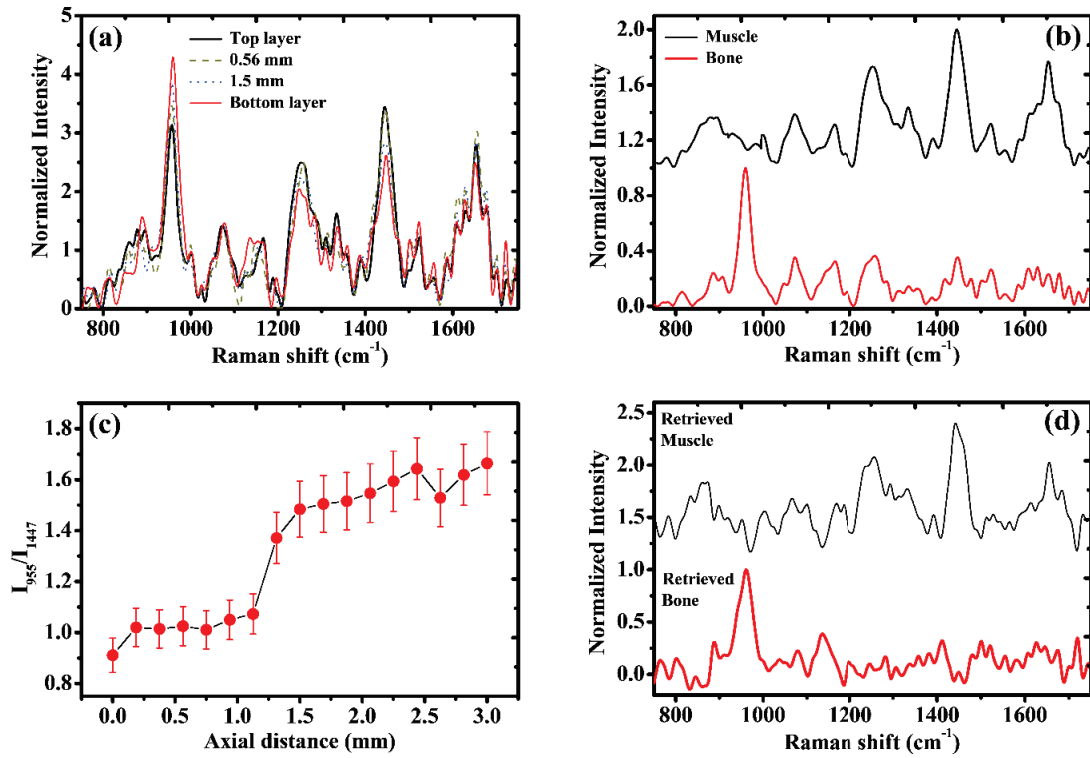
Figure 5.5: *(a) Mean normalized Raman spectra corresponding to four different depths of the chicken tibia. Each spectrum is the average of three spectra corresponding to three different lateral positions separated by ~1 mm from each other. The integration time for each of these measurements was 10 s. (b) Reference Raman spectra of muscle (upper panel) and bone (lower panel). Both the spectra are peak normalized. (c) The ratio of the intensities of the Raman bands corresponding to 955 cm^{-1} and 1447 cm^{-1} (I_{955}/I_{1447}) at different axial distances of the chicken tibia. Error bars represent ±1 standard deviation corresponding to three different spectra. (d) Raman spectra of muscle (a1) and bone (b1) retrieved through the scale subtraction technique.*

Following validation in the non-biological phantom, the system was used to measure the Raman spectra from the different depths of the layered tissue sample. The relative changes in the Raman spectra at different axial positions inside the tissue sample were

monitored by shifting the focal spot in 0.19 mm steps. Figure 5.5a shows the Raman spectra of the tissue sample corresponding to four different depths. Similar to the earlier case, here also, each spectrum is the average of three spectra corresponding to three different lateral positions separated by ~1 mm. Figure 5.5b shows the Raman spectra of the muscle and bone measured separately with the same experimental system. As expected when the focus of the excitation beam is changed from the top muscle layer to deeper layers towards bone the intensities of the Raman bands at ~1655 cm^{-1} (amide-I), 1447 cm^{-1} (CH$_2$ bending) and the doublet located at ~1245-1300 cm^{-1} (believed to be due to amide-III) are found to decrease and that for ~955 cm^{-1} (believed to be due to phosphate) is seen to considerably increase. Figure 5.5c shows the plot of the ratios of the normalized intensities of the Raman peaks 955 cm^{-1} and 1447 cm^{-1} (i.e. I_{955}/I_{1447}) as a function of the different axial positions of the focal spot. Error bars represent ±1 standard deviation corresponding to three different spectra. One can clearly note that as the focus of the Raman probe beam moves from the muscle to the bone, the ratio value starts increasing indicating lesser contribution of Raman signal corresponding to muscle which indeed is the case.

Figure 5.5d shows the Raman spectra retrieved through scale-subtraction from the spectra of top and bottom layers (shown in Figure 5.5a). A comparison of Figure 5.5b with Figure 5.5d clearly reveals that there is very good match between the Raman bands of the retrieved spectra of the top and bottom layers with those found in the spectra measured separately from the corresponding tissue types. The estimated R^2 values for the respective tissue layers were found to be 0.68 and 0.60 respectively indicating reasonable correlation. The ratios of the intensities of the Raman peak at 1655 and 1447 cm^{-1} in the retrieved spectrum of the top tissue layer and at 1078 and 955 cm^{-1} in the retrieved spectrum of the bottom tissue layer were found to be 0.63 and 0.25 respectively. The corresponding ratios derived from the respective native tissue spectra were found to be 0.76 and 0.34, which were

indeed close to those calculated for the retrieved Raman spectra of the respective tissue layers.

For the chicken soft tissue used in our experiment the transport path length was estimated to be ~2.3 mm which was consistent with the values reported by others [88-90]. Thus it was possible to achieve a probing depth of at least ~2.3 mm in the chicken soft tissue. Further, since the probing depth also depends on the depth of focus of the focusing element and for that the CSRS setup used an axicon which had a depth of focus of ~0.9 mm, a slightly larger probing depth of ~2.8 mm in the said tissue sample could be achieved with the present setup. Beyond this, as the excitation beam penetrated deeper in the tissue, the exponential increase in the ratio between the multiply scattered and un-scattered light intensities [105-106] caused it to totally lose its focusing ability making the excitation beam overly blurred and causing CSRS to completely lose its depth-selectivity. To confirm that CSRS loses its depth-selectivity when the excitation light is totally diffused, it was used to measure Raman signal from a piece of bone and also a 2 mm thick sheet of polyethylene through a slice of chicken soft tissue of thickness of ~4 mm, a depth much greater than the estimated transport path length. No Raman signal characteristic of either bone or polyethylene could be detected with CSRS even with integration time of >120 s. Further, to see up to which depth the excitation light can retain its focusing ability, the Raman excitation beam was axially moved through a slice of chicken soft tissue, each time with a different thickness, placed on the top of a 20 μm thick sheet of polystyrene and the intensities of the characteristic Raman peak of polystyrene (at 1000 cm^{-1}) were plotted with the axial distance to generate the axial response of the system, similar to that in Figure 5.3a. The axial profiles so generated for different thicknesses (0.6, 1.0, 2.0, 2.4 and 3.0 mm respectively) of the tissue slices are shown in the Figure 5.6. The zero axial distance in the figure denotes the position (inside a given tissue

slice) from where measurement of Raman signal was started and it was different for the different thicknesses of the tissue slices investigated.
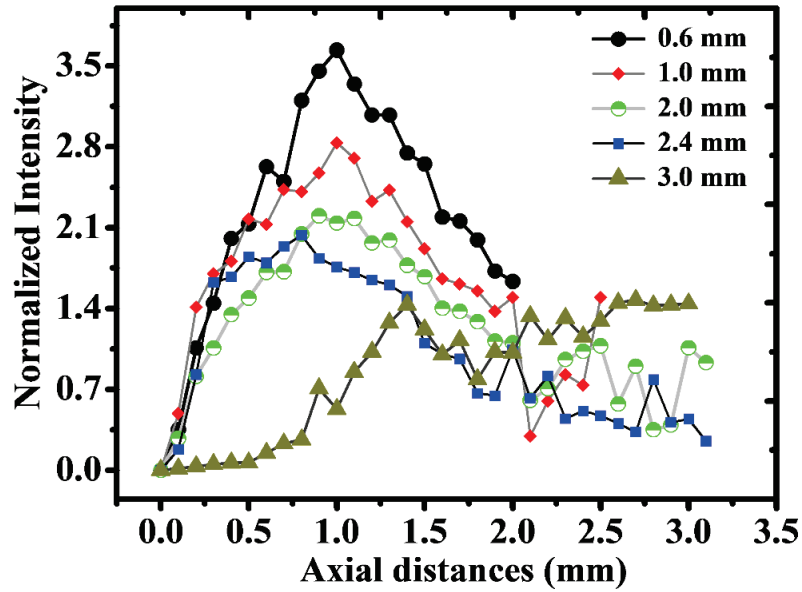
Figure 5.6: *Axial profiles for different thicknesses of the tissue slices*

It is apparent from the figure that for a given tissue slice, the intensity of polystyrene Raman peak first starts increasing as we move through the tissue depth, reaches a maximum and then starts decreasing as we go past the polystyrene sheet and this trend is almost similar for all tissue thicknesses except for the tissue slice with thickness of 3.0 mm (i.e. maximum probing depth) where it starts almost flattening. It is apparent from these results that CSRS could reject most of the multiply scattered light that reached the focal plane, until the optical depth became large enough to overwhelm the un-scattered component of the incident flux.

Besides the flexibility of CSRS in generating other sister configurations of depth-sensitive measurements, the approach has one unique advantage over the existing competitive approaches. In contrast to the earlier mentioned schemes (i.e. CRS, RCPRS and OCRS) where probing depth is confined to only few tens to hundreds of micrometers beneath the sample surface thereby limiting their use for layered samples requiring larger (several

hundred micrometers to few mm) depths to be probed, the CSRS allows one to probe large depths (of the order of few mm). In fact, it was found that the present system was good enough to recover the Raman spectra of bone by probing it through a soft tissue of ~2.3 mm thickness. The results of the studies described above therefore demonstrate the potential of CSRS as a viable technique for carrying out depth-sensitive Raman measurements beyond the reach of conventional techniques. Another important attraction of CSRS is the simplicity with which a particular depth inside a layered sample can be probed. For example, in CRS, one needs to vary the distance between the microscope objective lens and the sample being interrogated for reaching different depths. This, in turn, requires some adjustments in the sample arm of the instrument which may not be feasible (or desired) during various non-contact measurements. In CSRS, on the other hand, the probing depths can be varied by simply varying the separation between the two axicons which lie immediately adjacent to the excitation laser (see Figure 5.2). Since these axicons are independent of the sample arm, it amounts to having a remote handle in varying the probing depths inside a sample without requiring any manipulation inside the sample arm.

5.5 Summary

In this chapter, development of a depth-sensitive Raman spectroscopic system using a novel configuration of cone-shell excitation and cone detection has been shown. The development of the system involved three identical axicons for Raman excitation (of the target sample) in the form of a hollow conic section. The Raman scattered light from the sample, passed through the same (but solid) conic section, was collected for the detection. The performance of the system was evaluated on a layered non-biological phantom (comprising paraffin and acetaminophen) and a biological tissue sample (chicken tibia). It was found that the system

could recover Raman spectra of layers located at depths of ~2-3 mm beneath the surface. Apart from this ability of probing much larger depths compared to the previously mentioned schemes of depth-sensitive Raman measurements, the other attraction of the system is that it does not require any adjustment in the sample arm for reaching various depths inside a sample. Instead, it can be achieved by modulating the excitation arm (through change in the spatial separation between axicons), a significant advantage for non-contact, depth-sensitive measurement. However, a limitation of the technique is that the collection is primarily achieved through axicon lens which is known to have much poorer collection efficiency as compared to a normal lens or a microscope objective lens [107]. As a consequence the SNRs of the depth-sensitive Raman spectra measured using this approach are poor particularly while probing deeper. This issue will be addressed by using SORS the details of which are presented in the next chapter.

CHAPTER 6

Inverse spatially-offset Raman spectroscopy for detecting a low Raman-active turbid sample buried in a highly Raman-active matrix

6.1 Introduction

The technique based on CSRS, described in the previous chapter, has shown its potential in measuring Raman signal from depths beyond the reach of CRS, RCPRS and OCRS. Despite offering several advantages, a major limitation of CSRS is that the axicon lens used (in the collection arm) has poorer collection efficiency as compared to a normal lens or a microscope objective lens [107]. For example, we experimentally found that an objective lens (10X, NA = 0.25) can collect ~50% more Raman signal as compared to that gathered by an axicon lens of apex angle $140°$. The SNR of the measured Raman signal thus becomes low and a longer integration time is generally required for acquiring the Raman spectra of acceptable quality from biological samples. A technique which not only solves this problem but also can probe larger depths is inverse SORS. The technique is a variant of SORS [17, 21-22], an approach in which Raman signals are collected from the regions away from the point of illumination on the sample surface for identifying and analysing Raman-active turbid samples concealed deep inside another diffusely scattering Raman-active material of thicknesses of several millimetres. Inverse SORS provides the same set of information as the SORS but with interchanged positions of the illumination and collection points through the use of

illumination rings of varying radii and collection of Raman signal from the centre of these rings. It makes use of an axicon lens for converting the collimated laser beam into ring shaped beam and achieves the ability of subsurface interrogation by varying the radii of the illumination rings thereby introducing spatial offsets between collection and illumination. Unlike CSRS, in this technique, the axicon lens is used only for the illumination, not for the collection which allows measurement of the Raman signal with smaller acquisition time. In Chapter 1, we have discussed that SORS has shown its potential in a variety of biomedical applications, in recent past [21-22]. However, a careful review of the broad range of applications (including non-biomedical too) of inverse SORS as well as its conventional form reported thus far brings out one important observation common to all. The surface and sub-surface Raman active materials of the samples used in all these studies had marginal differences in the Raman cross-sections. Either both the materials were highly Raman active, for example, the active pharmaceutical ingredients in tablets [108-112], explosives hidden inside a plastic bottle [31, 113-115] etc., or both of them were having much lower Raman cross-sections, e.g. layered biological tissues [18-19, 57-60, 65]. There is no published report thus far where substantial difference is seen in the Raman cross-sections of the surface and the sub-surface materials comprising the sample. Two possibilities may arise in such a situation, one in which the sample might consist of a topping of low Raman cross-section overlaying a material which is highly Raman-active, and the other, where a low Raman-active sample might underlay a material of much larger Raman cross-section. While in the first case, detecting a highly Raman active sub-surface target is not expected to pose any difficulty, in the second case, interrogation of a sub-surface target of low Raman cross-section might be challenging due to the availability of a much smaller number of diffuse Raman photons from the target layer. Further, it is important to note that various applications like non-invasive diagnosis of the pathologic state of a tissue through intact FFPE tissue

blocks, non-destructive monitoring of packaged food products, etc. mimic the condition of the second case.

In this chapter, we present the results of a study to evaluate the applicability of inverse SORS on samples comprising a low Raman-active turbid material buried inside a diffusely scattering matrix of significantly higher Raman cross-section. An inverse SORS set up developed employing ring illumination and point collection on the surface of the sample was used for the study. Paraffin sandwiched tissue (PST) blocks, prepared by embedding biological tissue sections in solid paraffin blocks, were used as representative samples for investigating the efficacy of the inverse SORS in recovering the weak Raman signatures of the low Raman-active tissue from the background of a significantly stronger paraffin Raman. The Raman excitation beam was brought on to the surface of the PST blocks in the form of illumination rings of varying radii and the Raman signal was collected from the centre of this illumination ring. Since the Raman signal measured with different radii of the illumination ring contained different relative contributions of Raman scattered light from layers located at different depths within the block, it was possible to probe the target tissue embedded in the block by appropriately choosing the radius of the illumination ring. Further, the effect of sample turbidity on signal recovery and a comparative evaluation of the performance of inverse SORS relative to CSRS are also presented.

6.2 Principle of inverse SORS

The basic principle of inverse SORS detection has already been described in detail in the Chapter 1. However, one important component of such schemes is the axicon lens [31, 107] and elementary details of its working were not mentioned nowhere in the dissertation. The axicon transforms the incoming laser beam (collimated) into a ring-shaped beam. The width

of the ring is equal to the radius of the incoming beam, r_o as shown in Figure 6.1. Further, the internal radius of the ring, r_i is a linear function of the distance between the axicon and the plane at which the ring is being formed (i.e. d in the figure). Mathematically, the dependence of r_i on d is given by following equation [31]:

$$r_i = (d - D_0)\tan\beta \qquad \text{...... 6.1}$$

where the angle β depends on the refractive index of the lens material (n) and the base angle of the cone (α), as follows:

$$\beta = (n-1)\alpha \qquad \text{...... 6.2}$$
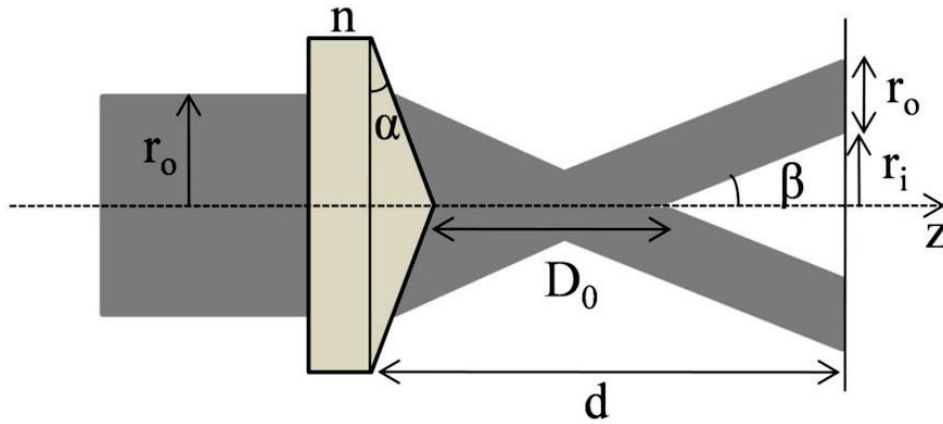
Figure 6.1: *Schematic of formation of a ring-shaped beam through an axicon lens. [Adapted from reference 31]*

The linear dependency of ring radius, r_i on the distance, d, is the main characteristic of the axicon lens which will be used in an inverse SORS system. In the system, the radius of the ring is a measure of the offset between the illumination zone and the collection point. The offset (or radius) therefore can be controlled by varying the distance of the axicon lens from the sample by mounting the lens on a sliding rail.

6.3 Materials and methods

A schematic of the inverse SORS experimental setup developed for the depth-sensitive Raman measurements is shown in Figure 6.2. It uses a 785 nm diode laser (DL785-100-SO, CrystaLaser) as the illumination source. The output of the laser is first collimated by an achromatic doublet lens (AC254-050-B-ML, Thorlabs Inc.) of focal length 50 mm and then spectrally purified using a laser clean-up filter (HQ782/20X, Chroma Tech. Corp.).
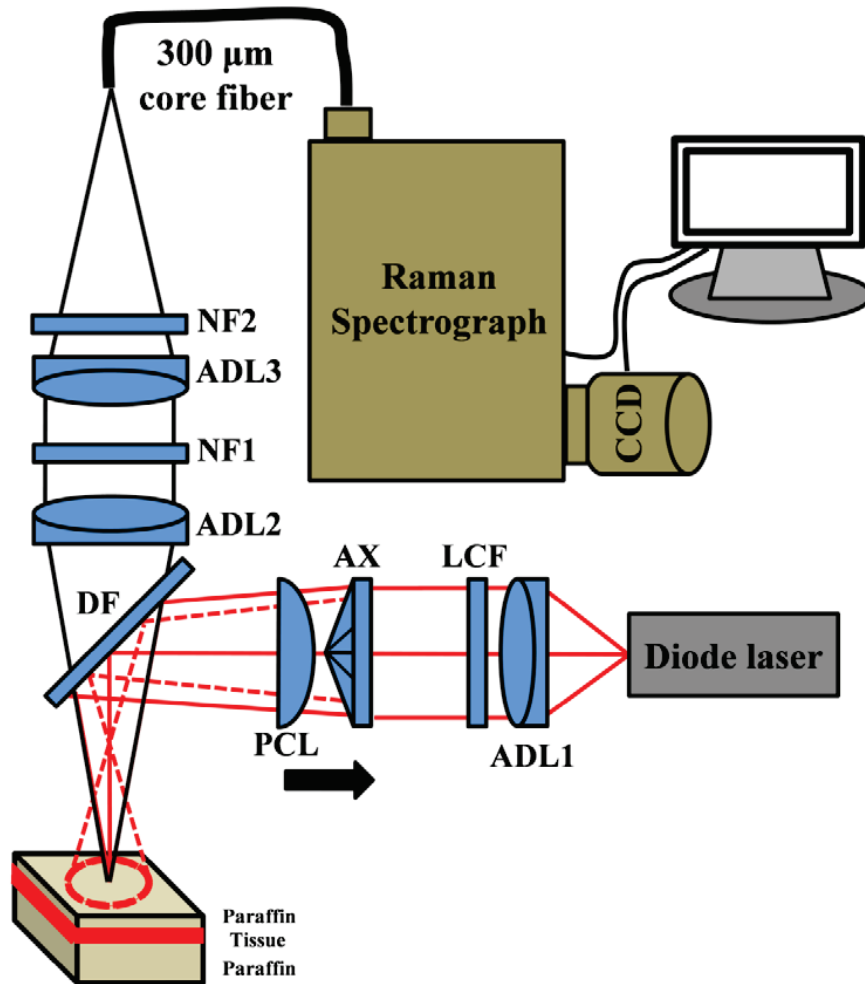
Figure 6.2: *Experimental setup of the inverse SORS for depth-sensitive Raman spectral measurements from the PST blocks. The abbreviations and their corresponding expanded forms are as follows: ADL-achromat doublet lens, LCF-laser clean-up filter, AX-axicon lens, PCL-plano-convex lens, DF-dichroic filter, NF-notch filter.*

An axicon (AXL) of apex angle 170° (1-APX-2-UV-E254, UAB Altechna) in combination with a plano-conex lens (PCL) of 35 mm converts the spectrally purified, collimated laser beam into a ring shaped beam. The plano-convex lens is placed in front of the axicon so as to make the radii of the resultant beam vary from very small (~0.16 mm) to around 5 mm over a working distance of ~50 mm. A dichroic filter (Di01-R355-25x36, Semrock Inc.) kept at an angle of 45° with respect to the axis of the axicon steers the ring-shaped collimated beam on to the sample surface. The zero-offset refers to the position of the lens-axicon assembly (closer to the dichroic filter) which condenses the ring-shaped illumination beam into a point illumination on the sample surface. The non-zero offsets refer to the positions of the lens-axicon assembly which form concentric rings of illumination on the sample and can be obtained by displacing the assembly away from the dichroic filter (in the direction of arrow). The radii of the rings correspond to the amount of non-zero spatial offsets between the illumination and collection points. The Raman signal backscattered from the sample is transmitted through the same dichroic filter (that transmits light above 800 nm), collimated by an achromat doublet (AC254-060-A-ML, Thorlabs Inc.) and then passed through two holographic notch filters (Narrow Notch-6, Tydex J. S. Co.) before it is coupled to an optical fiber of core 300 μm with the help of another achromat doublet (AC254-035-A-ML, Thorlabs Inc.) of focal length 35 mm. The light coming out of the distal end of the fiber is fed to an imaging spectrograph (SR-303i, Andor Shamrock) equipped with a thermoelectrically cooled, back-illuminated, deep-depletion CCD camera (DU420A-BR-DD, Andor) for depth-sensitive Raman spectral measurements.

The PST blocks, used in this study, were prepared by embedding slices of tissues into rectangular solid blocks of paraffin. The tissue samples used were from a chicken tissue and obtained from a local slaughterhouse. The tissue samples were cut into small pieces of ~1.5 cm x 1.5 cm cross-sections and of thicknesses varying between 0.5 mm and 2.0 mm. The

tissue slices were thoroughly rinsed with buffered saline to remove any residual blood. These were then put into cassettes of dimension 1.5 cm x 1.5 cm x 1.8 cm. The cassettes were filled with melted paraffin and kept at room temperature to allow the paraffin to solidify. The solid blocks of paraffin were then pulled out of the cassettes to obtain the PST blocks which contained the sections of tissues embedded in solid paraffin at various predetermined depths beneath the surface of the blocks. The thickness of the bottom layer of paraffin in these blocks was ~16-18 mm.

For the measurement of Raman spectra from the various depths of a PST block, the radii of the illumination ring on the surface of the sample were varied by displacing the lens-axicon assembly away from the dichroic filter through various distances. At the zero-offset position, spot size was estimated by an edge response method [20, 104] using a 10 μm thin PMMA layer and this came out to ~0.30 mm. The estimated diameter of the Raman collection zone on sample surface was found to be ~0.35 mm. The spectral resolution and SNR measured with an integration time of 1 s were found ~20 cm^{-1} and ~300 respectively for 1382 cm^{-1} Raman characteristic of naphthalene. For generating good quality Raman spectra from the PST blocks, the integration time used was 20 s. The optical power delivered onto the PST block was ~60 mW. The data pre-processing steps for the measured inverse SORS signals were similar to that mentioned in the Chapter 2. The minimum non-zero spatial offset taken for the measurements was 0.5 mm. Since the size of the Raman collection zone was less than 0.5 mm, the Raman signals from the rings were not collected.

6.4 Results and discussions

Figure 6.3a shows the mean Raman spectra of authentic paraffin and native chicken muscle tissue measured with spot illumination (i.e. zero-offset). The observed Raman bands at ~1062, 1130, 1295 and 1440 cm^{-1} in paraffin and at ~1265, 1330, 1450 and 1655 cm^{-1} in native tissue are seen to be consistent with the characteristic paraffin and tissue Raman bands reported in literature [7, 20, 43, 81].
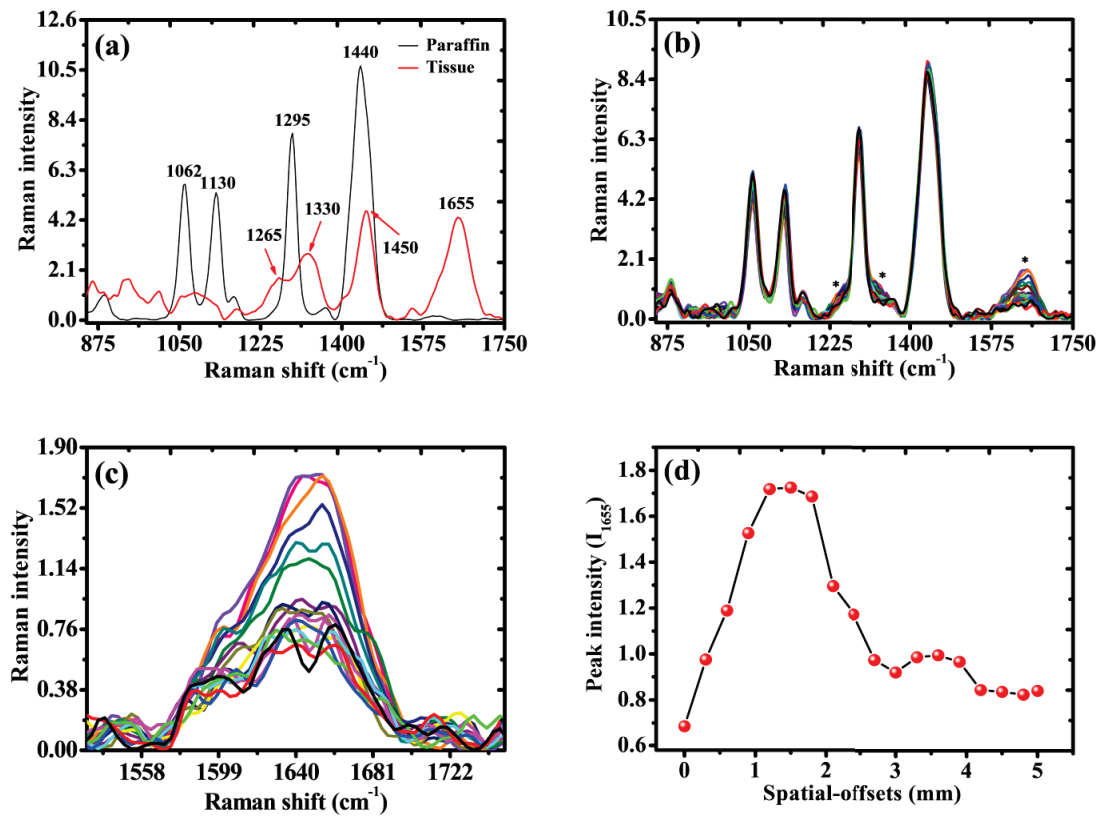
Figure 6.3: *(a) Conventional Raman spectra of authentic paraffin and native chicken muscle measured with spot illumination. (b) SORS spectra measured with different radii of illumination from the PST block containing 2.0 mm thick section of chicken tissue with a paraffin layer of ~0.5 mm thickness on its top. (c) Zoomed version of the prominent tissue Raman band appearing at ~1655 cm^{-1} of Figure 6.3b. (d) Plot of the peak intensities of the 1655 cm^{-1} Raman band as a function of the spatial offsets for the whole set of SORS spectra measured from the PST block corresponding to 2.0 mm thick tissue.*

In order to compare the relative signal strengths of paraffin and tissue, the ratio of the intensities of the tallest Raman peaks (~1440 cm^{-1}) in their respective background-removed, un-normalized spectra was calculated. The ratio, a rough measure of their relative Raman cross-sections (~1440 cm^{-1}), came out to be ~35. Figure 6.3b shows the SORS spectra measured with different radii of illumination from the PST block containing 2.0 mm thick section of chicken tissue with a paraffin layer of ~0.5 mm thickness on its top. It is apparent from the figure that the SORS spectra of the PST block at all the spatial offsets investigated have strong resemblance with the Raman spectrum of paraffin whose Raman cross-section is significantly higher than that of the biological tissues [43]. However, a closer look at the spectra reveals prominent dissimilarities appearing at ~1655 cm^{-1} and at the both sides of 1295 cm^{-1} paraffin Raman band. These locations, shown by a star symbol in the figure, are the fingerprint spectral regions where characteristic tissue Raman signatures are expected to appear. Figure 6.3c shows the zoomed version of the prominent tissue Raman band appearing at ~1655 cm^{-1}. It is observed that there is significant variation in the spectral intensities of this Raman band. Figure 6.3d plots the peak intensities of the 1655 cm^{-1} band, indicative of the content of tissue Raman signatures in the SORS spectra, as a function of the SOs for the whole set of SORS spectra measured from the PST block. One can see that the Raman intensity increases with increasing spatial offsets up to an offset of ~1.5 mm, beyond which it starts decreasing with increasing offsets signifying lesser contribution of tissue Raman signal corresponding to these offsets. Since the Raman band corresponding to the spatial offset of 1.5 mm shows the maximum intensity, one might expect that the respective Raman spectrum would contain the maximum tissue Raman signatures.

In order to eliminate the paraffin Raman background and isolate the weak tissue Raman signatures buried in it, the full set of SORS Raman spectra of the PST tissue block was subjected to the method of scale-subtraction, described in detail in the Chapter 2. The

method requires at its input at least two spectra which have one or few spectral regions where non-overlapping spectral features are present. In the present case, the Raman spectrum corresponding to zero-offset was subtracted from each of the measured SORS spectra of the PST block corresponding to all the non-zero spatial offsets after scaling the peak intensity of the 1130 cm^{-1} Raman band (unique to paraffin) of these spectra to the same height as that of the zero-offset Raman spectrum. The choice of zero-offset Raman spectrum for use in scaled-subtraction was dictated by the fact that it shows the maximum resemblance with the authentic paraffin Raman spectrum while minimum resemblance with the typical tissue Raman signatures (throughout the spectral region).
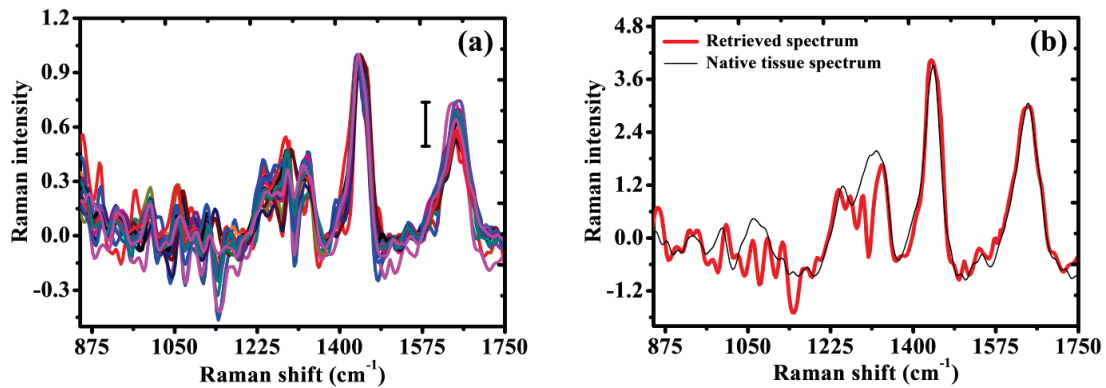
Figure 6.4: *(a) SORS spectra retrieved through scale-subtraction from the spectra shown in Figure 6.3b. (b) Scale-subtracted spectrum corresponding to the optimal spatial offset of 1.5 mm (that led to the SORS spectrum most representative of tissue) along-with the reference spectrum of native tissue measured with zero-offset.*

Figure 6.4a shows the SORS spectra retrieved through scale-subtraction from the spectra shown in Figure 6.3b. It is apparent from the figures that the retrieved spectra resemble the Raman spectra of native tissue except for a few spikes with intensities extending even in the negative. These spikes are the unavoidable artifacts that result during scale-subtraction from those parts of the characteristic paraffin Raman bands (appearing in the zero-offset SORS spectrum) which show a very subtle mismatch in line shape with that of the corresponding paraffin Raman bands contained in the SORS spectra of the PST block

corresponding to non-zero spatial offsets. Though appropriate spectral smoothening can reduce the height of these spikes or even eliminate them in some situations but the process almost flattens many of the tissue specific spectral signatures resulting in further distortions in the scale-subtracted spectra. Figure 6.4b shows the scale-subtracted SORS spectrum corresponding to the spatial offset of 1.5 mm which was found to lead to the most representative tissue Raman spectrum having the maximum intensity of the 1655 cm^{-1} Raman band characteristic of tissue. For the sake of comparison, the Raman spectrum of the native tissue measured with zero-offset is also shown in the same figure (i.e. Figure 6.4b). It is apparent that there is good match between the Raman bands of the retrieved spectrum with those found in the spectrum measured from the native tissue. For example, the 1655 cm^{-1} Raman bands appearing in the retrieved spectrum and in the native tissue spectrum are seen to be almost congruent in respect of both intensity and the width (FWHM). This appears to be due to the fact that at this spectral location paraffin does not have any of its characteristic Raman bands. One can also see that despite significant overlapping of the paraffin and tissue Raman signatures around 1450 cm^{-1} region, the characteristic tissue Raman band at this spectral location could be satisfactorily recovered with a deviation of only 3% in the peak intensity of this band from that of the native tissue Raman spectrum. Although a good recovery of the 1265 and 1330 cm^{-1} peaks is seen but the common shoulder of both the peaks is found to be distorted. The presence of paraffin characteristic at ~1295 cm^{-1} seems to be the main source of this distortion which is manifested as a negative spike. In the low wavenumber spectral region (~900-1200 cm^{-1}) the mismatch between the Raman bands of the retrieved and the native tissue spectra is found to be more conspicuous probably due to the relatively weaker intensities of the Raman peaks of tissue in comparison with those of paraffin. To quantify the overall recovery of tissue Raman spectrum, a correlation coefficient (i.e. R^2) was calculated. The computed R^2 value was found to be 0.83 indicating satisfactory

recovery. For further confirmation, the ratios of intensities of the characteristic tissue Raman peaks at 1655 cm^{-1} and 1450 cm^{-1} were calculated for the retrieved and the native tissue Raman spectra. It was found that the ratio of the intensities of the Raman peak at 1655 and 1450 cm^{-1} in the retrieved spectrum (0.75) was indeed close to the corresponding ratio derived from the native tissue spectrum (0.79).

In order to investigate the effect of the thicknesses of the tissue sections (estimated mean free path ~180 μm) contained in the PST blocks on the ability of the inverse SORS to retrieve the rather weak tissue Raman signatures, the SORS spectra were recorded with various spatial offsets from the PST blocks containing tissue sections of three different thicknesses, 0.5 mm, 1 mm and 2 mm. The blocks had a paraffin layer (estimated mean free path ~20 μm) of ~ 0.5 mm thickness overlaying all the tissue sections.
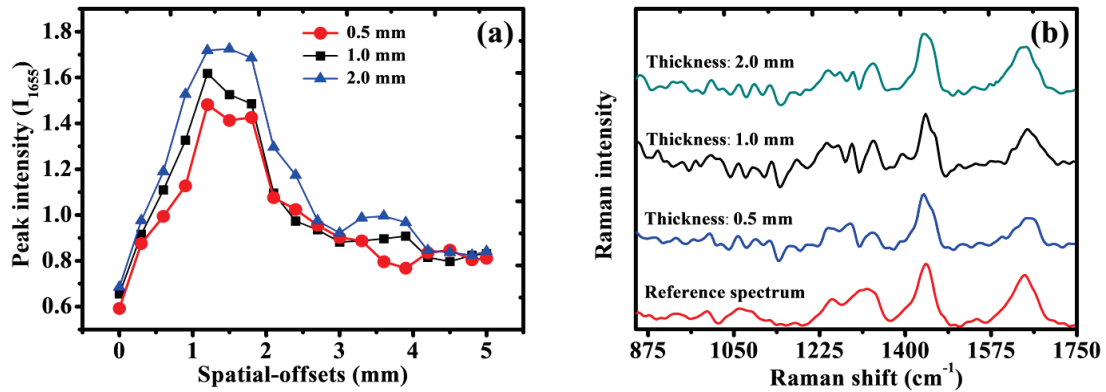
Figure 6.5: *(a) Plot of the intensities of the 1655 cm^{-1} Raman band as a function of the spatial-offsets from the PST blocks containing tissue sections of three different thicknesses, 0.5 mm, 1 mm and 2 mm. (b) Scale-subtracted inverse SORS spectra corresponding to the optimal spatial offsets from the PST blocks of three different tissue sections mentioned in Figure 6.5a along-with the reference spectrum of native tissue measured with zero spatial offset. For clarity, the spectra are shown with an offset.*

Figure 6.5a displays the plot of the intensities of the 1655 cm^{-1} Raman band as a function of the spatial-offsets used to measure the SORS spectra from these three blocks. It is apparent from the figure that the optimum offsets which led to the most representative tissue

Raman spectra for the PST blocks containing tissue sections of different thicknesses lie between ~1.2 and ~1.5. Figure 6.5b shows the spectra retrieved through scaled-subtraction from the SORS spectra of the PST blocks corresponding to the optimum spatial offsets. For comparison, the spectrum of the native tissue measured with zero spatial-offset is shown as the reference spectrum in the same figure. One can see that though the retrieval of the tissue Raman signatures is reasonably good in all three cases, it is the best in the case of the PST block containing the 2 mm thick tissue section with a 0.5 mm thick paraffin layer on its top.
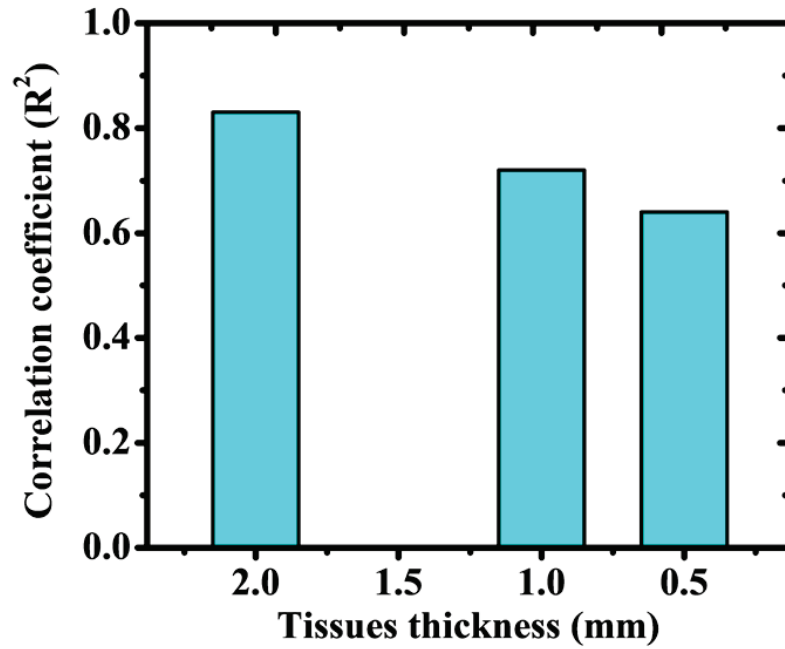
Figure 6.6: *The computed R² values (indicative of the extent of correlation) as a function of the tissue thicknesses*

Figure 6.6 shows the computed R^2 values indicative of the extent of correlation. It is clearly seen that the R^2 value is the maximum in the case of the retrieved spectrum from a 2 mm thick tissue section, whereas it is the least for the spectrum corresponding to the tissue section of 0.5 mm thickness. The plausible reason for the poorer recovery (i.e. decreasing values of R^2) in thin tissue sections is that with progressively diminishing tissue thicknesses the multiply scattered Raman photons generated from the deeper regions of the PST blocks

(and containing the strong paraffin signatures) start increasingly dominating the detected SORS signal. Alternatively, as the thickness of the tissue section decreases the availability of the diffuse Raman photons (corresponding to tissue) contributing to the measured Raman signal decreases thereby making the recovery difficult.

Following investigation of the effect of thickness of the embedded tissue sections on the recovery of the tissue Raman signatures, in the next step we investigated the effect of the thickness of the paraffin layer lying atop the tissue sections. In order to do so the SORS spectra were recorded from the PST blocks containing 2 mm thick tissue sections overlaid by paraffin layers of five different thicknesses: 0.2 mm, 0.5 mm, 0.75 mm, 1 mm and 1.5 mm. Figure 6.7 plots the Raman band at ~1655 cm^{-1} (in the measured SORS spectra of the PST blocks) for the different paraffin layer thicknesses corresponding to the optimum spatial offsets.
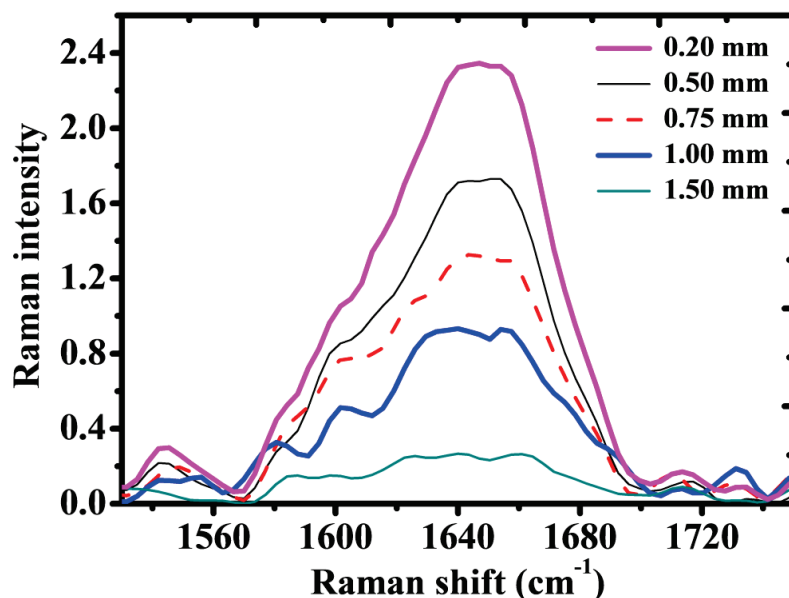
Figure 6.7: *Zoomed version of the prominent tissue Raman band appearing at ~1655 cm^{-1} of the PST blocks containing 2 mm thick tissue sections with overlaying paraffin layers of five different thicknesses: 0.20 mm, 0.50 mm, 0.75 mm, 1.0 mm and 1.50 mm.*

It is found that while the optimum tissue Raman signal is the largest for the PST block with the thinnest layer of paraffin (i.e. ~0.2 mm) beyond 1 mm thick paraffin layer hardly any tissue Raman signature is visible. This is not quite unexpected as may be clear from the following. The SORS uses diffuse photons for Raman excitation and predominantly seeks to collect only the multiply scattered Raman photons that are away from the illumination zone. Since with progressively larger thickness of the paraffin layer (overlaying the tissue) the multiply scattered Raman photons generated within this layer (of paraffin) between the surface and the sub-surface target tissue along with those generated in the region beneath the tissue section increasingly outnumber the weak tissue Raman photons, the detected SORS signal for a given spatial offset also starts getting increasingly dominated by the strong paraffin Raman signatures making, in turn, the recovery of the meaningful tissue Raman signal almost impossible beyond a certain thickness (~1 mm in the present case). Although a suitable choice of spatial offset allows one to collect more number of Raman photons generated within the thickness of the tissue section, due to significantly lower tissue Raman cross-section (in comparison with paraffin) these photons are not sufficient in number as compared to those generated within the layer of paraffin (with an increased thickness) so as to meaningfully contribute to the detected SORS signal. In order to verify this we prepared PST blocks where the thickness of the tissue section was increased to ~10 mm and measured the SORS spectra with various spatial offsets. As expected appreciable tissue Raman signatures started showing up and recovery was found to be possible for this tissue thickness even through a 2 mm thick paraffin layer (data not shown). It is pertinent to mention here that when the tissue section was replaced with a thin (~0.5 mm) layer of naphthalene, it was possible to recover the naphthalene Raman signatures even when the top paraffin layer thickness was ~10 mm further confirming the fact that it is indeed the relative Raman cross-section of the sub-surface material with respect to that of the surface which is one of the

important criteria (in addition to the other criteria of low or no absorption of the incident or Raman scattered light and no fluorescence of the sub-surface target material), for dictating the thickness of the surface through which one can identify the presence of the sub-surface target using the inverse SORS approach.

Since turbidity of the surface layer is also a factor that is expected to affect the probing depth and consequently the recovery of the sub-surface Raman signatures across different depths, we carried out an experiment to evaluate this aspect. Mock-up samples were prepared by using Teflon, paraffin and plastic (which were found to have different turbidity as confirmed by estimating their mean free paths), and sandwiching tissue sections (estimated mean free path ~180 μm) of ~3 mm thickness between two layers made of these materials. Different thicknesses (~500 μm, ~1 mm and ~3 mm) of these materials were used as the surface layer in these mock-up samples. In all the cases, the thickness of the bottom layer of the materials was ~15 mm. The results showed similar trends as observed earlier. For example, it was found that as the thickness of the top layer increased the relative intensities of the characteristic tissue Raman bands reduced and beyond a particular thickness almost no tissue Raman signal could be found. It was further observed that the probing depth was the least when the paraffin that had the highest turbidity (mean free path ~20 μm) was used at the surface, followed by Teflon (mean free path ~40 μm) and then plastic which had the minimum turbidity (mean free path ~2 mm). While for plastic one could recover tissue Raman signatures even beyond 5 mm depth, for Teflon and paraffin the corresponding depths were ~3 mm and ~1 mm, respectively. Further, it was found that the quality of recovery of the tissue Raman signatures fared poorer with increase in turbidity of the surface layer. For example, R^2 value (~0.85) for the 500 μm thick paraffin layer lying atop the tissue was found equivalent to that for the sample where ~1 mm thick Teflon layer was overlaying the tissue. In order to find the effect of the bottom layer thickness on the recovery of the tissue Raman

signatures, mock-up samples of varying thicknesses of bottom layers were prepared keeping the thickness of the tissue and the overlaying surface layer fixed. The observation was very similar to that when the thicknesses of the top layers were varied. For example, it was found that as the thickness of the bottom layer increased the relative intensities of the characteristic tissue Raman bands reduced with the recovery of tissue Raman signatures being the best when there was no layer beneath the tissue. However, unlike the top layers the relative intensities of the tissue Raman bands stopped reducing (remained almost unchanged) beyond a particular thickness of the bottom layer.

An important point to be noted here is that the characteristics of the laser beam brought onto the sample surface for CSRS (described in Chapter 5) look similar to those between inverse SORS mentioned above and the defocused SORS [53]. It is thus important to note that in CSRS, there is always a non-zero probability of collecting some multiply-scattered Raman photons which diffuse into the regions inside the collection cone not illuminated by the excitation light. This probability, while very less at shallower depths due to the presence of smaller number of diffuse Raman photons, considerably increases at larger depths since the number of the multiply scattered Raman photons increases progressively. A comparison between CSRS and inverse SORS is therefore required to understand the main difference between their configurations. In order to compare their relative performances, we used a two-layered phantom comprising a 2 mm thick slice of chicken soft tissue placed on a 10 mm thick block of naphthalene. The surface area of the phantom was ~30 mm x 30 mm. Figures 6.8a and 6.8b show the Raman spectra measured from the phantom with SORS and CSRS, respectively. The spectra correspond to two different offsets (in SORS) or two different depths (in CSRS) where the respective Raman signals characteristics of the two layers were the maximum.
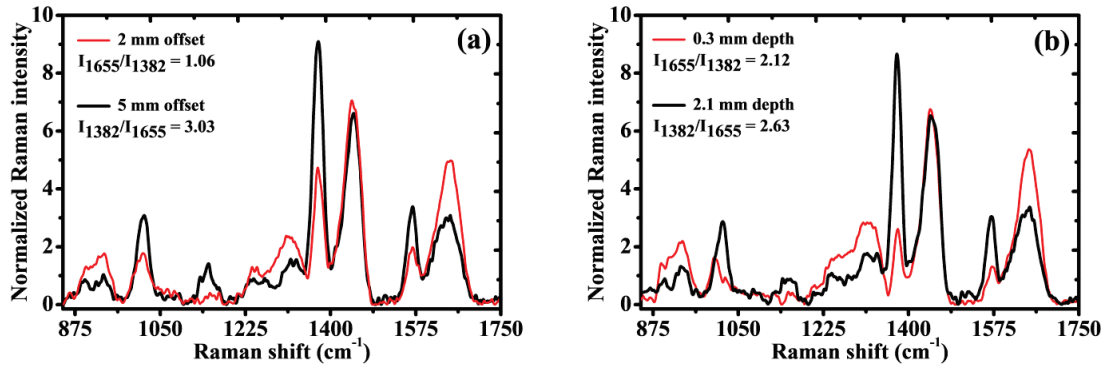
Figure 6.8: *Mean normalized Raman spectra of the two-layered phantom comprising a 2 mm thick slice of chicken soft tissue placed on a 10 mm thick naphthalene block. The spectra correspond to (a) two different offsets (in SORS) and (b) two different depths (in CSRS) where the respective Raman signals characteristics of the two layers were the maximum. The integration time used for each of these measurements was 20 s.*

It is apparent from the figures that for both SORS and CSRS there is considerable mixing of signals in the Raman spectra corresponding to each of the layers. For probing the top tissue layer, the level of signal mixing was expressed as the ratio of the intensity of characteristic tissue Raman peak at 1655 cm^{-1} to that of characteristic naphthalene Raman peak at 1382 cm^{-1}, I_{1655}/I_{1382} and for probing the bottom naphthalene layer, the inverse of this ratio (I_{1382}/I_{1655}) was used as a measure of signal mixing. One may note that the level of signal mixing for CSRS while probing the top layer (at ~0.3 mm depth) is considerably less (almost half) as compared to that for SORS. However, for probing the bottom naphthalene layer the signal mixing was almost comparable for the two, with SORS showing a slightly reduced level. This is not quite unexpected as may be clear from the following. The CSRS predominantly collected Raman photons generated within the focal zone of the excitation beam. Since at progressively larger depths the multiply scattered Raman photons cause the fiber aperture (acting as a pinhole in CSRS) increasingly lose its ability to reject light scattered outside the focal zone, especially within the region (inside the collection cone) between the surface and the focal plane, the signal mixing is expected to be considerably

more at larger depths as compared to the shallower depths. On the other hand, SORS uses diffuse photons for Raman excitation and intrinsically seeks to collect only the multiply scattered Raman photons that are away from the illumination zone. Thus, the level of signal mixing in probing larger depths is expected to be significantly less as compared to that while probing shallower depths.

6.5 Summary

To summarize, we have discussed the details of the studies carried out to evaluate the efficacy of inverse SORS in identifying the sub-surface layer of a low Raman active sample buried in a scattering matrix of much higher Raman cross-section. The effect of the thickness of the subsurface and the surface layers as well as the turbidity of the surface layer on the ability of the method to efficiently recover the weak sub-surface Raman signatures has been systematically investigated. The results of the studies demonstrate that unlike in the cases (when the differential in the Raman cross-sections between the surface and the sub-surface is marginal) where SORS can successfully probe a sub-surface diffusely scattering Raman active target through several millimetres of depth inside another Raman active turbid medium, the probing depth gets considerably reduced (~a few mm) when the Raman cross-section of the sub-surface target is significantly lower as compared to that of the layer overlaying it. A comparison between inverse SORS and the CSRS reveals that the former is very useful in deeper probing. However, the development of a clinically suitable hand-held inverse SORS probe requires smaller axicons (diameter = <10 mm or so) which are presently unavailable. A solution regarding this issue will be presented in the next chapter.

CHAPTER 7

Inverse spatially-offset Raman spectroscopy using optical fibers – An axicon lens free approach

7.1 Introduction

The results of the study described in the previous chapter clearly indicate that the inverse SORS has considerable promise for applications involving interrogation of deeper sub-surface depths. However, an important issue related to the implementation of the approach is that its classical configuration that employs axicon lens puts limit on making a compact and pencil-sized inverse SORS probe, an important requirement for *in-vivo* tissue analysis in a clinical setting. In this chapter, we report a novel scheme of implementing inverse SORS which overcomes the above mentioned issue and has the potential to make a clinically suitable SORS probe. The scheme eliminates the need of an axicon lens, and uses ring illumination and point collection through two multi-mode optical fibers. In the scheme, the ring shaped illumination is generated with a multi-mode fiber (lying in the source arm of the experimental set-up) kept at non-zero angle with respect to the axis of the lens used for focusing the laser light onto its tip. On varying this angle, the Raman illumination beam is incident onto the sample surface in the form of concentric illumination rings of varying radii. The back-scattered Raman light exiting the sample surface at the centre of the concentric rings is collected for the detection. The ability of the system developed based on the present scheme to measure Raman spectra of the subsurface layers is demonstrated using layered non-biological phantoms and biological tissue till a depth of ~3-4 mm.

7.2 Principle and background

The underlying principle of generation of ring shaped beam following passing of light through a multi-mode optical fiber is explained in the following. The light rays impinging on the core-cladding interface of the fiber at an angle greater than the critical angle ($\theta_c = \sin^{-1}$ (n_2/n_1); with $n_1 > n_2$; n_1 and n_2 respectively being the refractive indices of the core and cladding materials of the fiber) are trapped inside the fiber core as they satisfy the total internal reflection (TIR) condition [116-118]. Because of the cylindrical symmetry in the fiber structure, these rays suffer TIR at the lower interface also and therefore are guided through the core by repeated TIRs [116-118]. However, the guided rays inside the fiber core are of two types; meridional rays and skew rays.
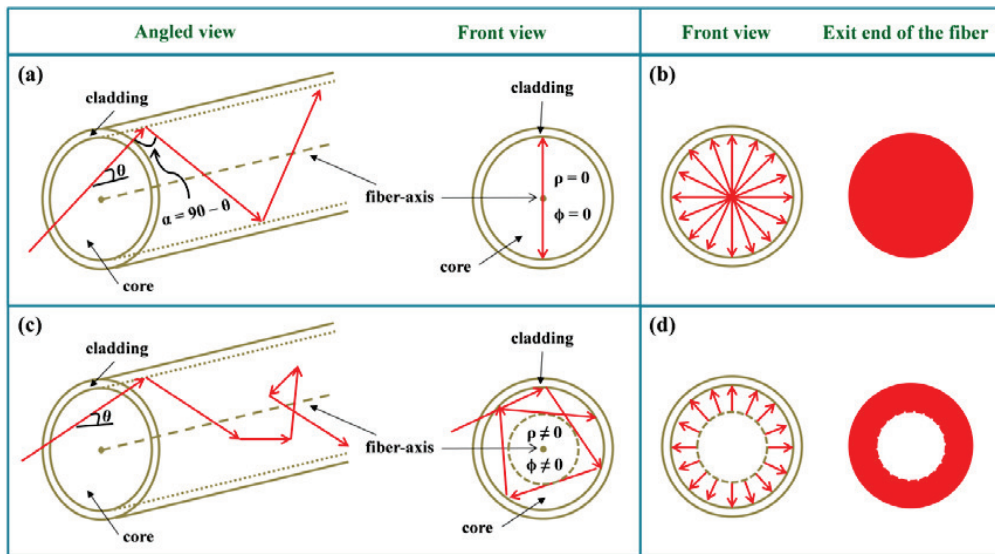
Figure 7.1: *Propagation path for a (a) meridional and (c) skew ray. Output beam patterns for a number of (b) meridional and (d) skew rays at the exit end of the fiber*

In Figure 7.1, the propagation paths of both the rays are shown. A meridional ray (shown in Figure 7.1a) incident on an angle, α, at the core-cladding interface gets totally internally reflected at the interface and crosses the fiber-axis. For this ray, the angle, α is

equal to $90° - \theta$ with θ, being the angle of incidence at the core-surface. In general, α is a combination of θ and ϕ (i.e. $\cos\alpha = \sin\theta.\cos\phi$), where ϕ is the perpendicular component of the incident angle and is given by following equation:

$$\sin\phi = \rho/r \qquad\qquad ...... 7.1$$

Here r is the radius of the core and ρ is known as the minimal approach towards the fiber-axis [118]. Since the meridional ray crosses the fiber-axis during its travel, both ρ and ϕ are set to zero for it. Although only one meridional ray is shown in Figure 7.1a, in practice there are an infinite number of meridional rays. Few of them are shown in "Front view" of the Figure 7.1b. Due to all such rays, at the exit end of the fiber a circular pattern of uniform intensity is generated as shown in Figure 7.1b. However, in reality, the intensity is not uniform in the complete circular region and decreases at the peripheral region having a maximum at the central portion due to the Gaussian nature of the light beam.

In contrast, a skew ray propagates without crossing the fiber-axis as shown in Figure 7.1c. This ray undergoes TIR with both ρ and ϕ set at non-zero [116-118]. In simpler words, the skew ray goes on spiralling around the fiber-axis. For a large number of skew rays, the light energy carried by them is effectively confined to an annular region around the fiber-axis as shown in Figure 7.1d. Consequently, at the exit end of the fiber, skew rays will have minimum energy at the fiber-axis and it will gradually increase towards the periphery of the core. This results in a ring shaped beam at the fiber-exit as shown in the Figure 7.1d.

Theoretically, an infinitesimal sized focus point may generate only meridional rays as shown in Figure 7.2a. However, in actual cases such situation is never obtained and the focus point at the core-surface always has a definite size (see Figure 7.2b). In such case, both meridional (preferably due to the cone shown in yellow colour) as well as skew (outside the yellow coloured cone) rays contribute and the resulting output at the fiber-exit is circularly

shaped with almost uniformly illuminated everywhere. In case of an angulated focusing, as shown in Figure 7.2c, the proportion of meridional rays rapidly decreases and most of the light is guided through the skew rays which results in an annular or ring shaped beam at the fiber-exit [119-121].
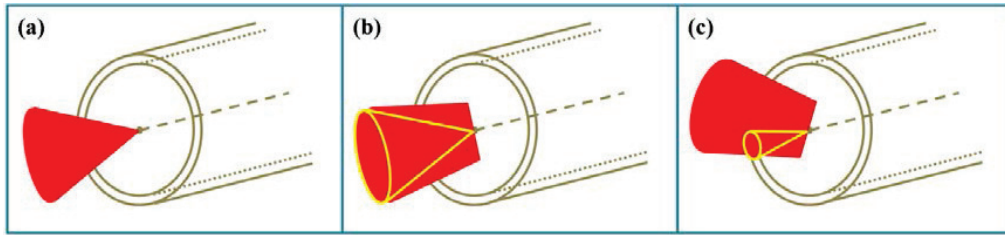
Figure 7.2: *(a) Focusing of light with an infinitesimal sized focal point at the core-centre which generates only meridional rays (b) Focusing of light with a definite focal point at the core-centre which generates both meridional and skew rays (c) Angulated focusing minimizes the number of meridional rays*

The ring formation using a multi-mode optical fiber is shown in Figure 7.3. The area of the central hollow region increases linearly with the incident angle due to continually decreasing number of meridional rays. Further, as the incident angle increases, the angle at the fiber-exit too increases resulting in the formation of concentric rings of light of increasing radii. Thus, by arranging to fix the point of collection (of the Raman signal) at the centre of the concentric rings of illumination on the surface of the target sample and by varying their radii by changing the angle of the incident illuminating beam (with the fiber surface), one can implement the inverse SORS technique in an experimental configuration without the use of any axicon lens.
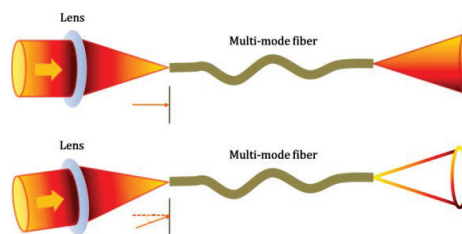
Figure 7.3: *Ring formation using a multi-mode optical fiber*

7.3 Materials and methods

Figure 7.4 shows the schematic of the experimental setup of the inverse SORS developed based on the proposed scheme of generation of concentric illumination rings using a multimode optical fiber.
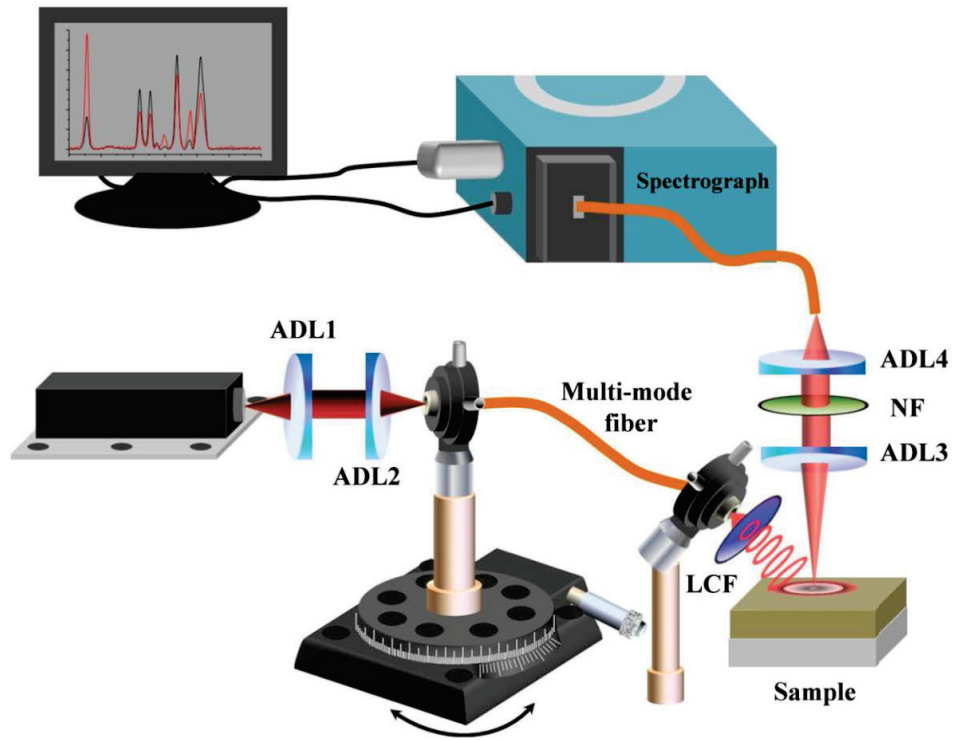
Figure 7.4: *Experimental setup of inverse SORS based on the proposed approach. The abbreviations and their corresponding expanded forms are as follows: ADL-achromatic doublet lens, LCF-laser clean-up filter and NF-notch filter.*

The laser light with a central wavelength of 785 nm from a diode laser (CL-2000, CrystaLaser) is first collimated by an achromatic doublet lens, ADL1 (AC254-050-B-ML, Thorlabs Inc.), and then focused onto the tip of a multi-mode fiber of core 600 μm (QMMJ-55-IRVIS-600/630-3-1, OZ Optics Ltd.) through another doublet lens, ADL2 (AC254-030-B-ML, Thorlabs Inc.). The illumination end of the fiber is mounted on a rotary stage for providing different angles to the fiber tip with respect to the optic axis of ADL2. On the distal

end of the fiber (where the light exits), a laser clean-up filter, LCF (ZET785/10X, Chroma Tech. Corp.) spectrally purifies the generated ring shaped beam prior to illuminating the sample surface. The Raman signal backscattered from the sample surface is collected from the centre of the illumination ring through the use of an additional doublet lens, ADL3 (AC254-050-B-ML, Thorlabs Inc.) situated in the collection arm of the setup. A notch filter, NF (NF03-785E-25, Semrock Inc.) removes the elastically scattered component from the light signal collected by ADL3 and passes only the Stokes shifted Raman signal. Finally, one more doublet lens, ADL4 (AC254-030-B-ML, Thorlabs Inc.) couples the Raman signal to a detection fiber (QMMJ-55-IRVIS-200/240-3-1, OZ Optics Ltd.). A Raman spectrograph (SR-303i, Andor Shamrock), connected at the other end of the detection fiber and equipped with a thermoelectrically cooled CCD camera (DU420A-BR-DD, Andor), measures the Raman signal and displays it on the screen of the computer interfaced with it.

For inverse SORS measurements, the angle between the tip of multi-mode fiber (placed in the illumination arm of the experimental set-up) and the lens, ADL2 was varied and different concentric illumination rings corresponding to different spatial offsets between the illumination and the collection (fixed at the centre of the rings) were created. An angle of 0°, where no ring was formed, corresponded to zero spatial-offset. For the non-zero angles, different concentric illuminating rings of varying radii were formed introducing non-zero spatial-offsets. The difference between the outer and inner radii provided the width of a given illumination ring. Table 7.1 lists the ring radii (on the sample surface) with their widths at different angles.

The procedures followed for spectral measurements and the data pre-processing steps were similar to what was described in details in Chapter 2. The inverse SORS spectra were acquired starting with an angle of incidence of 0° (corresponding to zero spatial offset) and then changing the angles in steps of 1°.

Table 7.1: *Characteristic of the illumination rings formed at different angles*

Angle	Outer radius (mm)	Inner radius (mm)	Width of ring (mm)
0°	2	-	-
1°	3	-	-
2°	4	0.5	3.5
3°	5	1	4
4°	6	2	4
5°	7.5	2.5	5
6°	8.5	3.5	5
7°	9	5	4
8°	9	5.5	3.5
9°	9	6	3
10°	9	7	2
11°	9	7	2

The performance of the developed inverse SORS system was evaluated using layered non-biological phantom and biological tissue. The non-biological phantom was a two-layered turbid medium comprising a cylindrical Teflon block (radius 16 mm and height 30 mm) underlying a piece of high density polyethylene (HDPE). The thickness of HDPE was varied from 1.3 mm to 3.9 mm. For measurements in biological samples, a chicken tibia obtained from a local slaughter house was used. The tibia was a bone embedded in a relatively thin layer of muscle. The thickness of the muscle was varied from 0.8 to 1.8 mm. The integration time used for Raman spectral measurements was 5 s for non-biological phantoms and either 5 s or 10 s for biological tissues depending on the quality of the observed Raman signal. The optical power delivered at the entrance tip of the fiber used to form ring illumination was 120 mW.

7.4 Results and discussions

The inverse SORS spectra measured at different angles (of the laser beam with the axis of the illumination fiber) from the two-layered non-biological phantom comprising 1.3 mm thick layer HDPE overlying the cylindrical Teflon block are shown in Figure 7.5a. The spectra are normalized with respect to their means over the displayed spectral range. For reference, the conventional Raman spectra (i.e. the Raman spectra corresponding to an angle of zero degree) measured from individual HDPE and Teflon are shown in Figure 7.5b.
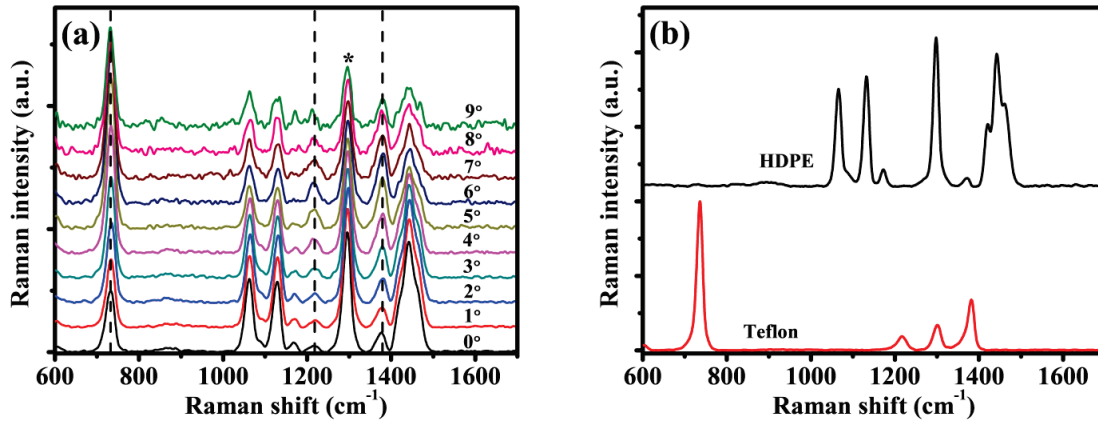
Figure 7.5: *(a) Inverse SORS spectra of non-biological phantom made of 1.3 mm thick HDPE deposited over a Teflon block. The angle dependent spectra are normalized with respect to their means over the displayed spectral range. The Raman peak marked by a star symbol represents the peak found common in both layers of the phantom. (b) Reference Raman spectra of individual HDPE (upper panel) and Teflon (lower panel).*

Based on the reference spectra, one can see in Figure 7.5a that as the angle of incidence is increased, the intensities of the four prominent Raman peaks (1066, 1130, 1296 and 1440 cm^{-1}), characteristic of HDPE which forms the top layer of the phantom, go down. However, a reverse trend is noted for the intensity of the 734 cm^{-1} Raman peak, characteristic of Teflon that forms the bottom layer.

Figure 7.6a plots the ratio of intensity of the characteristic Raman peak of Teflon at 734 cm^{-1} to the characteristic Raman peak of HDPE at 1440 cm^{-1}, I_{734}/I_{1440}, as a function of

the angle of incidence on the tip of the illumination fiber. It can be seen that the ratio first increases till an angle of 6º, then decreases slowly beyond 6º and finally reaches a constant value.
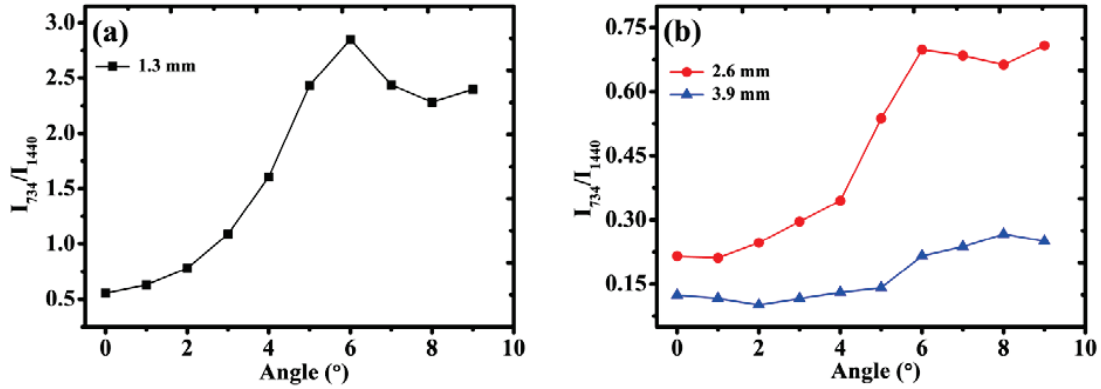
Figure 7.6: *(a) Plot of ratio, I$_{734}$/I$_{1440}$ as a function of angle for a HDPE thickness of 1.3 mm. (b) Plots of the ratio for two different thicknesses of the HDPE.*

The underlying reason behind this observed trend can be understood with the help of Table 7.1. In the table, one can see that the radius of the illumination ring formed at the sample surface increases monotonously with the angle of incidence till a particular angle (here 6º) is reached. Since all the rings formed at the sample surface are concentric with the centre being the point of Raman collection, an increasing angle of incidence leads to an increasing spatial offset between the illumination and the collection (satisfying the criteria of inverse SORS) [31], which is why the Raman signatures of the sub-surface Teflon appear more prominent in the measured Raman signal with a steady rise in the ratio. However, beyond the angle of 6º, one can see that the size of the illumination ring does not increase (i.e. becomes almost constant) with the increase in the angle of incidence, though its width starts decreasing rapidly making it considerably slimmer. This has two consequences. First, the incident photon flux onto the sample surface is getting considerably reduced, and second, the spatial offset becomes constant. While a constant offset puts a limit on the probing depth

thereby not allowing probing further deep, the considerably reduced photon flux leads to generation of much reduced number of Raman scattered photons within the depth of the phantom that can be probed. The Raman signal emanating from the bottom layer of the phantom, therefore, becomes weaker resulting in the lowering of the ratio. However, further increase in the angle of incidence does not result in any further increase in the outer radius of the illumination ring thus making the ratio remain almost constant beyond a certain angle ($\sim 8^{\circ}$ or so). Figure 7.6b plots the ratio, I_{734}/I_{1440} for two different thicknesses of the HDPE (2.6 and 3.9 mm respectively). One may note that for both the thicknesses the plots are similar to that seen with the HDPE thickness of 1.3 mm. This confirms that till 3.9 mm thick surface layer of a layered turbid medium the inverse SORS effect can be achieved.

Following evaluation of the performance of the inverse SORS setup, developed based on the proposed scheme, in layered non-biological phantoms, its performance was validated on layered biological samples. Figure 7.7a shows the Raman spectra of a chicken tibia measured at two different angles of incidence. The tibia had a highly scattering bone tissue beneath a 0.8 mm thick muscle tissue. While muscle is believed to have a plenty of protein and lipid molecules, phosphate (PO_4^{3-}) is known to be the main constituent of bone [7, 57-58]. As expected when the angle of incidence is changed from 0° to 6° the intensities of Raman peaks at ~ 1658 cm^{-1} (amide-I, C=O stretching), 1445 cm^{-1} (C-H deformation) and at 1250 and 1315 cm^{-1} (amide-III bands, C-N stretching and N-H in plane bending) are found to decrease and that for ~ 958 cm^{-1} (believed to be due to PO_4^{3-}) is seen to substantially increase. To further quantify the relative increase (or decrease) in the intensities of the peaks corresponding to muscle and bone, the ratio of peak intensities at 958 (bone characteristic) and 1445 cm^{-1} (primarily due to muscle) was calculated. While the ratio, I_{958}/I_{1445}, is found to be 0.58 for the Raman spectrum obtained with 0° angle of incidence, it is increased up to 0.99

in the spectrum corresponding to the 6º angle. The increased ratio clearly indicates the success of the technique in sub-surface probing.
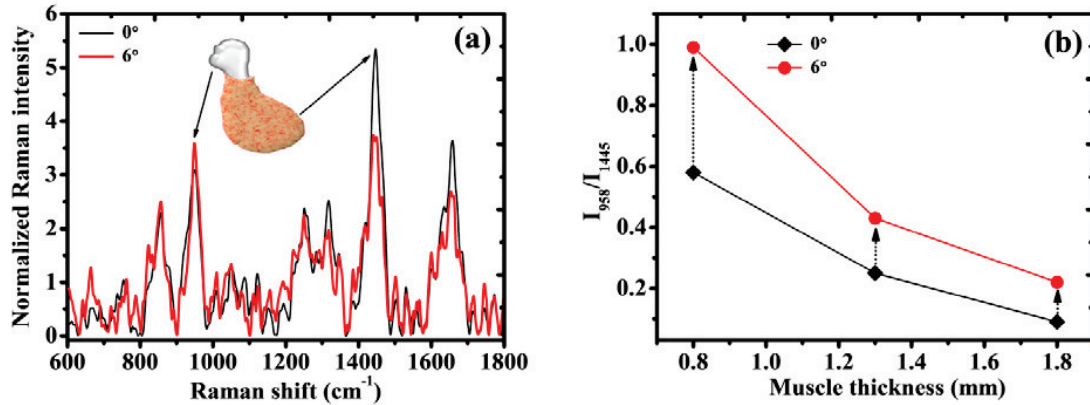
Figure 7.7: *(a) Inverse SORS spectra of the chicken tibia at two different angles, 0° and 6°. The spectra are normalized with respect to their means over the shown spectral range. The two arrows indicate the two Raman peaks of top and bottom layers of the tibia. (a) Plot of ratio, I_{958}/I_{1445} as a function of the muscle thickness at two different angles.*

Figure 7.7b plots the ratio, I_{958}/I_{1445} for three different thicknesses of the muscle (0.8, 1.3 and 1.8 mm respectively). One may infer that at non-zero angle the ratio is higher irrespective of its thickness i.e. for all the three thicknesses the inverse SORS effect can be achieved. While the increment in the ratio successively reduces with the thickness, nevertheless it is straightforward to understand from the fact that for a given offset (or angle) the tendency to probe bottom layer is inversely proportional to the thickness of the top layer.

The above results clearly demonstrate the viability of the proposed scheme for implementing an inverse SORS configuration. The present scheme executes SORS measurements of layered turbid media by using a multi-mode optical fiber and performs the same function that usually is done by an axicon lens [31]. However, the use of a fiber over the axicon lens has a few advantages. For example, with the fiber-based configuration it will be possible to make a compact and pencil-sized inverse SORS probe, an important

requirement for *in-vivo* tissue analysis in a clinical setting, which otherwise is not possible with the conventional configuration of inverse SORS based on axicon lens whose minimum available size, at present, is ~25 mm. Further, for introducing spatial offsets required for probing various sub-surface depths, one needs to form illumination rings of various sizes on the sample surface. It requires the system to have arrangement of movement of the axicon lens (ranging from several tens to hundreds of millimeters) which in turn renders the system bulkier as compared to that based on the present scheme where no such movement is required.

Although the proposed scheme offers several advantages over the axicon lens based configuration, perhaps its only demerit is that unlike in the case of an axicon lens based system, it is beyond the scope of the scheme to probe below a certain sub-surface depth. This is because while an axicon lens allows to form illumination ring of any large size (by varying the distance of the lens from the sample surface) without ever compromising on the width (which remains constant) of the ring, in the fiber based arrangement the size of the illumination ring becomes constant (though the width of the ring gets thinner) beyond a certain angle (for example ~6^0 in the present case) thereby putting a limit on the spatial offset (which gets fixed to a constant value) one can introduce. However, this limiting offset is sufficient for many a practical application requiring probing of sub-surface depths. For example, in the present setup, the limiting offset was found to be ~6 mm, sufficient to probe a depth of ~3 mm. It is important to mention here that the much higher spatial offsets may not always be practically useful as the SNR of the Raman signal significantly deteriorates with increasing spatial offsets between illumination and collection. For example, in an axicon lens based configuration, the offsets >8 mm have rarely been used [21-22].

7.5 Summary

To summarize, in this chapter, an alternate scheme for implementing inverse SORS has been described. The details of the experimental set-up developed based on this novel scheme and the results of the evaluation of its performance in probing sub-surface depths in layered turbid media are presented. The ring shaped illumination was generated with a multi-mode fiber (lying in the source arm of the experimental set-up) kept at non-zero angle with respect to the axis of the lens used for focusing the laser light onto its tip. By varying this angle, the Raman illumination beam was incident onto the sample surface in the form of concentric illumination rings of varying radii. The back-scattered Raman light exiting the sample surface at the centre of the concentric rings was then collected for detection. A notable advantage of the present scheme is that unlike the previously reported inverse SORS setups, it does not require any movement for generating various spatial offsets needed for probing sub-surface layers of a given sample. Another important advantage is its suitability in making a compact and pencil-sized inverse SORS probe, required for *in-vivo* tissue analysis. The ability of the developed system to measure Raman spectra of the subsurface layers was demonstrated using layered non-biological phantoms and biological tissues.

CHAPTER 8

Conclusions and future prospects

8.1 Conclusions

To conclude, in this thesis, we have presented our research on the development and evaluation of various depth-sensitive Raman spectroscopic techniques for the analysis of layered turbid media like biological tissues. Two primary objectives were set for the present work. The first objective was to investigate the applicability of existing depth-sensitive Raman spectroscopic techniques for applications involving turbid media such as biological tissues and evaluate their relative performances in probing sub-surface depths within the media. In order to achieve this objective, two independent studies were carried out. In the first study, applicability of a CRS based technique was assessed for obtaining diagnostic feedback about a tissue under interrogation by measuring confocal Raman spectra from intact FFPE tissue blocks without preparing any micro-thin tissue sections or any other processing [122]. A CRS system using a 785 nm diode laser was developed and characterized by estimating various parameters such as SNR, spatial resolution, spectral resolution etc. and then used for measuring the confocal Raman spectra from the intact FFPE tissue blocks. Combined use of the CRS system and a multivariate statistical diagnostic algorithm showed that this could be a promising tool in a clinical pathology setting for non-destructively determining the pathologic state of a tissue embedded in intact FFPE blocks.

In the second study, the applicability of inverse SORS was investigated in identifying the presence of a very low Raman-active turbid sample placed inside a highly Raman-active

diffusely scattering matrix [123]. An inverse SORS set up was developed and used to measure Raman spectra from paraffin sandwiched chicken tissue blocks. The effect of the thickness of the sub-surface (tissue) and the surface (paraffin) layers as well as the turbidity of the surface layer on the ability of the inverse SORS technique to efficiently recover the weak tissue Raman signatures was systematically investigated. It was found that both the probing depth and the quality of the recovery of the tissue Raman signatures varied inversely with turbidity of the surface layer. However, on increasing the thickness of the tissue, the recovery became easier.

The second objective of the thesis was to develop new depth-sensitive Raman spectroscopic techniques and evaluate their capabilities in overcoming major limitations of the existing techniques keeping in mind the future objective of translating them into field-deployable instruments. The work towards achieving this objective resulted in the development of four novel approaches of depth-sensitive Raman measurements from tissues listed below.

1. RCPRS: In this approach, the depth-sensitive Raman measurements were performed by moving the focal plane of the illumination beam away from the tissue surface unlike in CRS where it was moved across the different depths of the target tissue. The approach was shown to overcome the drawback of lens-sample contact faced in a CRS setup and found to probe comparatively larger sub-surface depths.

2. OCRS: It uses the experimental configuration of a confocal Raman, but employs off-confocal Raman detection for sub-surface interrogation of layered tissues [124]. The two important advantages of this approach are that it does not require any adjustment in the sample arm of the system and the illumination light remains fixed on the sample surface and thereby providing the effective illumination.

3. CSRS: It employs the configuration of cone-shell Raman excitation and cone detection [125]. Using this approach, Raman signal from a depth of up to few mm (~2.5 mm) beneath the surface could be measured.

4. An axicon lens free approach for implementing an inverse SORS: This approach not only probes higher depths as compared to CSRS but also has the ability of developing a compact and pencil-sized SORS probe, an urgent and current need in routine clinical pathology setting [126].

A careful review of the above techniques reveals that choice of an appropriate depth-sensitive Raman technique for a given application is decided by various criteria, the nature of the sample and the depths to be probed being the most important. For example, while probing a depth up to ~200 μm in a transparent or semi-transparent sample, the preference should be given to CRS. If the sample is of reactive nature and/or highly turbid, the CRS can be replaced by RCRS or RCPRS scheme of Raman detection. Till a depth of ~500 μm, RCRS (or RCPRS in some cases) could be a choice for depth-sensitive Raman measurements. In case of biological tissues or the samples of low Raman cross-sections, OCRS is the optimum choice with the ability of picking up Raman signatures from a depth up to ~600-800 μm. For identical depths, OCRS provides a more effective illumination of the sample as compared to the RCRS based approach. For probing still deeper (depths ~1-2.5 mm), CSRS may be used. However, for probing a depth in the range of ~1-5 mm, inverse SORS is the best candidate. It should be noted here that the above mentioned depth ranges for different schemes are the optimal thicknesses of the surface layers of the phantoms as well as biological samples for which we could obtain detectable Raman signal from sub-surface layers. However, for different samples, the depth ranges may vary because of the difference in their optical properties (e.g. absorption, scattering, anisotropy factor etc.).

8.2 Future prospects

After having demonstrated the promising potential of various novel depth-sensitive Raman spectroscopic techniques through proof of the concept studies, the next important task will be to convert these techniques into portable instruments suitable for field use. Depending on the complexities of the experimental configurations for the different depth-sensitive techniques proposed, the challenges are expected to be different. The efforts will be therefore made in order to overcome these challenges.

One of the future studies includes development of a portable SORS module. Such module will be very useful in analyzing layered turbid samples. An inverse SORS configuration using an axicon lens may be used for developing the module capable in providing the depth-sensitive Raman signals (of appreciable SNR) from biological tissues. Although such module to be developed can be used for *ex-vivo* tissue applications like cancer diagnosis through FFPE tissue blocks, for *in-vivo* applications a pencil-sized SORS probe may be wished. The other future study will thus involve development of a pencil-sized SORS probe and for achieving this goal, the axicon lens free SORS configuration presented in the Chapter 7 of the thesis may be used. The capability of such SORS probe for *in-vivo* depth-sensitive Raman measurements by probing epithelial and stromal layers in tissues of human oral cavity will also be investigated.

One major finding of the work described in the thesis was the OCRS concept. A hand-held OCRS probe will be developed in near future. Such probe will not require any adjustment in its sample arm unlike the available probes based on CRS like configuration. Further, the illumination light remains fixed onto the surface of the sample under investigation. Such unique advantages to be offered by an OCRS probe are very much

desired for depth-sensitive measurements *in-situ* from layered turbid samples particularly those having irregular surfaces like biological tissues.

Recently, there is a growing interest in combining Raman spectroscopy with OCT in a single optical system in order to improve the performance of optical method for tissue analysis. Since Raman reveals biochemical information at the molecular level and OCT is able to provide morphological features of a tissue, combination of the two allows complete analysis of the tissue state. The dual-modal Raman-OCT systems reported in literature suffer from one major drawback in that while OCT provides information from the various sub-surface depths of a tissue, the backscattered Raman signal, co-registered with an OCT image at a particular point, contains information which is volume integrated. This issue was addressed to by our group in the recent past [20], by devising a novel scheme based on depth-sensitive Raman spectroscopy combined with OCT. In this scheme, a depth-sensitive Raman system incorporating a confocal like configuration was combined by co-aligning the Raman beam with the OCT beam in the sample arm of a time-domain OCT (TD-OCT) system. Despite the success of the combined system in obtaining the OCT image and the Raman signal from the same depth of a layered sample, the system suffers from two practical problems which limit its field use. First, for measuring depth-sensitive Raman signal, one needs to move the sample arm of the system which is not desirable in field applications, and second, the time-domain OCT system, used as the platform for developing the dual-modal system, has bulky optics preventing development of a compact system, and slow image acquisition rate, not acceptable in applications requiring rapid image acquisition. The future objective will thus be to develop an integrated Raman–OCT system that can overcome these limitations. For developing the dual-modal system, OCRS will be combined with swept source OCT (SS-OCT) in a single optical platform. While OCRS allows sub-surface interrogation of layered turbid samples at depths beyond the reach of a typical confocal

Raman without requiring any adjustment in the sample arm, SS-OCT provides faster image acquisition rate and deeper penetration. The performance of the dual-modal system so developed will be evaluated using various non-biological and biological layered turbid samples. In addition, like confocal imaging, the efforts may also be made for off-confocal Raman imaging in order to have a 3D biochemical map of the tissue under investigation.

Last but not least, depth-sensitive configurations of other spectroscopic techniques like fluorescence and diffuse reflectance will also be developed. The availability of miniaturized spectrometers will help in developing compact and portable depth-sensitive optical spectroscopic tools for *in-vivo* tissue applications.

References

[1] E. Cordero, I. Latka, C. Matthaus, I. W. Schie and J. Popp, *J. Biomed. Opt.* 23(7), 071210 (2018).

[2] D. W. Shipp, F. Sinjab and I. Notingher, *Adv. Opt. Photonics* 9(2), 315 (2017).

[3] I. Pence and A. M. Jansen, *Chem. Soc. Rev.* 45(7), 1958 (2016).

[4] K. Kong, C. Kendall, N. Stone and I. Notingher, *Adv. Drug Deliv. Rev.* 89, 121 (2015).

[5] I. J. Bigio and S. G. Bown, *Cancer Biol. Ther.* 3(3), 259 (2004).

[6] E. B. Hanlon, R. Manoharan, T. W. Koo, K. E. Shafer, J. T. Motz, M. Fitzmaurice, J. R. Kramer, I. Itzkan, R. R. Dasari and M. S. Feld, *Phys. Med. Biol.* 45(2), R1 (2000).

[7] R. Manoharan, Y. Wang and M. S. Feld, *Spectrochim. Acta A* 52(2), 215 (1996).

[8] L. P. C. Smith, H. G. M. Edwards, H. P. Endtz, J. M. Kros, F. Heule, H. Barr, J. S. Robinson Jr., H. A. Bruining and G. J. Puppels, *Biopolymers (Biospectrosc.)* 67(1), 1 (2002).

[9] C. J. Frank, R. L. McCreery and D. C. B. Redd, *Anal. Chem.* 67(5), 777 (1995).

[10] A. M. Jansen and R. R. Kortum, *J. Biomed. Opt.* 1(1), 31 (1996).

[11] J. T. Motz, M. Hunter, L. H. Galindo, J. A. Gardecki, J. R. Kramer, R. R. Dasari and M. S. Feld, *Appl. Opt.* 43(3), 542 (2004).

[12] U. Utzinger and R. R. Richards-Kortum, *J. Biomed. Opt.* 8(1), 121 (2003).

[13] I. R. Lewis and P. R. Griffiths, *Appl. Spectrosc.* 50(10), 12A (1996).

[14] C. Zhu, Q. Liu and N. Ramanujam, *J. Biomed. Opt.* 8(2), 237 (2003).

[15] R. A. Schwarz, D. Arifler, S. K. Chang, I. Pavlova, I. A. Hussain, V. Mack, B. Knight, R. R. Kortum and A. M. Gillenwater, *Opt. Lett.* 30(10), 1159 (2005).

[16] R. A. Schwarz, W. Gao, D. Daye, M. D. Williams, R. R. Kortum, A. M. Gillenwater, *Appl. Opt.* 47(6), 825 (2008).

[17] P. Matousek, I. P. Clark, E. R. C. Draper, M. D. Morris, A. E. Goodship, N. Everall, M. Towrie, W. F. Finney and A. W. Parker, *Appl. Spectrosc.* 59(4), 393 (2005).

[18] M. D. Keller, E. Vargis, N. de M. Granja, R. H. Wilson, M. A. Mycek, M. C. Kelley and A. M. Jansen, *J. Biomed. Opt.* 16(7), 077006 (2011).

[19] P. Matousek, E. R. C. Draper, A. E. Goodship, I. P. Clark, K. L. Ronayne and A. W. Parker, *Appl. Spectrosc.* 60(7), 758 (2006).

[20] K. M. Khan, H. Krishna, S. K. Majumder, K. D. Rao and P. K. Gupta, *J. Biophotonics* 7(1-2), 77 (2014).

[21] P. Matousek and N. Stone, *J. Biophotonics* 6(1), 7 (2013).

[22] P. Matousek, *Chem. Soc. Rev.* 36(8), 1292 (2007).

[23] B. B. Das and R. R. Alfano, *Curr. Sci.* 77(7), 885 (1999).

[24] C. Dunsby and P. M. W. French, *J. Phys. D: Appl. Phys.* 36(14), R207 (2003).

[25] N. J. Everall, *Appl. Spectrosc.* 63(9), 245A (2009).

[26] N. J. Everall, *Analyst* 135(10), 2512 (2010).

[27] P. Matousek, N. Everall, M. Towrie and A. W. Parker, *Appl. Spectrosc.* 59(2), 200 (2005).

[28] Z. J. Smith and A. J. Berger, *Opt. Lett.* 30(11), 1363 (2005).

[29] R. Tabaksblat, R. J. Meier and B. J. Kip, *Appl. Spectrosc.* 46(1), 60 (1992).

[30] C. J. D. Grauw, N. M. Sijtsema, C. Otto and J. Greve, *J. Microsc.* 188(3), 273 (1997).

[31] P. Matousek, *Appl. Spectrosc.* 60(11), 1341 (2006).

[32] N. J. Everall, *Appl. Spectrosc.* 54(6), 773 (2000).

[33] J. P. Tomba and J. M. Pastor, *Appl. Spectrosc.* 62(7), 817 (2008).

[34] G. J. Puppels, F. F. M. De-Mul, C. Otto, J. Greve, M. R. Nicoud, D. J. A. Jovin and T. M. Jovin, *Nature* 347(6290), 301 (1990).

[35] G. J. Puppels, H. S. P. Garritsen, G. M. J. S. Nolten, F. F. M. De-Mul and J. Greve, *Biophys. J.* 60(5), 1046 (1991).

[36] P. J. Caspers, G. W. Lucassen, R. Wolthuis, H. A. Bruining and G. J. Puppels, *Biospectrosc.* 4(5), S31 (1998).

[37] P. J. Caspers, G. W. Lucassen, E. A. Carter, H. A. Bruining and G. J. Puppels, *J. Invest. Dermatol.* 116(3), 434 (2001).

[38] J. Choi, J. Choo, H. Chung, D. G. Gweon, J. Park, H. J. Kim, S. Park and C. H. Oh, *Biopolymers* 77(5), 264 (2005).

[39] C. A. Lieber, S. K. Majumder, D. Billheimer, D. L. Ellis and A. M. Jansen, *J. Biomed. Opt.* 13(2), 024013 (2008).

[40] C. A. Lieber, S. K. Majumder, D. L. Ellis, D. D. Billheimer and A. M. Jansen, *Lasers Surg. Med.* 40(7), 461 (2008).

[41] J. D. Bancroft and M. Gamble, Theory and Practice of Histological Techniques, Churchill Livingstone, 2002, 5th edn.

[42] J. A. Kiernan, Histological and Histochemical Methods: Theory and Practice, Scion, 2008, 4th edn.

[43] E. O. Faolain, M. B. Hunter, J. M. Byrne, P. Kelehan, H. A. Lambkin, H. J. Byrne and F. M. Lyng, *J. Histochem. Cytochem.* 53(1), 121 (2005).

[44] N. Rashid, H. Nawaz, K. W. C. Poon, F. Bonnier, S. Bakhiet, C. Martin, J. J. O'Leary, H. J. Byrne and F. M. Lyng, *Exp. Mol. Pathol.* 97(3), 554 (2014).

[45] F. M. Lyng, D. Traynor, I. R. M. Ramos, F. Bonnier and H. J. Byrne, *Anal. Bioanal. Chem.* 407(27), 8279 (2015).

[46] C. M. Krishna, G. D. Sockalingum, L. Venteo, R. A. Bhat, P. Kushtagi, M. Pluot and M. Manfait, *Biopolymers* 79(5), 269 (2005).

[47] V. Vrabie, C. Gobinet, O. Piot, A. Tfayli, P. Bernard, R. Huez and M. Manfait, *Biomed. Signal Process. Control* 2(1), 40 (2007).

[48] P. J. Caspers, G. W. Lucassen and G. J. Puppels, *Biophys. J.* 85(1), 572 (2003).

[49] K. M. Khan, R. Kumar, H. Krishna, K. D. Rao and S. K. Majumder, *Biomed. Spectrosc. Imaging* 5(3), 313 (2016).

[50] S. X. Li, Q. Y. Chen, Y. J. Zhang, Z. M. Liu, H. L. Xiong, Z. Y. Guo, H. Q. Mai and S. H. Liu, *J. Biomed. Opt.* 17(12), 125003 (2012).

[51] C. A. Lieber and A. M. Jansen, *Opt. Express* 15(19), 11874 (2007).

[52] M. Agenant, M. Grimbergen, R. Draga, E. Marple, R. Bosch and C. V. Swol, *Biomed. Opt. Express* 5(4), 1203 (2014).

[53] C. Eliasson, M. Claybourn and P. Matousek, *Appl. Spectrosc.* 61(10), 1123 (2007).

[54] P. Matousek, C. Conti, M. Realini and C. Colombo, *Analyst* 141(3), 731 (2016).

[55] C. Conti, C. Colombo, M. Realini, G. Zerbi and P. Matousek, *Appl. Spectrosc.* 68(6), 686 (2014).

[56] C. Conti, M. Realini, C. Colombo and P. Matousek, *Analyst* 140(24), 8127 (2015).

[57] M. V. Schulmerich, W. F. Finney, V. Popescu, M. D. Morris, T. M. Vanasse and S. A. Goldstein, *Proc. SPIE* 6093, 60930O (2006).

[58] M. V. Schulmerich, J. H. Cole, J. M. Kreider, F. E. White, K. A. Dooley, S. A. Goldstein and M. D. Morris, *Appl. Spectrosc.* 63(3), 286 (2009).

[59] M. D. Keller, S. K. Majumder and A. M. Jansen, *Opt. Lett.* 34(7), 926 (2009).

[60] M. D. Keller, R. H. Wilson, M. A. Mycek and A. M. Jansen, *Appl. Spectrosc.* 64(6), 607 (2010).

[61] B. R. McCreadie, M. D. Morris, T. Chen, D. S. Rao, W. F. Finney, E. Widjaja and S. A. Goldstein, *Bone* 39(6), 1190 (2006).

[62] J. M. Yuen, N. C. Shah, J. T. Walsh, M. R. Glucksberg and R. P. Van Duyne, *Anal. Chem.* 82(20), 8382 (2010).

[63] K. Ma, J. M. Yuen, N. C. Shah, J. T. Walsh, M. R. Glucksberg and R. P. Van Duyne, *Anal. Chem.* 83(23), 9146 (2011).

[64] N. Stone, M. Kerssens, G. R. Lloyd, K. Faulds, D. Graham and P. Matousek, *Chem. Sci.* 2(4), 776 (2011).

[65] M. V. Schulmerich, K. A. Dooley, M. D. Morris, T. M. Vanasse and S. A. Goldstein, *J. Biomed. Opt.* 11(6), 060502 (2006).

[66] A. M. J. Wang, J. E. Bender, J. Pfefer, U. Utzinger and R. A. Drezek, *J. Biomed. Opt.* 10(4), 044017 (2005).

[67] Q. Liu and N. Ramanujam, *Appl. Opt.* 45(19), 4776 (2006).

[68] T. F. Cooney, H. T. Skinner and S. M. Angel, *Appl. Spectrosc.* 50(7), 836 (1996).

[69] N. Ghosh, S. K. Majumder, H. S. Patel and P. K. Gupta, *Opt. Lett.* 30(2), 162 (2005).

[70] D. A. Woods and C. D. Bain, *Analyst* 137(1), 35 (2012).

[71] C. Zhu and Q. Liu, *Opt. Express* 20(28), 29807 (2012).

[72] Y. H. Ong and Q. Liu, *Opt. Lett.* 38(15), 2647 (2013).

[73] C. Gobinet, V. Vrabie, M. Manfait and O. Piot, *IEEE Trans. Biomed. Eng.* 56(5), 1371 (2009).

[74] A. Tfayli, C. Gobinet, V. Vrabie, R. Huez, M. Manfait and O. Piot, *Appl. Spectrosc.* 63(5), 564 (2009).

[75] K. M. Tan, C. S. Herrington and C. T. A. Brown, *J. Biophotonics* 4(1-2), 40 (2011).

[76] M. Fryling, C. J. Frank and R. L. McCreeey, *Appl. Spectrosc.* 47(12), 1965 (1993).

[77] H. Krishna, S. K. Majumder and P. K. Gupta, *J. Raman Spectrosc.* 43(12), 1884 (2012).

[78] I. T. Jolliffe, Principal Component Analysis, Springer, 2002, 2nd edn.

[79] B. Krishnapuram, L. Carin, M. A. T. Figueiredo and A. J. Hartemink, *IEEE Trans. Pattern Anal. Machine Intell.* 27(6), 957 (2005).

[80] S. K. Majumder, S. C. Gebhart, M. D. Johnson, R. Thompson, W. C. Lin and A. M. Jansen, *Appl. Spectrosc.* 61(5), 548 (2007).

[81] K. E. S. Peltier, A. S. Haka, M. Fitzmaurice, J. Crowe, J. Myles, R. R. Dasari and M. S. Feld, *J. Raman Spectrosc.* 33(7), 552 (2002).

[82] S. K. Majumder, M. D. Keller, F. I. Boulos, M. C. Kelley and A. M. Jansen, *J. Biomed. Opt.* 13(5), 054009 (2008).

[83] F. Bonnier, F. Petitjean, M. J. Baker and H. J. Byrne, *J. Biophotonics* 7(3-4), 167 (2014).

[84] A. Ishimaru, Wave Propagation and Scattering in Random Media; vol 1, New York: Academic Press, 1978.

[85] W. F. Cheong, S. A. Prahl and A. J. Welch, *IEEE J. Quantum Electron.* 26(12), 2166 (1990).

[86] V. V. Tuchin, *Phys. Usp.* 40(5), 495 (1997).

[87] P. K. Gupta, *Curr. Sci.* 76(10), 1341 (1999).

[88] T. E. Matthews, M. Medina, J. R. Maher, H. Levinson, W. J. Brown and A. Wax, *Optica* 1(2), 105 (2014).

[89] B. B. Das, K. M. Yoo and R. R. Alfano, *Opt. Lett.* 18(13), 1092 (1993).

[90] A. Kienle, L. Lilge, M. S. Patterson, R. Hibst, R. Steiner and B. C. Wilson, *Appl. Opt.* 35(13), 2304 (1996).

[91] L. Wang, S. L. Jacques and L. Zheng, *Compt. Methods Programs Biomed.* 47(2), 131 (1995).

[92] T. J. Pfefer, A. Agrawal and R. A. Drezek, *J. Biomed. Opt.* 10(4), 044016 (2005).

[93] T. Durduran, R. Choe, W. B. Baker and A. G. Yodh, *Rep. Prog. Phys.* 73, 076701 (2010).

[94] O. K. Dudko and G. H. Weiss, *Diffus. Fund.* 2, 1 (2005).

[95] S. L. Jacques, *Phys. Med. Biol.* 58(11), R37 (2013).

[96] N. J. Everall, *Spectrosc.* 19(11), 16 (2004).

[97] N. J. Everall, *Appl. Spectrosc.* 62(6), 591 (2008).

[98] A. M. Macdonald, A. S. Vaughan and P. Wyeth, *J. Raman Spectrosc.* 36(3), 185 (2005).

[99] A. M. Macdonald and A. S. Vaughan, *J. Raman Spectrosc.* 38(5), 584 (2007).

[100] K. D. Rao, A. Alex, Y. Verma, S. Thampi and P. K. Gupta, *J. Biophotonics* 2(5), 288 (2009).

[101] T. Vo-Dinh, Biomedical Photonics Handbook, CRC Press LLC chap 2-4 (2003).

[102] C. Conti, M. Realini, C. Colombo, A. Botteon and P. Matousek, *J. Raman Spectrosc.* 47(5), 565 (2016).

[103] M. Duocastella and C. B. Arnold, *Laser Photonics Rev.* 6(5), 607 (2012).

[104] C. A. Patil, N. Bosschaart, M. D. Keller, T. G. van Leeuwen and A. M. Jansen, *Opt. Lett.* 33(10), 1135 (2008).

[105] J. M. Schmitt, A. Knuttel and M. Yadlowsky, *J. Opt. Soc. Am. A* 11(8), 2226 (1994).

[106] C. Yang, K. An, L. T. Perelman, R. R. Dasari and M. S. Feld, *J. Opt. Soc. Am. A* 16(4), 866 (1999).

[107] I. Iglesias, *Opt. Laser Technol.* 95, 8 (2017).

[108] P. Matousek and A. W. Parker, *Appl. Spectrosc.* 60(12), 1353 (2006).

[109] C. Eliasson and P. Matousek, *Anal. Chem.* 79(4), 1696 (2007).

[110] C. Ricci, C. Eliasson, N. A. Macleod, P. N. Newton, P. Matousek and S. G. Kazarian, *Anal. Bioanal. Chem.* 389(5), 1525 (2007).

[111] A. Aina, M. D. Hargreaves, P. Matousek and J. C. Burley, *Analyst* 135(9), 2328 (2010).

[112] M. Fransson, J. Johansson, A. Sparen and O. Svensson, *J. Chemom.* 24(11-12), 674 (2010).

[113] C. Eliasson, N. A. Macleod, L. Jayes, F. C. Clarke, S. Hammond, M. R. Smith and P. Matousek, *J. Pharm. Biomed. Anal.* 47(2), 221 (2008).

[114] C. Eliasson, N. A. Macleod and P. Matousek, *Vib. Spectrosc.* 48(1), 8 (2008).

[115] C. Eliasson, N. A. Macleod and P. Matousek, *Anal. Chem.* 79(21), 8185 (2007).

[116] A. Ghatak and K. Thyagrajan, in: Fundamentals of photonics, edited by C. Roychoudhuri, Bellingham, Washington, SPIE, Module 1.7 (2008).

[117] R. K. Shevgaonkar, in: NPTEL online courses, Propagation of light in an optical fiber, Lecture: 3.

[118] S. Nieswand, Measurement of the exit characteristics of light from optical multimode plastic fibres, MSc thesis, III. Physikalisches Institut A, RWTH Aachen University (2014).

[119] H. Ma, H. Cheng, W. Zhang, L. Liu and Y. Wang, *Chin. Opt. Lett.* 5(8), 460 (2007).

[120] Y. Yan, G. Wang, W. Sun, A-Li Luo, Z. Ma, J. Li and S. Wang, *MNRAS* 466, 1669 (2017).

[121] S. Ramachandran, J. M. Fini, M. Mermelstein, J. W. Nicholson, S. Ghalmi and M. F. Yan, *Laser & Photon. Rev.* 2(6), 429 (2008).

[122] K. M. Khan, H. Krishna, C. V. Kulkarni and S. K. Majumder, *J. Anal. Oncol.* 5(4), 153 (2016).

[123] K. M. Khan, S. B. Dutta, H. Krishna and S. K. Majumder, *J. Biophotonics* 9(9), 879 (2016).

[124] K. M. Khan, N. Ghosh and S. K. Majumder, *J. Opt.* 18(9), 095301 (2016).

[125] K. M. Khan, S. K. Majumder and P. K. Gupta, *J. Biophotonics* 8(11-12), 889 (2015).

[126] K. M. Khan, S. B. Dutta, N. Kumar, A. Dalal, A. Srivastava, H. Krishna and S. K. Majumder, *J. Biophotonics* (2019); e201900140 https://doi.org/10.1002/jbio.201900140